
Electronic Thesis and Dissertation Repository

8-15-2019 10:30 AM

Pneumatic Hyperelastic Robotic End-Effector for Grasping Soft Curved Organic Objects

Alexandre Galley
The University of Western Ontario

Supervisor
Knopf, George K.
The University of Western Ontario

Graduate Program in Mechanical and Materials Engineering
A thesis submitted in partial fulfillment of the requirements for the degree in Master of Engineering Science
© Alexandre Galley 2019

Follow this and additional works at: <https://ir.lib.uwo.ca/etd>



Part of the [Other Mechanical Engineering Commons](#)

Recommended Citation

Galley, Alexandre, "Pneumatic Hyperelastic Robotic End-Effector for Grasping Soft Curved Organic Objects" (2019). *Electronic Thesis and Dissertation Repository*. 6392.
<https://ir.lib.uwo.ca/etd/6392>

This Dissertation/Thesis is brought to you for free and open access by Scholarship@Western. It has been accepted for inclusion in Electronic Thesis and Dissertation Repository by an authorized administrator of Scholarship@Western. For more information, please contact wlsadmin@uwo.ca.

Abstract

Pneumatically-driven soft robotic grippers can elastically deform to grasp delicate, curved organic objects with minimal surface damage. However, common actuators have multipart geometries and are fabricated with ultra-soft hyperelastic elastomers not originally intended for scientific applications. The complexity of the actuator geometry and extreme nonlinearity of their material's stress-strain behaviour make it difficult to predict the actuator's deformation prior to experimentation. In this work, a compact soft pneumatic gripper made with polydimethylsiloxane (PDMS) is developed for grasping delicate organic objects, analyzed through computational modelling and experimentally validated. COMSOL Multiphysics is used to simulate the impact of geometrical parameters on the actuator's behaviour, allowing for the refinement of the proposed geometry prior to fabrication. Optimal parameters are selected for fabrication, with experimental tests matching simulations within ± 1.11 mm. Gripper performance is evaluated for three actuator wall thicknesses in terms of contact area with target, contact force, and maximum payload before slippage. The comparative assessment between simulations and experiments demonstrate that the proposed soft actuators can be used in robotic grippers tailored for grasping delicate objects without damaging their surface. Furthermore, analysis of the actuators provides additional insight on how to design simple but effective soft systems.

Keywords

Soft robotic grippers; hyperelastic materials; polydimethylsiloxane; COMSOL Multiphysics simulation

Summary for Lay Audience

Air-powered soft robotic grippers are made of rubber-like materials that can stretch and inflate to collect delicate objects like fruits and vegetables. However, the soft “finger” components of the robotic gripper commonly have multipart geometries, and the rubber materials used in their fabrication were not meant for scientific applications. The combination of these complex geometries and the extreme unpredictability of non-standard soft materials make it difficult to calculate the “finger’s” movement before performing experiments. In this work, a compact and soft air-powered gripper is developed and fabricated using a silicone material commonly used in the scientific community, polydimethylsiloxane (PDMS). The gripper is designed for grasping delicate produce. The inflation and behaviour of the soft gripper components are first analyzed using computer simulations based on geometrical dimensions and air pressure. Data acquired from these simulations is used to improve the proposed soft component geometry before building it, reducing the number of trial-and-error tests needed to previously develop soft robotic “fingers”. After fabricating soft “finger” components, experiments are performed to compare the simulated data with experimental results. This comparison shows a match between simulations and experiments within ± 1.11 mm. The “fingers” are then assembled into three different grippers and tested to assess each gripper’s effectiveness at grasping objects of different shapes and weights. The comparison between computer simulations and real experiments demonstrate that the proposed soft “fingers” can be used in grippers designed for picking up delicate objects without damaging them. Furthermore, analysis of the soft components provides additional insight on how to design simple but effective soft robots.

Acknowledgments

This research is the result of collaboration between the University of Western Ontario (London, Ontario) and Vineland Research and Innovation Centre, Lincoln, Ontario, Canada. This research was funded, in part, by a Mitacs Accelerate Internship grant and Natural Sciences and Engineering Research Council of Canada (NSERC) Discovery Grant (Number: RGPIN/05858-2014.). Specifically, I would like to thank Drs. Gideon Avigad and Mohamed Kashkoush from Vineland Research for their support and guidance during the early stages of this research project.

Special thanks to my supervisor Prof. George K. Knopf for his continual support, advice, and encouragement. I appreciate the opportunity he gave me to work in such a complex and interesting field. I would also like to thank Dr. Dogan Sinar, who gave me advice on how to approach my work and how to get started with PDMS. The dedication you both show to your work is inspiring.

My appreciation also goes out to Prof. Aaron Price and the members of the Organic Mechatronics and Smart Materials Laboratory, especially Andrew Cullen, Ben Holness, and Rami Abu-Shammeh, for their insight, support, and friendship throughout my studies. Allowing me the use of their lab space proved critical to my work. I would also like to extend my thanks and gratitude to laboratory supervisor Mr. Dave Lunn, both for his friendship and for helping me throughout my studies and TA duties. Thank you to my colleague Mr. Ahmed Tanashi for his help and use of his TrakSTAR sensor system. I can very honestly say that I could not have done it without them.

Finally, I would like to thank my dearest friends and family. I owe everything to my parents for their patience in imparting their persistent work ethic and for their unrelenting support. I owe special gratitude to my grandfather, who passed away in August 2018. He helped my parents shape the man I am today, and I strive to be someone he would be proud of.

Table of Contents

Abstract.....	ii
Summary for Lay Audience	iii
Acknowledgments	iv
List of Figures.....	viii
List of Tables	xiv
List of Appendices.....	xv
List of Abbreviations, Terminology and Nomenclature.....	xvi
1 Introduction.....	1
1.1 Research Motivation	2
1.2 Objectives of Research	3
1.3 Major Contributions.....	4
1.4 Thesis Organization	5
2 Background and Literature Review	6
2.1 Hyperelastic Theory	6
2.1.1 Governing Equations	7
2.2 Polydimethylsiloxane (PDMS).....	11
2.2.1 Ultra-soft, Unpredictable Elastomers.....	11
2.2.2 Properties of PDMS	12
2.2.3 Importance of Degassing PDMS	14
2.2.4 Removing PDMS from a Mould.....	15
2.2.5 Partial Moulding Techniques.....	16
2.3 Soft Robotics Technology.....	16
2.3.1 Review of Soft Pneumatic Actuators	17
2.3.2 Review of Soft Pneumatic Grippers	27

	2.4 Chapter Summary	32
3	Design Methodology and Fabrication	33
	3.1 Geometric Design of Elastomeric Actuators	33
	3.2 Actuator Fabrication	35
	3.3 Role and Functionality of COMSOL Multiphysics Software.....	40
	3.3.1 Defining PDMS Material Properties for Finite Element Modelling	40
	3.3.2 Model Implementation in COMSOL Multiphysics 5.3	42
	3.3.3 Mesh Generation for Finite Element Modelling	43
	3.4 Chapter Summary	44
4	COMSOL Simulations and Results.....	45
	4.1 Wall Displacement for a Parameter Change	45
	4.2 Surface Loads	49
	4.3 Relating to the Strain-Energy Function	50
	4.4 Principal Strain and Principal Stretch	54
	4.5 Chapter Summary	58
5	Experimental Setup and Testing	59
	5.1 Actuator Displacement Under Applied Pressure	59
	5.1.1 Experimental Setup.....	60
	5.1.2 Measured Actuator Displacement.....	61
	5.1.3 Wall Displacement over Pressure	62
	5.2 Gripper Contact Forces and Maximum Payload Capabilities.....	63
	5.2.1 Experimental Setup.....	63
	5.2.2 Contact Force and Maximum Payload Results	65
	5.3 Chapter Summary	66
6	Application Study and Discussion	67
	6.1 Robotic Harvesting Systems in Horticulture	67
	6.1.1 Review of Existing Mushroom-Harvesting End-Effectors	69

6.1.2 Standard Vacuum Cups Provided by Vineland	71
6.2 Parameters for Evaluation.....	71
6.3 Application Testing.....	72
6.4 Discussion of Results.....	75
6.5 Design for Different Applications	79
6.6 Chapter Summary	80
7 Concluding Remarks	81
7.1 Summary of Thesis	81
7.2 Summary of Conclusions.....	83
7.3 Recommendations for Future Research.....	84
Bibliography	86
A PneuNet Actuators	92
B Vacuum Cups	96
C Supporting Information on Mushrooms.....	99
C.1 The White Mushroom, <i>Agaricus Bisporus</i>	99
C.2 Graze Harvesting Strategy	101
C.3 Overview of Existing Infrastructure at Vineland Research and Innovation Centre Inc. .	101
C.4 Mushroom Sample Measurements	103
D Actuator Moulding System CAD & Drawings	107
E Copyright Permissions	114
Curriculum Vitae	122

List of Figures

Figure 2.1 Stress-strain curve during a loading cycle. (a) Elastomer hyperelastic material behaviour; (b) Linear elastic material behaviour. Note that the Young's moduli are not to scale. As described by [24], [26], [27].	7
Figure 2.2 Volume element subjected to (a) uniaxial stress (σ) and (b) principal stresses.	7
Figure 2.3 Empirical formula of PDMS. As shown on Sigma-Aldrich [39].	12
Figure 2.4 Pneumatic Network soft bending actuators. (a) Deflated state; (b) Inflated State; (c) Ultra-soft material instability; (d) Limitations as a gripper design for the research application. Note that the actuators shown in this figure were fabricated as part of preliminary work for this research thesis.	18
Figure 2.5 Fiber-Reinforced actuators at different sleeve spacing configurations (Galloway et al. [63] © 2013 IEEE, included with permission).	21
Figure 2.6 FR actuator fabrication (Galloway). (a) Mould components; (b) Multi-step fabrication process (Galloway et al. [63] © 2013 IEEE, included with permission).	23
Figure 2.7 FR actuator fabrication (Miron) (Miron et al. [33] © 2018 CC-BY, included with permission).	24
Figure 2.8 Pneumatic artificial muscles. (a) PAM contraction for increasing pressure with constant mass; (b) Enhanced view of PAM braided sleeve. Figures created at Western University.	25
Figure 2.9 McKibben EBPAM. (a) Modified extensor McKibben actuator; (b) Extensor McKibben actuator further modified to bend (Al-Fahaam et al. [66], © 2018 Elsevier, included with permission).	26
Figure 2.10 Early Whitesides PneuNet grippers. Grasping an egg (top) and a sedated mouse (bottom) (Whitesides et al. [6], © 2011 WILEY, included with permission).	28
Figure 2.11 PneuNet Gripper for delicate ocean reef sampling (Galloway et al. [70], © 2016 Mary Ann Liebert, Inc., included with permission).	29
Figure 2.12 Universal PneuNet gripper testing tunable actuator lengths (Hao et al. [58], © 2016 IEEE, included with permission).	30

Figure 2.13 Maximum payload test of Fiber Reinforced grippers with different actuator sleeve spacing configurations (Galloway et al. [63], © 2013 IEEE, included with permission).....	31
Figure 2.14 Small (left) and large (right) variants of the Fiber Reinforced gripper developed at Sherbrooke University (Miron et al. [33], © 2018 CC-BY, included with permission).....	31
Figure 3.1 (a) Bottom view of a gripper comprised of three soft pneumatic actuators. (b) Outside geometry of the actuator's pneumatic chamber. (c) Internal structure of the chamber walls, location of the strain-limiting fiber mesh (blue) and the impact of inflation δ_d on the active deformable wall (red). Note that the deformation is for visualization purposes only.....	34
Figure 3.2 Top view of the (a) base for Mould 1; (b) base for Mould 2; and (c) detachable outer walls.	36
Figure 3.3 Key steps in the fabrication actuator fabrication process. (a) Assembly of outer walls on the base for Mould 1; (b) Pour PDMS pre-polymer in mould cavity; (c) Extract PDMS part from disassembled mould; (d) Fill bottom of base cavity of Mould 2 with partially cured PDMS and then uncured pre-polymer; (e) Align and secure PDMS part on partially cured layer; and (f) disassemble mould to remove completed actuator with a single air inlet through-hole to chamber.....	38
Figure 3.4 (a) Single moulded PDMS actuator; (b) Robotic end-effector with the elastomeric actuators inserted into the gripper assembly (coloured white); Top view of gripper ring in (c) deflated state and (d) moderate inflated state. For the sake of picture clarity, the actuators shown in (c) and (d) of this figure were fabricated out of Ecoflex 00-30. Ecoflex is white while PDMS is nearly transparent.....	39
Figure 3.5 Material data for PDMS from COMSOL Multiphysics' Material Library Module.	41
Figure 3.6 Wireframe of single actuator. (a) Fixed constraint highlighted in yellow; (b) Boundary load to concave deformable wall highlighted in blue; (c) Finite element mesh generated over model geometry and locally refined at concave deformable wall surface.	42
Figure 4.1 (a) Simulated model showing wall displacement due to expansion; (b) top view of simulated model of single actuator with expansion of the principle active wall.	46
Figure 4.2 Simulated displacement (δ_d) values for three expandable wall thicknesses (t_d) at $P_a = 34.47$ kPa.	47

Figure 4.3 Simulated displacement values (δ_d) of different applied pressures (P_a , kPa).	48
Figure 4.4 Displacement (δ_d) as a function of both (a) actuator height (h) and (b) arc angle (α) for $t_d = 2$ mm and $P_a = 6.89$ kPa.	49
Figure 4.5 Simulated surface loads (P_c) with an applied pressure of 34.37 kPa. (a) $t_d = 1.5$ mm; (b) $t_d = 2$ mm; (c) $t_d = 2.5$ mm	50
Figure 4.6 Simulated total elastic strain-energy (U) at different pressures (P_a , kPa).	51
Figure 4.7 Simulated stored energy density (W) at different pressures (P_a , kPa).	52
Figure 4.8 Simulated volumetric strain energy density (W_v) at different pressures (P_a , kPa).	53
Figure 4.9 Simulated isochoric strain energy density (W_{iso}) at different pressures (P_a , kPa).	53
Figure 4.10 Principal strain directions under applied pressures (P_a , kPa). (a) 0 kPa; (b) 68.94 kPa. ..	54
Figure 4.11 Principal strains (ϵ_i) under applied pressure (P_a , kPa) for an actuator wall thickness of $t_d = 1.5$ mm.	55
Figure 4.12 Principal stretches (λ_i) under applied pressure (P_a , kPa) for an actuator wall thickness of $t_d = 1.5$ mm.	55
Figure 4.13 Principal stretches (λ_i) over time for an actuator wall thickness of $t_d = 1.5$ mm.	56
Figure 4.14 Principal stretches (λ_i) over time for an actuator wall thickness of $t_d = 2$ mm.	57
Figure 4.15 Principal stretches (λ_i) over time for an actuator wall thickness of $t_d = 2.5$ mm.	57
Figure 5.1 Experimental setup and test procedure. (a) Testing of a single actuator with a positioning sensor; (b) Sensor data for displacement testing of a single actuator. The dips in the figure show three separate instances of displacement for one test. Note that this the test shown in this figure is performed over a period of 20 seconds. The time period is reduced to 10 seconds after the TrakSTAR system underwent initial calibration.	61
Figure 5.2 Comparison of measured and simulated data for wall displacements (δ_d) for different wall thicknesses (t_d).	62

Figure 5.3 Comparison of experimental and simulation data for wall displacement (δ_d) at different input pressures (P_a) for different wall thicknesses (t_d).....	63
Figure 5.4 Setup for contact force tests. Top view of painted gripper ring in (a) deflated and (b) inflated states; (c) 3D model of contact area on sphere.	64
Figure 5.5 Experimental setup for payload tests. (a) Close-up of spherical target held in gripper; (b) sphere target for payload test; and (c) cylindrical target for payload test.	65
Figure 6.1 Commercially-available vacuum cups provided by Vineland. (a) Bellows-type cup; (b) Bell-type cup.....	71
Figure 6.2 Experimental setup and manual test procedure. (a) Gripper placed over mushroom; (b) Gripper lifting mushroom from threaded rod; (c) Organic test object (i.e., mushroom) embedded on threaded rod.	72
Figure 6.3 Results of grasp-and-hold experiments (success/failure) and observed damage to mushroom surfaces during the tests (damaged/undamaged). These results are for tests with the vacuum cups.	73
Figure 6.4 Observed damage on mushroom cap inflicted by vacuum cup. (a) Indented ring of damage; (b) Inflicted damage outlined with red circle; (c) Bell-type cup geometry collapsing under vacuum pressure.....	74
Figure 6.5 Results of grasp-and-hold experiments (success/failure) and observed damage to mushroom surfaces during the tests (damaged/undamaged). These results are for tests with the soft PDMS gripper variants.	75
Figure A.1 PneuNet Actuator. (a) At rest; (b) Full Actuation; (c) Observed Instability due to ultra-soft hyperelastic Ecoflex 00-30.	93
Figure A.2 PneuNet Gripper. (a) At rest; (b) and (c) show two separate instances of snap-through instability.	94
Figure A.3 Grasping attempt with 4 cm diameter foam sphere. (a) Positioning the sphere between the PneuNet actuators; (b) PneuNet gripper failing to properly hold 4 cm diameter foam sphere by its fingertips.	94
Figure A.4 PneuNet gripper failing to properly hold 6 cm diameter foam sphere by its fingertips.....	95

Figure A.5 PneuNet gripper failing to properly hold the (a) spherical and (b) cylindrical payload rigs by its fingertips.	95
Figure A.6 PneuNet gripper attempting to grasp a soft foam mushroom. (a) Initially succeeding but (b) eventually failing to grasp by its fingertips.	95
Figure B.1 Sketch of vacuum cup operating principle.	96
Figure B.2 Vacuum cup geometries tested. (a) Bellows-type cup; (b) Bell-type cup; (c) Cup Iteration 1; (d) Cup Iteration 2; (e) Cup Iteration 3.	97
Figure B.3 Results of grasp-and-hold experiments (success/failure) and observed damage to mushroom surfaces during the tests (damaged/undamaged). These results are for tests with all vacuum cups.	98
Figure C.1 Basic anatomy of a mushroom (Leeuwen et al. [77], © 1999 Elsevier, included with permission).	99
Figure C.2 Development stages of Agaricus Bisporus in terms of growth (Hammond et al. [79], © 1976 Journal of General Microbiology, included with permission).	100
Figure C.3 Kinematic diagram of PreciseFlex robotic manipulator in use at the Vineland facility. Adapted from PreciseFlex reference manual [80].	102
Figure C.4 Operating principle of Venturi vacuum ejector. (A) Ejector inlet; (B) Venturi nozzle; (C) Sound-reducing silencer; (D) Vacuum connection. As described by the SCHMALZ webpage [82].	103
Figure C.5 Mushroom sample measurements. (a) Cross-section dimensions; (b) Mass measurements with Mettler Toledo digital scale.	105
Figure C.6 Mushroom population for sample measurements (sample size $n = 8$).	106
Figure D.1 CAD of actuator mould assemblies. (a) Mould set for actuator body; (b) Mould set for actuator bottom. Both models shown have the closest wall, nuts, and bolts hidden to provide a view of the mould interior.	108
Figure E.1 Copyright permission statement by IEEE Publisher.	116
Figure E.2 Copyright permission information for confirmation number 11824368.	117

Figure E.3 Copyright permission information for confirmation number 11824388.....	118
Figure E.4 Copyright permission information for confirmation number 11824398.....	119
Figure E.5 Copyright permission information for confirmation number 4611460433957.....	120
Figure E.6 Copyright permission information for confirmation number 11824409.....	121
Figure E.7 Copyright permission information for confirmation number 11824411.....	121

List of Tables

Table 2.1 Properties of PDMS, Sylgard 184, summarized from [39].	13
Table 2.2 Performance summary of actuator designs.	27
Table 2.3 Performance summary of gripper designs.....	32
Table 3.1 Key design parameters used to analyze soft pneumatic actuators during operation.	35
Table 5.1 Contact force and payload test results for all gripper geometries. Test object is a foam sphere unless stated otherwise in brackets.	66
Table 6.1 Standard performance indicators for robotic harvesting systems.....	68
Table 6.2 Comparison of test results for Vacuum Cup and PDMS Soft Gripper performance with reported performance indicators in literature.	77
Table 6.3 Summary of design guidelines.	79
Table C.1 Development stages of Agaricus Bisporus in terms of mushroom cap diameter ranges. Adapted from [74].....	100
Table C.2 Summary of mushroom sample measurements.	105
Table E.1 Summary of Copyright Permission Information. The column labelled “Reference Figure #” may include further annotations in parentheses. These correspond to their labelling within the thesis itself.	115

List of Appendices

A	PneuNet Actuators.....	92
B	Vacuum Cups	96
C	Supporting Information on Mushrooms.....	99
D	Actuator Moulding System CAD & Drawings	107
E	Copyright Permissions	114

List of Abbreviations, Terminology and Nomenclature

Abbreviations

3D	Three-Dimensional
ABS	Acrylonitrile Butadiene Styrene
CAD	Computer-Aided Design
DOF	Degree-of-Freedom
EBPAM	Extensor Bending Pneumatic Artificial Muscle
FEA	Finite Element Analysis
FR	Fiber-Reinforced
NSERC	Natural Sciences and Engineering Research Council
PAM	Pneumatic Artificial Muscle
PDE	Partial Differential Equation
PDMS	Polydimethylsiloxane
PneuNet	Pneumatic Network

Terminology

COMSOL Multiphysics

COMSOL Multiphysics is a cross-platform finite element analysis, solver, and Multiphysics simulation software.

Constitutive model

A constitutive model establishes a close approximation of a material's real behaviour.

Direct farm cash receipt

A direct farm cash receipt represents the cash income received from the sale of agricultural merchandise and direct program subsidy payments.

Green deformation tensor

The Green deformation tensor is a measurement of large displacements and deformations as strain in material coordinates.

Gripper

A gripper is a type of end-effector or tool end on robotic manipulator systems. Situated at the end of the manipulator arm, the gripper's purpose is to grasp a target object.

Hooke's law

Hooke's law states that, for linear materials, the strain in a solid is proportional to the applied stress within that solid's elastic limit.

Hyperelastic material

A hyperelastic material is capable of large deformations under small loads. It is not characterized by Hooke's law.

Inert

An inert material has properties that make it chemically inactive.

Mooney-Rivlin

The Mooney-Rivlin model is a type of hyperelastic constitutive material model.

Principal strain

A principal strain has a maximized normal vector.

Principal stretch

A principal stretch has a maximized normal vector.

Soft lithography

Soft lithography is a classification of techniques for fabricating or replicating elastomeric structures that includes stamps, open, and closed cavity moulding.

Soft robotics

The field of soft robotics covers robotic systems that implement inherent or material compliance.

Surfactant

A surfactant is a chemical solution that reduces adhesion between mould surfaces and pre-polymer mixtures by reducing surface tension of a fluid.

Thermosetting

A thermosetting material has properties that are permanently set when heated.

Venturi principle

The Venturi principle is the reduction in fluid pressure resulting when a fluid flows through a constricted pipe section.

Viscoelastic

A viscoelastic material exhibits both viscous and elastic behaviour when deformed.

Nomenclature

A_c	Contact area
C_{ii}	Material constants
$F_{buoyancy}$	Buoyancy force
F_c	Contact force
I_i	Principal strain invariant ($i = 1, 2, 3, \dots$)
K_1	Bulk modulus
P_a	Applied pressure
P_c	Contact pressure
V_b	Volume of submerged body
$W_{iso}(f)$	Isochoric term, strain-energy density
$W_v(f)$	Volumetric term, strain-energy density
l_o	Original length
m_L	Slip test payload mass
t_d	Thickness of deformable wall
t_r	Thickness of rear wall
δ_d	Displacement at center of actuator wall
λ_i	Principal stretch ratio, ($i = 1, 2, 3, \dots$)
μ_i	Ratio of shear modulus

σ_i	Principal stress ($i = 1, 2, 3, \dots$)
ϵ_i	Principal strain ($i = 1, 2, 3, \dots$)
$^{\circ}\text{C}$	Degrees Celsius
$^{\circ}\text{F}$	Degrees Fahrenheit
h	Actuator chamber height
A	Area
E	Young's Modulus
F	Force
J	Elastic volume ratio
U	Strain-energy
W	Strain-energy density
d	Actuator chamber depth
g	Gravity
l	Final length
ΔA	Change in cross-sectional area
ΔF	Difference in force
ΔU	Difference in strain-energy
ΔV	Difference in volume
α	Arc angle

μ	Shear modulus
ν	Poisson's Ratio
σ	Uniaxial stress
ϵ	Material strain

Chapter 1

Introduction

Soft robotics can be defined as the research field covering robotic systems that interact with their environment by relying on inherent or structural compliance [1]. Soft-material robotics is a specific branch of this field that studies inherent material compliance, and how deformation of a soft material can be controlled to achieve robotic functionality. A common feature of soft materials, whether they be liquids, gels, polymers, etc., is that they consist of large molecules or assemblies of molecules that move collectively. As a result, they provide a large, slow and nonlinear response to small forces [1]. Most research on soft-material robotics focuses on materials with a low Young's modulus (< 1 GPa) at ambient temperature [1], [2].

Soft robotic grippers can elastically deform to grasp irregularly shaped, delicate organic objects. In contrast with rigid robotic end-effectors that apply point forces on a target, soft grippers can distribute contact forces over a broader surface area, thereby minimizing contact damage to delicate organic structures. Soft robotic grippers can be based on a number of different operating principles including tendon-driven tension, particle jamming, and fluidic actuation [3]. Pneumatic actuation is commonly used because air is nearly inviscid and compressed air can be stored and dispensed at precisely controlled amounts [4]–[7]. During operation, the applied pressurized air causes the inflation and deformation of one or more inner cavities (i.e., chambers) embedded in the actuators of the grasping mechanism. Air-driven soft actuators can have multipart geometries fabricated from hyperelastic materials such as synthetic rubbers or silicone polymers [5] that have

very nonlinear stress-strain properties, making it difficult to predict the actuator's behaviour. In many cases, the elastomeric materials used are commercially branded as special effects rubber for prosthetics in the performing arts, and thus the material data is rarely outlined. As a consequence of the inherent nonlinearity and lack of available material properties, most soft robotic grippers must be developed through an iterative design process based on trial-and-error experiments.

1.1 Research Motivation

There is an economic incentive to improving the design process of soft robotic grippers for horticultural product harvesting. A 2017 symposium report published by Vineland Research and Innovation Centre Inc. states that there are over 27,500 horticulture farms in Canada, covering approximately 1 million acres of land and producing \$5 billion in annual direct farm cash receipts [8]. In the 5 years prior to the report, Ontario had accounted for nearly 60% of Canadian horticulture sales each year [8]. Labour costs take a significant toll on the horticulture sector, being as high as 40-50% of the cost of goods [8], [9]. In addition, a diminishing labour pool is recognizable in as early as 2014 when the industry was unable to fill 5,800 employment positions. This cost the industry over \$350 million, with 60% of field-fruit and vegetable farms reporting sales losses. The shortage is projected to increase by 2025, and it is expected that 32-45% of the horticulture sector's labour demands will not be met by domestic workers [8].

Shifting from manual labour to robotic automation has reduced the previously significant impact of labour costs and availability. Robotic automation has seen notable use in the harvesting of high-value crops; non-staple produce that typically require a high manual labour input [10]. Each type of automated system faces unique design requirements and constraints that are dependent of the harvested crop. For soft fruits and vegetables, it is important that a system's end-effector can collect the produce without damaging its delicate structure [11]. Noticeable damage to any produce significantly reduces the quality of the crop yield, in turn diminishing farm profits. Automated, robotics-based harvesting systems have also faced challenges in the mushroom farming industry [12]–[21].

Mushrooms have a very delicate body that can be easily damaged by conventional gripper designs. They do not grow in neat, orderly lines. Instead, they spread across large growing beds, packed together by the thousands. Conventional rigid end-effectors are ill-suited for the manipulation of delicate organic objects in such a dense environment, as they are likely to damage both the collected target and mushrooms growing adjacent to it.

Prior attempts have been made to eliminate the rigid end-effector by employing robotic vacuum end-effectors [12]–[14], [16]–[22]. In theory, a non-rigid suction cup with a soft sealing base can deform around a mushroom cap’s irregular geometry and pull it from its growing bed. This method has proven only partially successful, as gripping forces applied to the cap surface can still be excessive due to the limited contact area of the suction cup. Conventional cups have a fixed open diameter which require accurate positioning over the cap. Misalignment can lead to further damage. Optimizing the conventional suction cup designs are not likely to fully eliminate damage inflicted to the mushroom due to the high variability in mushroom size, orientation, and cluster density.

1.2 Objectives of Research

The primary objective of the research reported in this thesis is to provide a possible solution to the modelling limitations pertaining to soft robotic actuators by presenting a compact, single Degree-of-Freedom (DOF) geometry for a soft pneumatic actuator. To bypass the lack of material data available for typical ultra-soft materials used, the actuator geometry is fabricated with polydimethylsiloxane (PDMS), a better-known and therefore more predictable hyperelastic material frequently seen in microfluidics research. Choosing the more predictable PDMS as the actuator material allows the geometry to be modelled in nonlinear simulation software, specifically COMSOL Multiphysics. Simulations performed focus on analyzing the impact of geometrical parameters on the simple and straightforward actuator geometry to assess its performance prior to fabrication. Optimal geometric parameters can then be selected for the improved design of an actuator to be fabricated, resulting in fewer design iterations required. Performance of these actuators can then be verified experimentally in a laboratory environment, establishing a new and comparative method of optimizing actuators for soft robotics.

In collaboration with the Vineland Research and Innovation Centre Inc., this research also aims to investigate the validity of these actuators in a proposed soft gripper design by comparing their performance to both commercial and custom vacuum cup geometries for automated mushroom harvesting. The target fungi in question is *Agaricus Bisporus*, more commonly known as the white mushroom. Although literature exists on numerous attempts at designing and optimizing systems and methods for automated mushroom harvesting, little is found on the implementation of soft robotics in this field. Thus, the secondary objective is to investigate the proposed soft gripper design's viability for this application. By comparing the gripper design to both standard and modified vacuum cup geometries, the validity of the proposed design can be evaluated. In addition, modifying existing cup geometries proves that attempting to optimize vacuum cup systems will not fully resolve the issues related to mushroom harvesting.

1.3 Major Contributions

This thesis provides the following major contributions to the scientific community:

- *Starting foundation for hybrid computational/experimental design of soft robotic grippers and actuators.* A comparative method of assessing the performance of soft robotic actuators made of hyperelastic materials. This has been achieved through the classification of key parameters for analysis and comparing the impact of changing these parameters using nonlinear simulation software and experiments. This reduces the number of iterations required to be fabricated throughout the design process.
- *Pneumatically-driven soft robotic gripper for automated mushroom harvesting.* Optimal geometrical parameters are selected in the fabrication of compliant soft PDMS grippers and combined with a rigid housing structure to enable the grasping and collection of delicate objects in experiments that simulate mushroom harvesting. The gripper design not only allows for damage-free mushroom handling but also serves as a potential replacement for vacuum cup end-effectors currently in use.

- *Established summary of design guidelines for soft robotic grippers.* A summarized set of design guidelines for adapting the proposed gripper structure for various applications. These guidelines provide instruction on which parameters to modify to redesign the soft compliant end-effector for grasping different targets.

1.4 Thesis Organization

This thesis is organized into seven chapters. The following chapter, Chapter 2, *Background and Literature Review* provides a detailed overview of the knowledge and information researched in this thesis. After an introduction to hyperelastic material theory, the chapter discusses relevant work on soft robotic technology, including the fabrication and operating principles of various soft actuators and grippers. Chapter 3, *Design Methodology and Fabrication* presents the geometric overview of the compliant soft actuator and corresponding gripper structure. The chapter also provides the actuator design's fabrication process, and model generation and setup in COMSOL Multiphysics. Chapter 4, *COMSOL Simulations and Results* describes the hyperelastic studies performed and their resulting data. Chapter 5, *Experimental Setup and Testing* goes over the experiments performed and the comparison of their resulting data with the previous chapter's simulation results. Chapter 6, *Application Study and Discussion* demonstrates the proposed design's performance in terms of mushroom harvesting. Previous work on harvesting systems is presented. The systems are first discussed in general terms, followed by an overview of mushroom harvesting systems that utilize vacuum cups. A comparison is then made between the proposed gripper design and existing vacuum cups. The chapter also discusses results of simulation studies and experimental tests and summarizes design guidelines to modify the gripper design for different applications. Finally, Chapter 7, *Concluding Remarks* summarizes the primary conclusions of the thesis and provides recommendations for future work.

Chapter 2

Background and Literature Review

This chapter first provides an introduction to hyperelastic material theory. It also provides relevant background information on soft robotics technology, with a focus on air-driven soft material actuators and grippers. Additional background on the intended application, mushroom harvesting, is presented in this thesis. However, the goal of this chapter is to provide the necessary information fundamental to understanding soft robots and their functionality. Robotic harvesters in horticulture are presented at the beginning of Chapter 6. All additional information related to mushrooms is available in Appendix C.

2.1 Hyperelastic Theory

Most silicone-based elastomers are considered to be hyperelastic. That is, materials that are capable of experiencing large deformations under small loads and then return to their original shape without any significant plastic deformation once that load is removed [23]. Hyperelastic materials, such as solid rubber, are close to ideally elastic. When deformed at constant temperature or adiabatically, stress is solely a function of current strain. It is independent of the history or rate of loading [24]. The stress-strain behaviour of a hyperelastic material is very nonlinear, meaning that the material's elastic modulus is not enough to characterize its elastic behaviour (Figure 2.1) [25], [26]. A constitutive mathematical model is therefore necessary to represent the real behaviour of a hyperelastic material [23], [25], [27]. These hyperelastic models can be used with materials that undergo

large deformations, taking into account intrinsic (relating to the material microstructure) and geometric (relating to the material's shape) nonlinearities [28], [29].

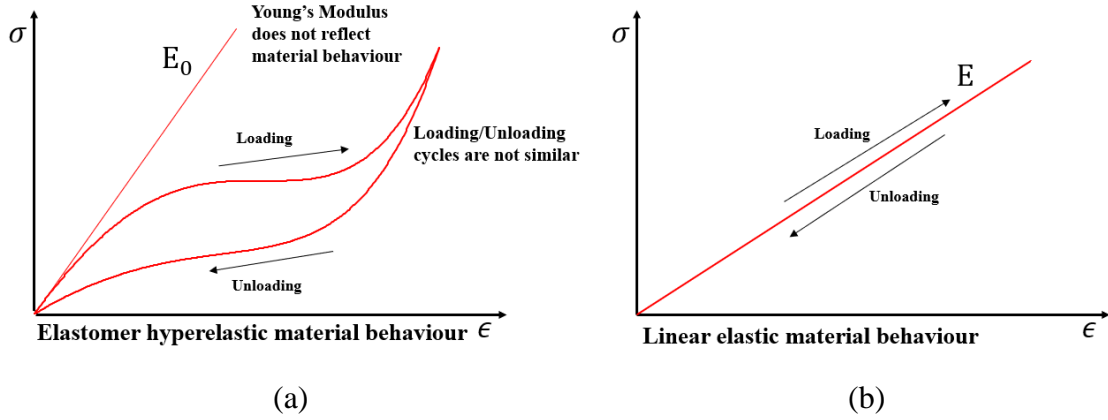


Figure 2.1 Stress-strain curve during a loading cycle. (a) Elastomer hyperelastic material behaviour; (b) Linear elastic material behaviour. Note that the Young's moduli are not to scale. As described by [24], [26], [27].

2.1.1 Governing Equations

A material tends to store energy internally throughout its volume as it is deformed by an external load. This internal energy is related to material strain and is known as the strain-energy. Consider an object under tension, where a volume element of the object is subjected to a uniaxial stress (Figure 2.2a) [30].

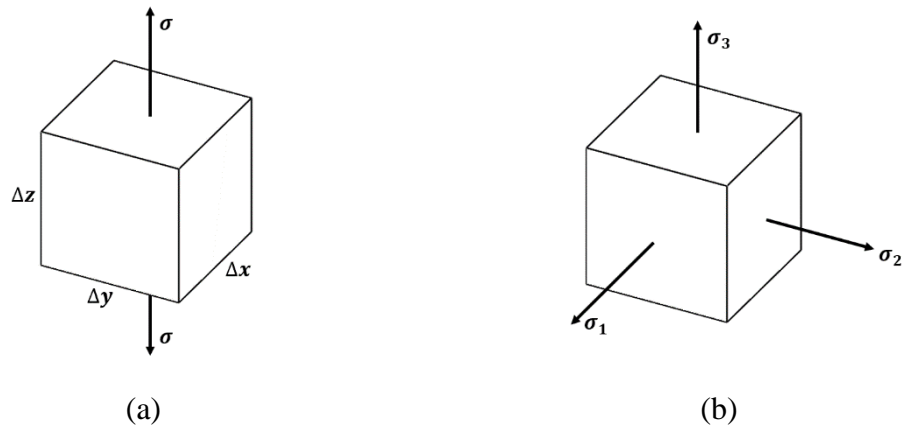


Figure 2.2 Volume element subjected to (a) uniaxial stress (σ) and (b) principal stresses.

This stress in turn develops a force on the top and bottom faces of the element once it undergoes a displacement. The difference in these forces is defined by

$$\Delta F = \sigma \Delta A = \sigma(\Delta x \Delta y) \quad (2.1)$$

where (σ) is the uniaxial stress and (ΔA) is the change in cross-sectional area of the element normal to the stress, after the element of length Δz undergoes a vertical displacement. Work is defined by the product of the force and related displacement. Since force is uniformly increased from zero to its final magnitude when this displacement is reached, the work done by the force on the element is equal to the product of the average force magnitude and the displacement. With the assumption of no energy loss, the external work becomes equal to the internal energy, also known as the strain-energy stored in the element. Therefore, the strain-energy can be defined by

$$\Delta U = \left(\frac{\Delta F}{2} \right) \epsilon \Delta z = \frac{1}{2} \sigma \Delta A \epsilon \Delta z \quad (2.2)$$

$$\Delta U = \frac{1}{2} \sigma \epsilon \Delta V \quad (2.3)$$

where (ϵ) is the strain and $(\epsilon \Delta z)$ is the material element's vertical displacement. Equation (2.3) can be rewritten to formulate the strain-energy per unit volume of material. This is known as the strain-energy density.

$$W = \frac{\Delta U}{\Delta V} = \frac{1}{2} \sigma \epsilon \quad (2.4)$$

Now consider this same volume element, now subject to three principal stresses (Figure 2.2b). Equation (2.4) can be rewritten such that each principal stress contributes a portion of the total strain-energy density.

$$W = \frac{1}{2} \sigma_1 \epsilon_1 + \frac{1}{2} \sigma_2 \epsilon_2 + \frac{1}{2} \sigma_3 \epsilon_3 \quad (2.5)$$

For linear-elastic material behaviour, Hooke's law applies, and these formulas can be rewritten in terms of the material's Young modulus. However, the stress-strain behaviour of a rubber-like material such as PDMS is highly nonlinear and, therefore, the material's

elastic modulus is not sufficient for characterizing their behaviour when dealing with large deformations. A constitutive model is required for simulating the true behaviour of the hyperelastic material and associated structures at high strains [23], [25], [27], [28]. A suitable constitutive model can be derived from a strain-energy density function (W) that represents the energy stored in the material per unit volume of the original geometry as a function of strain at that point in the material. Mathematically, this relationship is defined as [23]

$$W = f(I_1, I_2, I_3) = f((\lambda_1^2 + \lambda_2^2 + \lambda_3^2), (\lambda_1^2 \lambda_2^2 + \lambda_2^2 \lambda_3^2 + \lambda_3^2 \lambda_1^2), (\lambda_1^2 \lambda_2^2 \lambda_3^2)) \quad (2.6)$$

where I_1, I_2 , and I_3 are the three strain invariants of the Green deformation tensor. The individual strain invariants are a function of the principal stretch ratios ($\lambda_i, i = 1, 2$ and 3).

The stretch ratio is a measure of the extensional strain that is normal to a material line element. It can be defined within either the natural or deformed state as the ratio between the final and initial lengths of the material line. In other words,

$$\lambda = \frac{l}{l_0} = \frac{l - l_0 + l_0}{l_0} = \epsilon + 1 \quad (2.7)$$

where l is the final length, l_0 is the original length, and ϵ is the material strain. Stretch invariants are the properties by which the hyperelastic model can have a non-zero solution.

The third invariant term given by equation (2.6) is related to the elastic volume ratio (J) by $I_3 = J^2$. Introducing the volume ratio term enables a more convenient constitutive model to be developed for nearly incompressible materials where

$$\bar{I}_1 = \frac{I_1}{J^{2/3}} \quad \text{and} \quad \bar{I}_2 = \frac{I_2}{J^{4/3}} \quad (2.8)$$

and where \bar{I}_1 and \bar{I}_2 are assumed to remain constant under a pure volume change.

The strain-energy density of a material (W) given by equation (2.6) can be written as the sum of two parts [27]. The first part is the isochoric term, $W_{iso}(f)$, which represents the energy needed to deform or distort the element while preserving volume. The second part represents the energy needed to cause a change in volume of the element with no

change in shape and is known as the volumetric term, $W_v(f)$. The strain-energy density can therefore be given as

$$W = W_{iso}(\bar{I}_1, \bar{I}_2) + W_v(J) \quad (2.9)$$

where $J = \sqrt{I_3}$. By assuming an incompressible material, $J = 1$.

In this study, the Mooney-Rivlin model [23], [25], [27] is used to simulate the hyperelastic behaviour of the PDMS material used in the pneumatically-driven soft actuators. The generalized form of strain-energy density is given by

$$W = \frac{\mu_1}{2}(\bar{I}_1 - 3) + \frac{\mu_2}{2}(\bar{I}_2 - 3) + \frac{K_1}{2}(J - 1)^2 \quad (2.10)$$

where μ and K_1 are the shear and bulk moduli of the solid, respectively. In this case, $\mu_1 = C_{10} = \frac{7}{16}\mu$ and $\mu_2 = C_{01} = \frac{1}{16}\mu$. Correspondingly, the shear modulus is $\mu = 2(C_{10} + C_{01})$. The material constants C_{10} and C_{01} are set as such to fulfill the approximation for rubber-like materials of $C_{10} = 7C_{01}$ [27], [31], [32].

Other hyperelastic models were available. From an experiment described in the textbook by Holzapfel [27], the Mooney-Rivlin model is used in comparison with the Neo-Hookean, Varga, and Ogden models for the inflation of a rubber spherical balloon. The simplified Neo-Hookean and Varga models are capable of reproducing the real behaviour of the deforming hyperelastic shape for small strains. However, neither model is capable of tracking the local maximum and minimum displacement values for pressure, known as limit points. The Mooney-Rivlin and Ogden models are capable of showing these points. The Ogden model provides a more realistic approximation of the balloon's deformation; however, it requires additional parameters that are beyond the capabilities and scope of this work. Thus, the Mooney-Rivlin model was selected.

2.2 Polydimethylsiloxane (PDMS)

2.2.1 Ultra-soft, Unpredictable Elastomers

Pneumatically-driven soft actuators have been fabricated from a variety of commercially available silicone elastomers like Ecoflex™, DragonSkin™ and pre-made tubes of commercial silicone [33]. Although these elastomeric materials are ultra-soft and can be moulded into single and multi-chambered actuators, they were developed for non-scientific applications like theatrical prosthetics and, therefore, very little information is available about their underlying engineering properties. Furthermore, these ultra-soft materials exhibit inconsistent hyperelastic behaviour under pressurization making it very difficult to analyze fabricated chambers either through simulation or controlled repeatable experiments.

Ultra-soft elastomers are susceptible to modes of instability such as snap-through buckling, a bi-stable form of nonlinear buckling common in ultra-soft elastomers and thin-walled geometries [34], [35]. At high air pressure inputs, the elastomeric chambers undergo large deformations at an accelerated and unstable rate. The actuator chamber walls are more susceptible to buckling under these conditions, where the displacement under load will “snap-through”. When this occurs, the actuator’s chambers will exhibit a sudden and significant change in geometry before stabilizing at a new configuration [36]. Removing the pressure causes the chamber geometry to revert to its original stable form, or “snap-back”.

In contrast, polydimethylsiloxane (PDMS) is a flexible silicone-based organic polymer that is used extensively in scientific research due to its viscoelastic, thermosetting and inert properties [37], [38]. The predictable and known material properties of PDMS make it a viable hyperelastic material for computational simulation on COMSOL Multiphysics software and enable a deeper understanding of the impact of geometric design parameters on actuator performance.

2.2.2 Properties of PDMS

PDMS is a mineral-organic polymer, with a structure that contains both carbon and silicon, from the siloxane family (silicon, oxygen, alkane) [25]. The brand used in this research, Sylgard 184, is available as a fluid monomer base and curing agent. To fabricate solid PDMS, the liquid base is mixed with the cross-linking agent and then poured into a mould to create the desired geometry. The empirical formula (Figure 2.3) of PDMS is $(C_2H_6OSi)_n$, and the fragmented formula is $CH_3[Si(CH_3)_2O]_nSi(CH_3)_3$, where n is the number of monomer repetitions in the polymer chain [25].

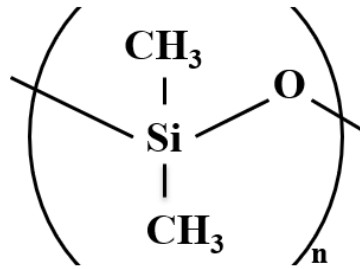


Figure 2.3 Empirical formula of PDMS. As shown on Sigma-Aldrich [39].

Properties of PDMS can be tuned and adjusted by varying the mixing ratio between the monomer base and cross-linking agent [40], curing temperature [41], and cure time. Kim et al. [40] investigated the nonlinear mechanical properties of Sylgard 184 in relation to the base/agent mixing ratio. They found that the amount of curing agent used will influence the elastic properties of PDMS, with more curing agent resulting in a hard PDMS and less agent creating a softer elastomer, both with differing stress-strain curves. Johnston et al. [41] investigated the mechanical properties of Sylgard 184 PDMS with regard to curing temperatures ranging from 25 °C to 200 °C. A linear relationship between the elastic modulus, E , and the curing temperature is shown. Note that letting PDMS cure at 25 °C (room temperature) requires at least 48 hours before a solid elastomer is formed. Liu et al. [42] investigated the mechanical properties of Sylgard 184 PDMS in relation to long cure times at high temperatures (100 – 500 °C). They found that longer cure times at temperatures greater than 200 °C drastically reduce the mechanical strength of PDMS. This

reduction is attributed to thermal decomposition, which starts at 200 °C and reaches a peak at 310 °C. Work by McDonald and Whitesides [43] summarizes the material properties of Sylgard 184 PDMS, shown in Table 2.1.

Table 2.1 Properties of PDMS, Sylgard 184, summarized from [43].

Property	Characteristic	Consequence
Mechanical	Elastomeric; tunable Young's Modulus $E = 0.75 \text{ MPa} - 4 \text{ MPa}$	Conforms to surface; allows actuation by reversible deformation; facilitates release from moulds
Thermal	Insulating; thermal conductivity, $0.2 \text{ W}(m \cdot K)$; coefficient of thermal expansion, $310 \mu\text{m}/(m \cdot ^\circ\text{C})$	Can be used to insulate heated solutions; does not allow dissipation of resistive heating from electrophoretic separation
Interfacial	Low surface free energy $\sim 20 \text{ erg}/\text{cm}^2$	Replicas release easily from the mould; can be reversible sealed with materials
Permeability	Impermeable to liquid water; permeable to gases and nonpolar organic solvents	Contains aqueous solutions in channels; allows gas transport through the bulk material; incompatible with many organic solvents

The established and well-documented procedures for creating softer or harder PDMS elastomer structures provide control on the fabrication processes for creating functional soft hyperelastic pneumatic actuators. For the purposes of this research, a 10:1 base/curing agent mixing ratio is used with a thermal cure at ambient temperature for 48 hours. As an elastic material, PDMS can withstand repeated loading. However, it is not as deformable as ultra-soft Ecoflex 00-30. Under bending load, PDMS will fracture above a maximum strain of 150%, whereas Ecoflex 00-30 will only fracture above a maximum strain of 900% [6]. An alternative elastomer comparable to PDMS, in terms of material properties, is RTV 615 Silicone [44]. Sharing similar material and mechanical properties, RTV 615 is better suited for optical applications than Sylgard 184 PDMS [45], and was thus not acquired for this research..

2.2.3 Importance of Degassing PDMS

Uncured PDMS is in the form of a thick liquid with a viscosity of approximately $3.5 \text{ kg/m}\cdot\text{s}$ [39]. This means that the fluid is susceptible to trapped gas bubbles before curing. Sylgard-184 PDMS is sold as a kit containing a monomer base and curing agent and mixing these two compounds together creates many air bubbles. Once the PDMS is cured, any bubbles that haven't dissipated will remain trapped in the solid geometry, creating points of weakness in the actuator structure. Even worse, an air bubble that creates a hole through any of the actuator walls renders the whole geometry useless. Therefore, it is critical that all gas bubbles be completely removed before the PDMS can cure.

Techniques exist to improve the removal of gas bubbles from the uncured PDMS mixture by increasing the buoyant forces that the viscous liquid exerts upon them. The buoyancy force acting in the opposite direction of gravity, g , of a submerged body [46] is given by

$$F_{buoyancy} = \rho_f V_b g \quad (2.11)$$

where ρ_f is the density of the fluid and V_b is the submerged body's volume. Vacuum degassing is the most common method of degassing PDMS. It is used in microfluidics [37], [38], as well as existing soft robotic [47], [48] literature where open cavity moulds are placed in a vacuum chamber. The mixed and heavily-aerated PDMS then becomes subject to negative pressure. The trapped air bubbles, previously at atmospheric pressure, now expand in volume. This also increases the exerted buoyant force in equation (2.11). Degassing with a vacuum chamber may require a long time to fully remove all bubbles depending on the initial number of bubbles present, the vertical distance they must rise to reach the surface, and wall friction effects.

Agitating the mixture by stirring or pouring can create tiny gas pockets which must be removed. Vacuum degassing is a common and proven method of removing any trapped gasses, though with a fluid as viscous as PDMS it can take over an hour. Any further agitation after the PDMS is degassed can introduce new bubbles to the mixture. Given the

multi-step moulding techniques described in Chapter 3 of this work, multiple degassing sessions are therefore necessary.

2.2.4 Removing PDMS from a Mould

Chapter 3 will present the multi-step moulding techniques used to fabricate the soft PDMS actuators. Extracting the part from the mould is a crucial and delicate process to preserve the overall quality of the demoulded geometry. For soft actuators, any defects, cuts or tears due to careless or improper removal techniques greatly diminishes, if not fully ruins, the functionality of the device. As mentioned in Table 2.1, the elastomeric properties of PDMS make fabricated geometries easy to peel off a complex master pattern. However, this is assuming that there is little-to-no adhesion between the PDMS and mould surface. Soft pneumatic actuators require much larger moulds compared to conventional microfluidics work, resulting in greater contact between the PDMS and multiple complex surface geometries. If enough adhesion between the mould surfaces and the PDMS part exists, actuator features may bond to the mould surface and tear when removal is attempted. Unwanted adhesion may result in high strains on the PDMS geometry during removal, which may cause permanent deformation.

A common method for preventing damage during part removal is to apply a thin layer of anti-adhesion coating to the mould surfaces. Commonly known as a surfactant, release agent or demoulding agent, these coatings lower the mould's surface energy to prevent the PDMS from bonding. Silane anti-adhesion layers are commonly used as release agents for PDMS fabrication in microfluidics. They are typically applied with vapour deposition on SU-8 or PDMS when master patterns are used and need to last for a limited number of soft lithography replications. Friend et al. [37] used gaseous dimethyloctadecylchlorosilane in vacuum conditions to form a thin anti-adhesive monolayer on SU-8 patterns. Work by Chen et al. [49] uses (tridecafluoro-1,1,2,2-terahydrooctyl)-1-trichlorosilane on PDMS patterns, while both Con et al. [50] and Zhang et al. [51] use trichloro-(1, 1H, 2H, 2H-perfluorooctyl)silane on SU-8 and PDMS patterns. It is important to note however, that when a material like a rigid polymer is used to fabricate the mould or master pattern, silane-based release agents can chemically interact with the polymer. This can cause cracking or

structure warping, depending on the combined polymer and silane agent. Silanes can also be hazardous and costly. Chang-Yen et al. [52] proposes a safer and more cost-effective solution by replacing the silane agent with an industrial cleaning solution. The work found that a detergent-based agent on SU-8 patterns performed with greater success than silane agents.

2.2.5 Partial Moulding Techniques

The multi-step fabrication technique mentions partially curing the PDMS in some steps, where the PDMS is cured for only half the required time. In this case, the PDMS has only just solidified and its surface still contains bondable polymer chains. More uncured PDMS can be poured over this surface, and this will bond with the surface's available polymer chains. Work by Eddings et al. [53] states that partial curing showed the highest bond strength compared to any other bonding technique.

2.3 Soft Robotics Technology

Research on soft-material robotic grippers using soft elastomers can be dated back to the late 1980s and early 1990s [1]. One of the first pieces of published work for a continuously-deforming elastomeric geometry is by Wilson and Mahajan in 1989 [54]. They present a pneumatically-driven arm made of soft elastomeric bellows. The attached grippers are made of additional bellows to create a soft robotic assembly. The actuation and bending of these bellows allowed the arm to perform pick-and-place operations of irregularly shaped objects [1], [54]. Other pieces of critical work include research by Suzumori et al. [55], [56]. In this research, the bellows-like actuators are replaced with novel tri-cellular units. The three cells are distributed about a central axis, each spanning 120° . The precise configuration of these units could be implemented in gripper designs and hexapod walkers for object manipulation and soft robotic locomotion [1], [55], [56].

Though the basic concepts behind pneumatically-actuated soft grippers have remained the same, the overall field of soft-material robotics has changed with the development and

improvement of new technologies. Interest in the field has rekindled in the early 21st century since the establishment of soft materials as a field of material science research in the early 1990s. Many new soft materials have been created and made available on a commercial scale. The development of diverse fabrication techniques for soft materials, and the level of accessibility of these techniques, has increased. An increase is also noted in the magnitude of the research and work, published in high-profile journals, that demonstrate the use of soft materials in robotic applications. Overall, it is generally agreed in the relevant scientific community that soft robotic technologies can and should be used in future robotic applications where they would provide a naturally cheaper, safer, and more adaptive solution for intricate applications in unstructured environments as opposed to conventional rigid systems [57].

2.3.1 Review of Soft Pneumatic Actuators

Also known as Fluidic Elastomer Actuators, soft pneumatic actuators are one of the most common and widespread soft robotic design. During operation, the applied pressurized air causes the inflation and deformation of one or more inner chambers (i.e., cavities). These actuators are typically fabricated from ultra-soft and highly deformable materials including synthetic rubbers or silicone polymers and elastomers [3], [5]. Soft lithography techniques and the integration of soft composite materials (i.e., embedded strain-limiting membranes) are combined to fabricate the soft actuator structure and predict its motion [2]. Predicting actuator behaviour is further improved with design asymmetry and the careful selection of constituent materials.

2.3.1.1 Pneumatic Networks

Designed by the Whitesides Research Group at Harvard University, Pneumatic Networks (PneuNets) consist of a series of chambers connected by a long channel, all embedded within an extensible elastomeric layer [4]. This compliant structure is bonded to an inextensible layer that includes an embedded film of non-stretching but flexible material like cloth or paper. A single air input pressurizes the structure, causing the chambers to

expand and press against each other. This creates a difference in strain between the extensible and inextensible layers, resulting in a directional bending motion (Figure 2.4). The PneuNet actuator is meant to approximate the behaviour of a biological finger. Each additional inflating chamber within the PneuNet corresponds to an additional bending DOF. With the use of ultra-soft elastomers, the actuator can have an infinite number of DOF [58]. The principle behind the PneuNet's bending motion has been implemented in a number of applications including multigait movement [5], medical rehabilitation devices [59], and the manipulation of various objects [58].

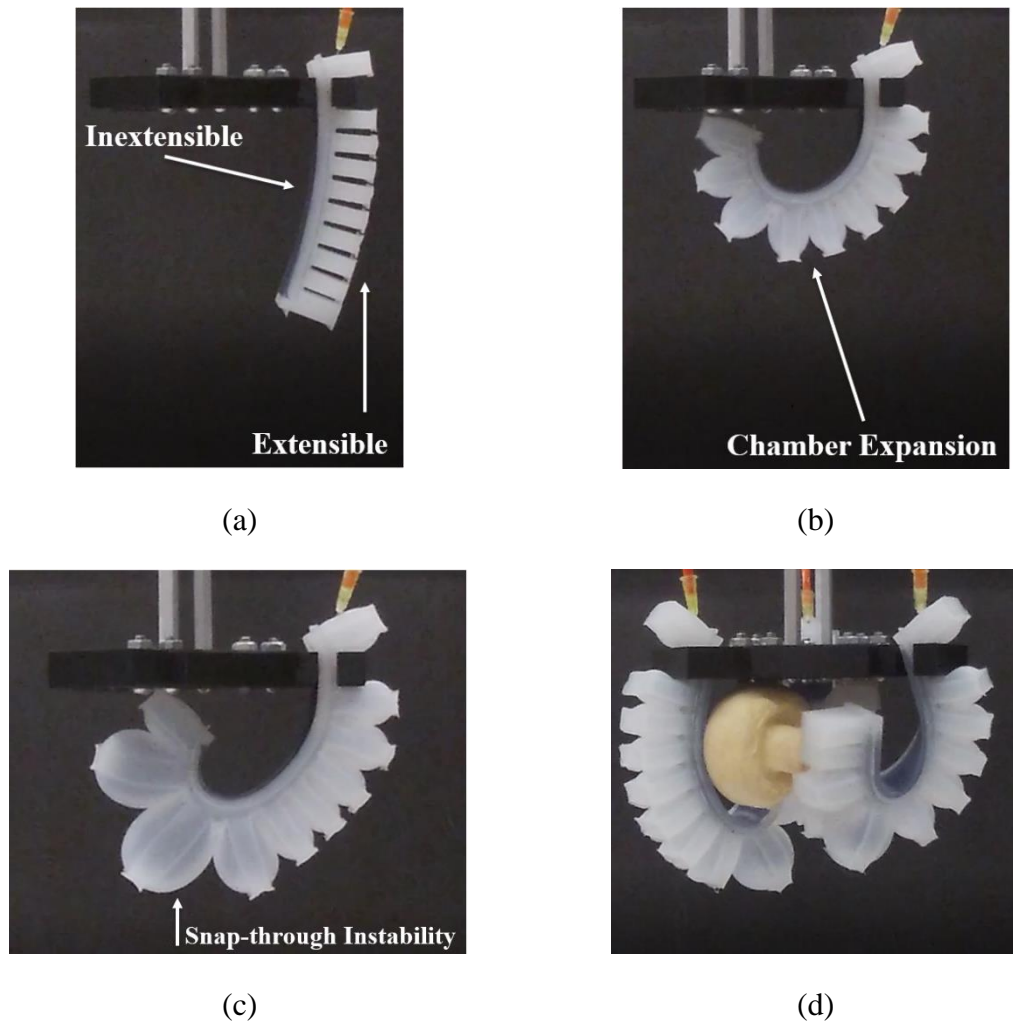


Figure 2.4 Pneumatic Network soft bending actuators. (a) Deflated state; (b) Inflated State; (c) Ultra-soft material instability; (d) Limitations as a gripper design for the research application. Note that the actuators shown in this figure were fabricated as part of preliminary work for this research thesis.

The most recent PneuNet design by Mosadegh et al. [4], of which a custom fabrication is shown in Figure 2.4, investigates the impact of reducing the expansion volume of the structure by adding gaps between the chambers. Less material between the chambers allow the chamber walls to expand preferentially under pressure, reducing the deformation and strain on portions of the structure not critical for bending. The study shows that reducing the expansion volume increases the speed at which the actuator bends (the actuation speed) and reduces the operating pressure for full actuation. The reduced deformation and operating pressure in turn reduce the material strain, significantly improving the actuator's durable life. However, these improvements come at the reduction of applicable tip forces.

The lower operating pressures reduce the actuator's contact forces, consequently diminishing the structure's payload capabilities as a gripper. The work also studied the impact of using different materials. The original design is fabricated with Ecoflex 00-30 and PDMS as the extensible and inextensible layers, respectively. Replacing the soft Ecoflex with a stiffer elastomer (Elastosil M4601) showed that while stiffer material geometries required significantly more pressure to fully actuate (approximately 8X more), a smaller change in volume is needed (approximately 1.5X less) to bend completely. It was also shown that the greater expansion volume required with softer material geometries is a direct consequence of the additional and extraneous expansion of non-critical actuator sections (i.e., walls not used in the bending motion). This means that actuators fabricated from a softer elastomer have a reduced actuation speed and apply lower tip forces for a given inflation pressure as compared to the same structure made with a stiffer material [4].

Performance parameters for the PneuNet design are established by Mosadegh et al. [4]. They are:

1. Speed achieved for a given rate of inflation.
2. Force exerted for a given pressure.
3. Change in volume required for a given degree of bending.
4. Number of actuation cycles before failure.
5. Correlation between actuation pressure and degree of bending without a load.

Two major limitations are present in Mosadegh et al.'s design. The length and size of the PneuNet structure, combined with the lack of material between the inflating chamber walls, cause the actuator to bend slightly under gravity. In addition, the actuator's chambers may not expand simultaneously and uniformly when pressurized above a certain threshold (200 kPa). This is due to snap-through instability, as mentioned in Section 2.2.1.

Soft Robotics Toolkit, the website created for educational purposes by the Harvard Biodesign Lab, provides several methods of fabricating soft robotic sensors and actuators [60]–[62], including a simple method of creating a basic PneuNet actuator. As previously explained, the PneuNet actuators are composed of two parts; the top extensible body containing the chambers that deform when the actuator is pressurized, and a bottom inextensible layer containing a strip of strain-limiting material. These two parts are fabricated separately in specific mould geometries before being bonded together. The webpage discusses fabrication of the PneuNet with Ecoflex 00-30 as the hyperelastic material, a strip of paper as the strain-limiting layer and suggests using an oven to accelerate the curing process. The work by Mosadegh et al [4] elaborates on the fabrication process for the most recent PneuNet design in a supporting document [7]. Moulds are made of acrylonitrile butadiene styrene (ABS) polymer with a three-dimensional (3D) printer. Three mould parts are used: interior and exterior pieces for the top body, and a flat rectangular mould for the inextensible bottom. The flaw with this method lies in the strain-limiting material used. Paper strips are prone to tearing and can break down when submerged in a fluid (i.e., the elastomer mixture). A more durable strain-limiting material is therefore required. Some preliminary work is performed on the fabrication of a PneuNet design. It is presented in Appendix A.

2.3.1.2 Fiber-Reinforced Actuators

Similar in bending motion to the PneuNet, Fiber-Reinforced (FR) actuators use fiber strands or meshes to radially constrain the actuator geometry (Figure 2.5). The actuator is typically fabricated by first embedding a strain-limiting layer into the flat surface of a half-cylinder elastomer tube. Fiber strands are then wrapped around the structure. The reinforcing fibers prevent radial expansion, limiting the actuator to axial deformation. With

the strain-limiting layer preventing the flat surface of the actuator from stretching, the geometry will perform a bending motion. The fibrous material can include, but is not limited to, Kevlar thread, nylon, and string [33], [63], [64]. Contact points between the soft actuator membrane and the reinforcing fibers create sources of highly localized strains and abrasion, which are both known causes of actuator failure by rupture [33]. To reduce these strains, a sleeve cover can be placed over the fiber strands.

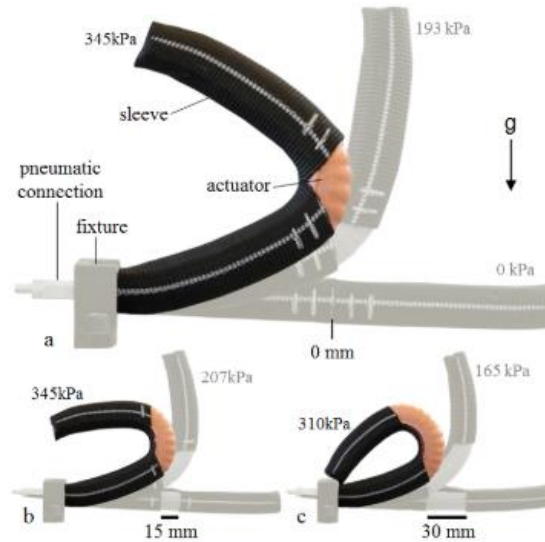


Figure 2.5 Fiber-Reinforced actuators at different sleeve spacing configurations (Galloway et al. [63] © 2013 IEEE, included with permission).

Research by Galloway et al. [63] investigates the impact of sleeve placement over the actuator's length. The work also verifies the impact of different materials, using DragonSkin 10 (Shore hardness 10A) and Elastosil M4601 (Shore hardness 28A) for a comparative study. A third case is created by fabricating another FR actuator out of Elastosil with sheets of fiberglass laminate bonded to the flat surface of the structure and held beneath the sleeve cover. Three sleeve spacing configurations are tested. They are 0 mm (no spacing), 15 mm, and 30 mm between each sleeved section. The study shows that increasing the spacing of the sleeve portions in turn increases the actuator's bending deflection at a given pressure. Adding the more rigid laminate sheets causes the flattest response to a given pressure for the two lesser sleeve spacing configurations. The 30 mm

configuration exhibits the lowest radius of curvature for a given pressure. This suggests that the rigid laminate sheets can localize actuation to the sleeve spacing, an important concept for the purposes of this research thesis as it shows that incorporating passive rigid elements into a soft actuator assembly can improve control over the system [63].

Comparing the two elastomers used shows that the softer material (DragonSkin 10) exhibited the highest sensitivity to a given pressure with respect to bending deflection [63]. In all cases and configurations, the softer elastomer can achieve smaller radii of curvature. However, the softer material is also more susceptible to instabilities at high pressures (over 400 kPa) and becomes highly prone to failure by rupture. Like the work by Mosadegh et al. on the PneuNet [4], this suggests that while a softer material structure may initially produce forces comparable to a stiffer elastomer, the stiffer material can support higher pressures. Thus, it can also produce larger forces. In summary, the described research presents trade-offs in actuator performance between sensitivity of deformation to air pressure, output force, and radius of curvature for a FR actuator.

Galloway et al.'s soft FR actuator also uses 3D printed polymer moulds for casting the elastomer mixtures in the geometries desired (Figure 2.6). The interior of the actuator is defined by the insertion of a half-round steel rod within the mould assembly. Several elastomer layers are casted and removed from the mould assembly, with modifications and additions made to the actuator between casting sessions. Once complete, the steel rod is removed, and the actuator is closed off on both sides with rigid caps. The input cap of the actuator includes a pneumatic fitting. Frequently removing the soft structure from the mould assembly increases the likelihood of damaging the actuator. Multiple modifications and additions also increase the possibility of non-identical actuators, resulting in varied performance. This is further compounded by the need to realign the actuator structure and steel rod within the mould assembly between each fabrication step.

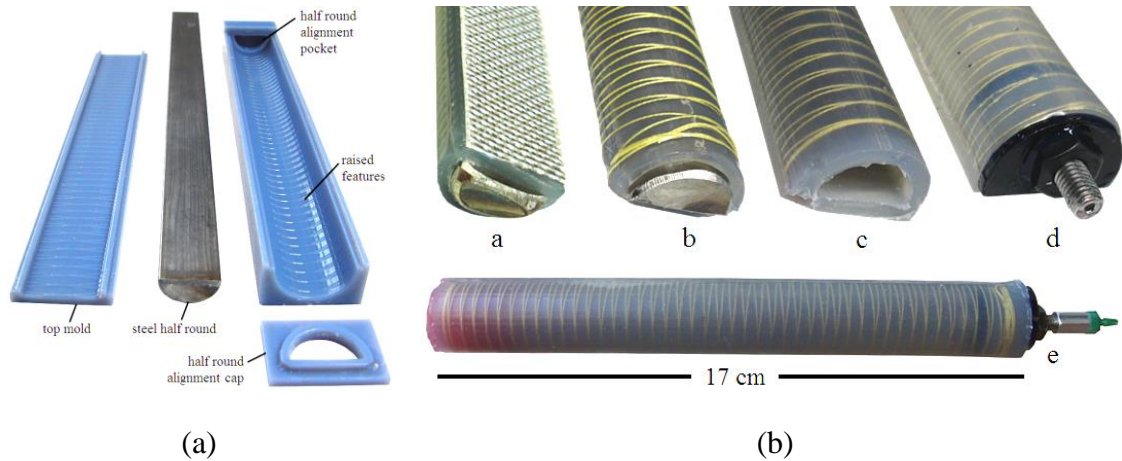


Figure 2.6 FR actuator fabrication (Galloway). (a) Mould components; (b) Multi-step fabrication process (Galloway et al. [63] © 2013 IEEE, included with permission).

Another study by Miron et al. [33] in Sherbrooke, QC, presents a similar design. Though the design is primarily tested as a gripper system (and thus will be discussed in Section 2.3.2), the proposed design presents an emphasis on three fatigue principles for FR actuators. These are:

1. Reduction in local stresses and strains.
2. Reduction in surface damage from abrasion and fiber-on-membrane cutting.
3. Operating below a material's fatigue limit; the strain under which the fatigue life tends towards infinity.

Fabrication for the FR actuator by Miron et al. [33] is accelerated by using a pre-made, open-ended tube of silicone elastomer known to have a fatigue limit of over 50%. A woven elastic band sewn in an inelastic nylon-fabric strip forms the FR sleeve that produces the bending motion. This sleeve is then positioned over the elastomer tube. The ends of the tube are once again capped (Figure 2.7). Using a pre-made elastomer structure significantly limits the shape and size of any actuator designed in this research thesis.

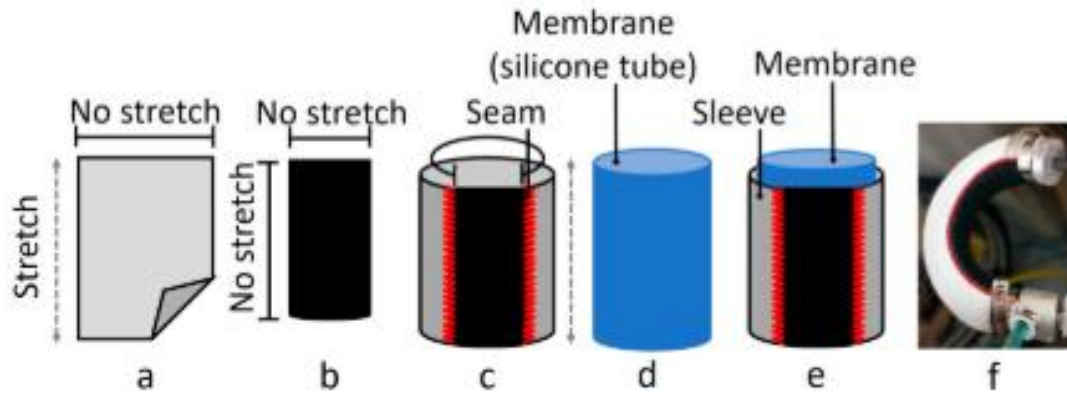


Figure 2.7 FR actuator fabrication (Miron) (Miron et al. [33] © 2018 CC-BY, included with permission).

2.3.1.3 *Pneumatic Artificial Muscles*

One of the earliest and simplest air-driven soft actuators is the Pneumatic Artificial Muscle (PAM), shown in Figure 2.8, where an internal elastomeric membrane (typically a cylindrical bladder) is surrounded by a woven braided shell [65], [66]. The behaviour of a PAM is dependent on its fabrication. Fitting the woven shell evenly along the muscle length (or making it slightly shorter) will cause it to contract when pressurized (contractor muscle). Using a shell that is slightly longer than the muscle will cause the actuator to extend under pressure (extensor muscle). The length of the shell is quantified by the pitch, braid, or weave angle. A contractor muscle will have a maximum braid angle of 54.7° at full contraction [65]. Extensor muscles will have the same braid angle when at rest. No single PAM can achieve both types of motion. Contractor muscles are significantly more established in research [66]. A common variant of the contracting PAM is the McKibben actuator. When pressure is applied at a constant value within the inner cavity, a contraction force is produced. This decreases with the contraction ratio, which is defined as the ratio between the muscle's reduction and its initial length [67]. Like all PAMs, the McKibben actuator generates a linear and unidirectional axial force, resulting in linear motion that transfers forces to an attached load [65].

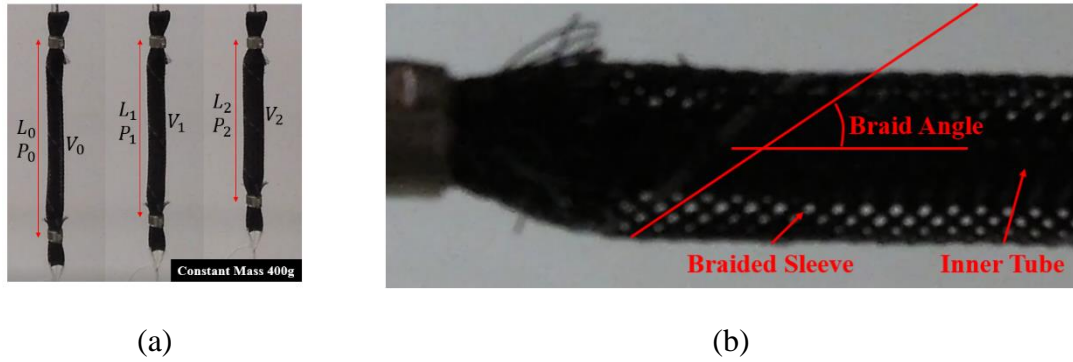
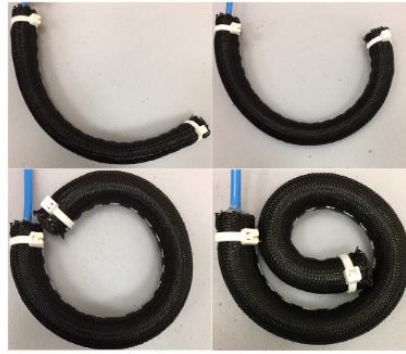


Figure 2.8 Pneumatic artificial muscles. (a) PAM contraction for increasing pressure with constant mass; (b) Enhanced view of PAM braided sleeve. Figures created at Western University.

Research by Al-Fahaam et al [66] starts with a McKibben PAM, and reconfigures it to become an extensor muscle by replacing the fitted woven shell with one significantly longer than the muscle (i.e., the shell now has a braid angle greater than 54.7° when the actuator is at rest). This modifies the McKibben actuator into an extensor muscle. The structure was then reinforced along one side with a strain-limiting layer to keep it at a fixed length. When pressurized, the new design is unable to extend in length and therefore performs a bending motion. This new variant of the PAM is proposed as an extensor bending pneumatic artificial muscle (EBPAM). An example of the EBPAM is shown in Figure 2.9.



(a)



(b)

Figure 2.9 McKibben EBPAM. (a) Modified extensor McKibben actuator; (b) Extensor McKibben actuator further modified to bend (Al-Fahaam et al. [66], © 2018 Elsevier, included with permission).

A summary of the performance of each type of described actuator, including operating pressures and applicable forces, is available in Table 2.2. Note that the percentages listed along the force values for the McKibben PAM are based on the muscle's level of contraction.

Table 2.2 Performance summary of actuator designs.

Actuator	Material	Mass	Operating Pressure	Actuation Speed	Applied Force	Comments	Reference
PneuNet	EcoFlex 00-30 (extensible); PDMS (inextensible); Paper (strain-limiting layer)	-	72 kPa	130 milliseconds	1.4 N	-	[4]
FR Actuator	DragonSkin 10	-	172 kPa	-	2.75 N	30 mm sleeve spacing	[63]
	Elastosil M4601	-	414 kPa	-	7.12 N	30 mm sleeve spacing	
McKibben PAM	-	50 g	300 kPa	-	650 N (rest); 300N (15%); 0 N (30%)	150 mm rest length, 14 mm diameter	[65]
	-	32 g	300 kPa	-	220 N (rest); 100 N (10%); 0 N (20%)	150 mm rest length	
McKibben EBPAM	-	-	500 kPa	-	42 N	bending actuator	[66]

Soft robotic designs exist for end-effectors or manipulators that implement PAM actuators in object manipulation applications [68], [69]. These systems typically emulate the complex biological behaviour of elephant trunks or cephalopod tentacles, the nature of which is not suited for the purposes of this research thesis.

2.3.2 Review of Soft Pneumatic Grippers

A six-fingered PneuNet gripper was originally developed by the Whitesides group [6]. Though little numerical data was found for this proof-of-concept design, the gripper was able to pick up a raw egg without breaking the shell. It was also capable of handling a sedated mouse without causing it any harm (Figure 2.10). The soft structure of the PneuNet

gripper distributes the target's load over the gripper's entire surface instead of a few force points.

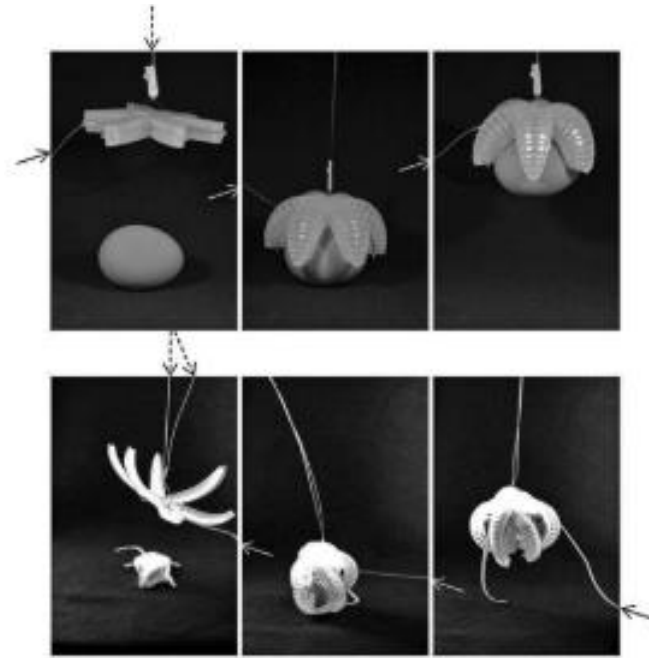


Figure 2.10 Early Whitesides PneuNet grippers. Grasping an egg (top) and a sedated mouse (bottom) (Whitesides et al. [6], © 2011 WILEY, included with permission).

Another PneuNet gripper design is presented by Galloway et al. [70]. In this case, the contact surfaces of the gripper's four fingers are modified to fit a block of memory foam for additional soft contact. Payload tests for this gripper design are performed for both horizontal and vertical configurations, and a case study is performed for collecting delicate reef samples at depths of up to 170 m (Figure 2.11) [70].

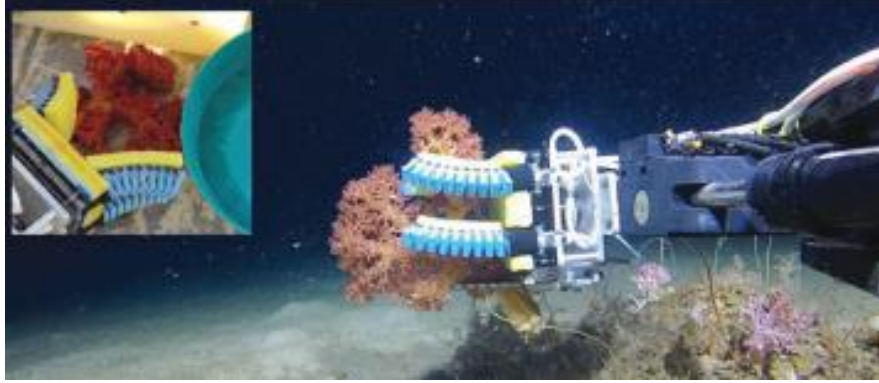


Figure 2.11 PneuNet Gripper for delicate ocean reef sampling (Galloway et al. [70], © 2016 Mary Ann Liebert, Inc., included with permission).

Research by Hao et al. [58] describes another four-fingered PneuNet gripper design (Figure 2.12). The core of their work focuses on investigating the performance of tunable effective finger lengths. A nylon strand is selectively placed to mechanically control the length of the PneuNet actuators that inflates. The study concludes that there exists an optimal PneuNet length capable of providing the maximum pull-off force for specific gripper shapes and sizes. That is, longer effective lengths are best-suited for larger objects whereas shorter lengths were better for smaller structures. For this work, the PneuNet fingers are made entirely out of DragonSkin 30 silicone elastomer. Payload tests are performed with a variety of different shapes. The work suggests that the gripper's payload capabilities is partially dependent on the effects of friction and geometrical overlapping or interlocking of the gripper fingers. When gripping objects by their vertical sides, like in the case of larger objects such as a rectangular prism, friction forces acting tangentially to the grasped surface are the primary means of grasping the object. As such, recorded pull-off forces are significantly smaller compared to smaller objects. However, the gripper fingers can enclose and wrap around objects like spheres and smaller cubic structures. In this case, the fingers overlap or interlock geometrically around the object. This effect becomes the dominant principle behind the gripper's grasping capabilities, with friction forces having a less significant role. The work also found that when the gripper holds flatter, more cubic-shaped objects, the maximum pull-off force observed is approximately double that of grasping a spherical structure [58].

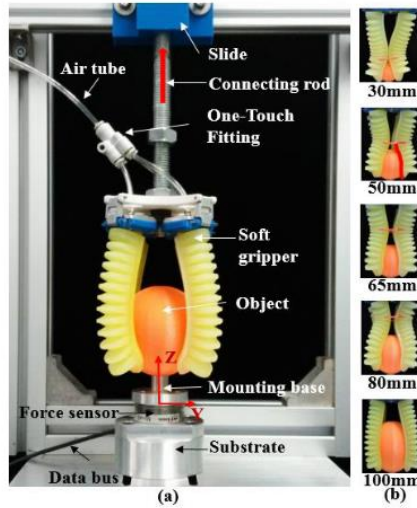


Figure 2.12 Universal PneuNet gripper testing tunable actuator lengths (Hao et al. [58], © 2016 IEEE, included with permission).

Soft Robotics Inc., a company based in Cambridge, MA, produces and sells basic PneuNet grippers for industrial pick-and-place operations. Though information on their design is proprietary, application videos on their website show an alleged maximum payload of 4.5 kg [33].

2.3.2.1 Fiber-Reinforced Grippers

The Fiber-Reinforced actuators previously described by Galloway et al. [63] were also tested in a two-fingered gripper assembly. The gripper was tested with three actuator configuration cases: a sleeveless actuator, an actuator with 0 mm sleeve spacing, and another with 0 mm sleeve spacing and the laminate sheets beneath the sleeve cover. All three cases were performed with Elastosil M4601 as the primary actuator material [63]. During payload tests (Figure 2.13), the sleeveless configuration would bow at the sides, leaving considerable compliance for the actuators to deform further as the applied payload increased. The 0 mm sleeve spacing case exhibited reduced bowing, demonstrating improved conformability to the payload. The case with laminate sheets exhibited the best conformability to the payload, in turn resulting in a higher maximum payload capacity [63].

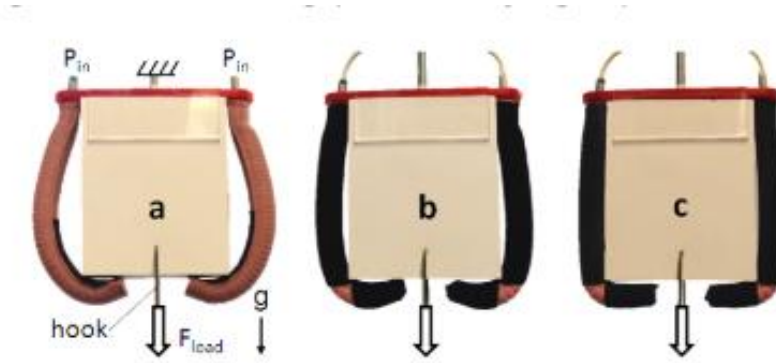


Figure 2.13 Maximum payload test of Fiber Reinforced grippers with different actuator sleeve spacing configurations (Galloway et al. [63], © 2013 IEEE, included with permission).

Using a similar FR actuator design, Miron et al. [33] developed two gripper assemblies: one small and one large. Both grippers are assembled by fixing the actuators to a 3D printed polymer plate. By configuring the actuators around the plate, the gripper can be organized as “fingers” on a “palm” [33]. The smaller gripper has three actuators in a 2-1 facing configuration, while the larger gripper can hold four actuators in a 2-2 offset configuration. However, the study performed its experiments with a large gripper having a 2-1 configuration to allow comparison between the two designs (Figure 2.14).

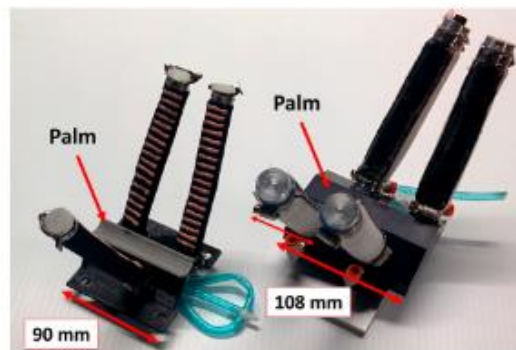


Figure 2.14 Small (left) and large (right) variants of the Fiber Reinforced gripper developed at Sherbrooke University (Miron et al. [33], © 2018 CC-BY, included with permission).

CHAPTER 2. BACKGROUND AND LITERATURE REVIEW

A summary of the performance of several gripper designs, including operating pressures and applicable forces and payloads, is available in Table 2.3.

Table 2.3 Performance summary of gripper designs.

Gripper	Material	Mass	Operating Pressure	Contact Force	Contact Pressure	Slip Tests	Payload	Comments	Reference
PneuNet Gripper	Elastosil M4601 core; Smooth-Sil 950 exterior	-	68.9 kPa	-	2 kPa	-	2 kg	-	[70]
	With foam insert			-	7 kPa	-		-	
		-	124 kPa	-	-	16.6 N	-	Vertical	
						5.6 N		Horizontal	
	DragonSkin 30		50 kPa	-	-	13.5 N	-	Maximum value for all trials	[58]
	-	-	-	-	-	-	4.5 kg	SoftRobotics Inc.	[33]
FR Actuator Gripper	Elastosil M4601	90 g	345 kPa	-	-	-	3.45 kg	No sleeve cover	[63]
							4.68 kg	0 mm sleeve spacing	
							6.1 kg	0 mm sleeve spacing; FR Laminate sheets	
	-	112.6 g	275 kPa	20 N	-	-	52 N	Small	[33]
	-	594 g		28 N	-	-	200 N	Large	

2.4 Chapter Summary

This chapter provided the background information in context with this research thesis. A detailed summary of hyperelastic theory and PDMS has been presented. The unique capabilities and advantages of pneumatically-driven soft robotic actuators and grippers have led to their continued development in recent history. However, methods to characterize their performance and behaviour are limited to primarily empirical testing and lengthy iterative design processes.

Chapter 3

Design Methodology and Fabrication

This chapter outlines the design and fabrication of a pneumatically-driven soft robotic gripper. The geometric design for the soft actuator and gripper is proposed. Fabrication of the gripper actuators is outlined in detail, involving a multi-step moulding process. The role and functionality of the computational software, COMSOL Multiphysics, is presented.

3.1 Geometric Design of Elastomeric Actuators

Soft pneumatic actuators reviewed in Section 2.3.1 all included long compliant structures that underwent a bending motion when pressurized. The resulting gripper systems were therefore larger assemblies, taking up more volume in the manipulator's workspace. Larger soft actuators, especially ones made of ultra-soft elastomers, are also more susceptible to gravity and other external sources of disturbance that may impact their performance. To verify this, preliminary work was performed on a simple ultra-soft PneuNet gripper. All associated work can be found in Appendix A, but it is shown that the ultra-soft structure is not well-suited for the intended application. In addition, Section 2.2.2 points out that PDMS can only withstand maximum strains of 150% [6]. Therefore, a smaller gripper geometry was considered.

A soft pneumatic gripper comprised of three compact PDMS actuators (Figure 3.1a) is developed for grasping irregular shaped organic objects such as mushroom tops, strawberries, and small citrus fruits during automated harvesting [10]. Each constituent actuator has a curved geometry (Figure 3.1b) and operates similarly to a single chamber PneuNet [2] with only one deformable concave wall that expands toward the center of the gripper assembly during pressurization (Figure 3.1c). Therefore, unlike bending actuator-based grippers that use a combination of interlocking actuator fingers and friction forces to grasp a target, the proposed design holds the target through friction forces alone. The modular single-DOF actuator was designed for functional simplicity, ease of fabrication and assembly, reliability, and repeatable performance. In addition, the design enabled a realistic model of the stress behaviour to be simulated using COMSOL Multiphysics software. The simulations were necessary to predict the impact of key design parameters on the gripper's performance during air inflation.

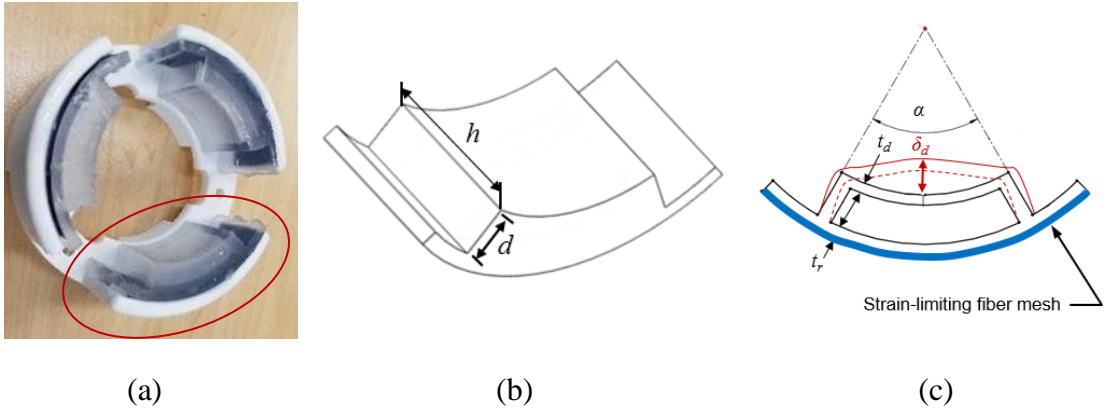


Figure 3.1 (a) Bottom view of a gripper comprised of three soft pneumatic actuators. (b) Outside geometry of the actuator's pneumatic chamber. (c) Internal structure of the chamber walls, location of the strain-limiting fiber mesh (blue) and the impact of inflation (δ_d) on the active deformable wall (red). Note that the deformation is for visualization purposes only.

The dimensional parameters for the actuator correspond to the inflatable chamber height (h) and depth (d), the angle of the actuator's arc (α), the thickness of the outer wall attached to the rigid housing unit (t_r), and the thickness of the expandable deformable

inner wall (t_d). The majority of chamber expansion will occur along the inner concave wall and, therefore, it is labeled the actuator's primary active deformable wall. When inflated with pressurized air the freely moving expandable primary wall produces a center displacement (δ_d) with a predictable contact pressure (P_c). The displacement and contact pressure are dependent upon both the actuator's chamber geometry and the applied air pressure input (P_a). The geometric parameters used to simulate and experimentally assess the performance of the proposed hyperelastic actuator are given in Table 3.1. Furthermore, the impact of these parameters will be evaluated over a range of low applied air pressures (P_a).

Table 3.1 Key design parameters used to analyze soft pneumatic actuators during operation.

Parameter	Range of Values
Wall thickness, t_d	1.5 mm, 2 mm, 2.5 mm
Actuator chamber height, h	10 - 30 mm; increments of 2 mm
Actuator arc angle, α	45° – 90°; increments of 5°
Applied air pressure, P_a	6.89Pa – 68.9 kPa (1psi - 10 psi)

3.2 Actuator Fabrication

Section 3.3 introduces the model setup in COMSOL Multiphysics for simulations that are described in Chapter 4. However, to keep the design and fabrication of the actuators together, Section 3.2 first describes the moulding process used to create the actuator prototypes. These actuators are validated through experiments presented in Chapter 5. The process described in Section 3.2 is general to all actuator prototypes fabricated. Note that the actuators are fabricated for testing after the simulations are completed.

Fabrication methods of various actuator designs were described in Section 2.3.1, including flaws prevalent in each methodology. Specific design decisions were made to circumvent these limitations. First, the paper strain-limiting strip from the PneuNet's fabrication has been replaced with durable synthetic fiber mesh. A complicated fabrication process using metal rods and requiring frequent removal of the partially fabricated actuator

has been bypassed by using only 3D printed ABS polymers for the mould components and by embedding the strain-limiting layer at the end of the whole process. Elastomers are acquired as pre-polymer mixtures to be prepared and poured into the moulds, avoiding the limitations imposed by purchasing pre-made silicone structures. This fabrication methodology provides complete control over every aspect of the soft PDMS actuator including geometry and material properties. The hyperelastic actuators are fabricated using a multistep soft lithography moulding process. The method requires two circular mould bases (Mould 1 and Mould 2) and a detachable outer wall as shown in Figure 3.2, where each reusable mould assembly can produce up to three compact pneumatic actuators at a time. Mould 1 is used to form the majority of the part geometry with a single open exposed surface while Mould 2 creates the final surface used to close the pneumatic chamber for the actuators. The moulds are designed for proper alignment during assembly and a combination of partial curing and adhesive bonding for assembling the discrete PDMS components. Before coming into contact with any PDMS pre-polymer, every surface of the mould assemblies is coated with a layer of surfactant. A mixture of soft detergent and water is used to prevent the pre-polymer from adhering to the 3D printed mould components.

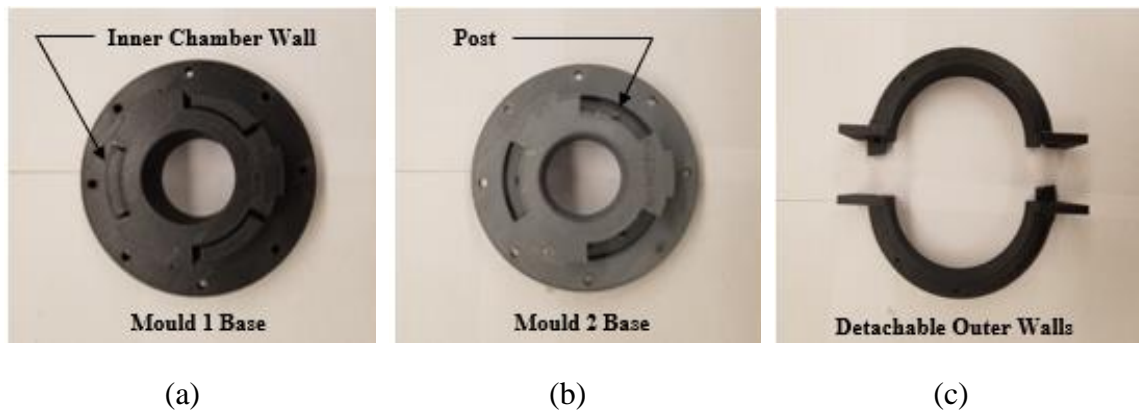


Figure 3.2 Top view of the (a) base for Mould 1; (b) base for Mould 2; and (c) detachable outer walls.

The key steps in fabricating the individual PDMS actuators (Figure 3.3) are now summarized. Mould 1 is first assembled by attaching the outer mould wall to the base (3.3a)

and ensuring that there are no leaks along the joins. Mixed PDMS pre-polymer is then slowly poured into each of the actuator cavities (3.3b). Once filled, the assembly is placed in a vacuum chamber and fully degassed until no bubbles remain in the PDMS. After degassing the PDMS, the entire assembly is left to cure at ambient temperature for 48 hours. Upon completion of curing, the outer walls attached to the Mould 1 base are removed and the cured PDMS part is carefully extracted (3.3c). The bottom section of the Mould 2 base is then partly filled with PDMS (3.3d), degassed, and partially cured for 24 hours. Typically, the thickness of the layer would be half the height of the post located at the center of the Mould 2 base. The post forms the through-hole on the bottom PDMS layer which becomes the air inlet for the assembled actuator. The process of partially curing allows the PDMS part to reach a solid state but remain bondable to another PDMS structure. To ensure a strong bond between the discrete moulded parts, the remainder of the bottom section (slightly below the height of the central post) is filled with PDMS pre-polymer and further degassed to eliminate bubbles in the polymer. The fully cured PDMS part previously extracted from Mould 1 is then carefully aligned and placed over the uncured PDMS layer (3.3e). Light pressure is applied to the part in order to form a tight seal for the bonding process. To ensure that the assembly remains in place during the curing process, the outer walls are attached to the base of Mould 2. The completed Mould 2 assembly is then left to cure at ambient temperature for 48 hours, after which it is taken apart and the finished PDMS geometry is removed (3.3f). Finally, a strip of synthetic fiber mesh is adhered to the convex surface of the actuator geometry with a thin coating of more pre-polymer. This forms the strain-limiting inextensible layer of the actuator. Engineering drawings for these mould components are available in Appendix D.

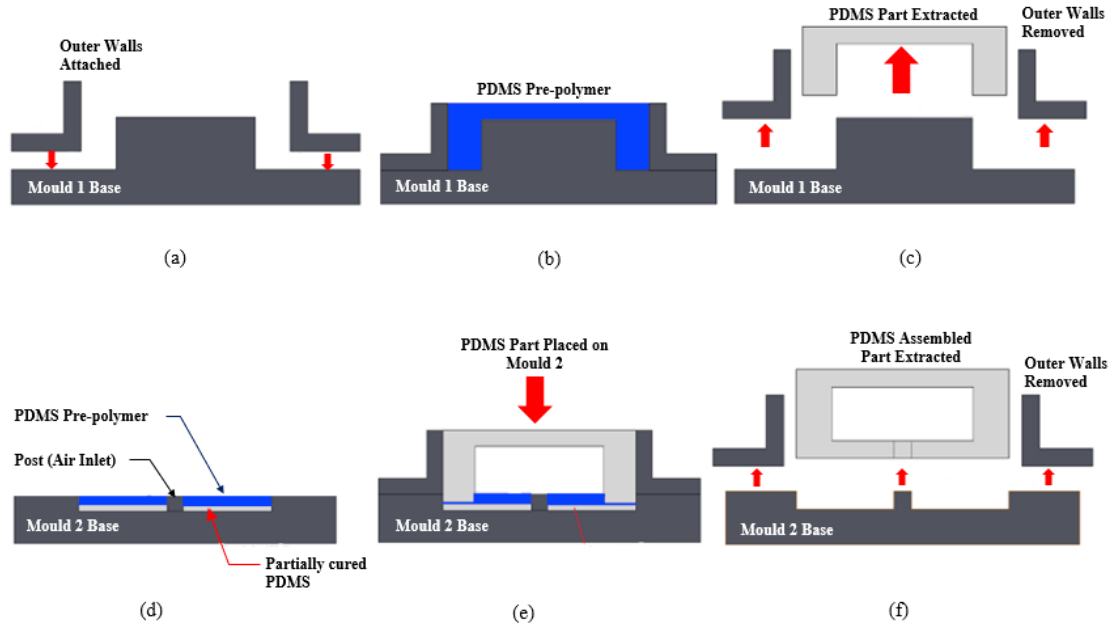
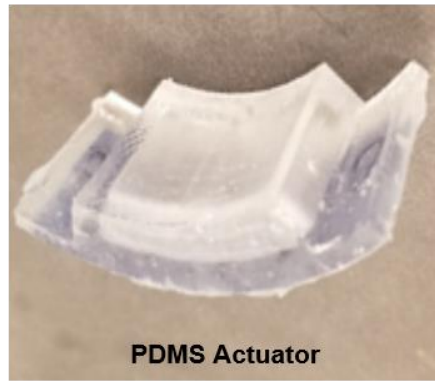


Figure 3.3 Key steps in the fabrication actuator fabrication process. (a) Assembly of outer walls on the base for Mould 1; (b) Pour PDMS pre-polymer in mould cavity; (c) Extract PDMS part from disassembled mould; (d) Fill bottom of base cavity of Mould 2 with partially cured PDMS and then uncured pre-polymer; (e) Align and secure PDMS part on partially cured layer; and (f) disassemble mould to remove completed actuator with a single air inlet through-hole to chamber.

The PDMS pre-polymer is first degassed as soon as it is mixed until no air bubbles are observable. It is then slowly poured into the open moulds in small increments at a time. Once the moulds are filled, they are placed into the vacuum chamber and degassed again. Every step that involves the agitation of the PDMS pre-polymer is followed by another degassing session. This is to ensure that there are no bubbles in the mixture.

In some instances, bubbles that rose to the surface remained and would not dissipate. When this occurred, a heat gun was quickly passed over the surface at its lowest setting. The jet of air would remove any bubbles at the mixture's surface and was applied quickly enough that the pre-polymer would not be heated by any significant amount.

Once fabricated, three identical actuators (Figure 3.4a) are inserted into the 3D printed housing unit to form the circular ring-like gripper (3.4c and 3.4d). The rigid ring has inlets that allow polyurethane tubing to connect to the actuators. A coupling extension connects the gripper ring to a manipulator arm (3.4b). It also adds clearance between the arm and the gripper ring. All rigid structural components of the gripper housing unit and robot attachment are made of ABS polymer. The ring structure can hold the actuators of varying chamber heights and arc angles, but all experiments focus on the deformable inner concave wall thicknesses. The ABS ring weighs approximately 34 g, and each actuator weighs approximately 14 g. In total, each gripper weighs approximately 76 g.



(a)



(b)



(c)



(d)

Figure 3.4 (a) Single moulded PDMS actuator; (b) Robotic end-effector with the elastomeric actuators inserted into the gripper assembly (coloured white); Top view of gripper ring in (c) deflated state and (d) moderate inflated state. For the sake of picture clarity, the actuators shown in (c) and (d) of this figure were fabricated out of Ecoflex 00-30. Ecoflex is white while PDMS is nearly transparent.

3.3 Role and Functionality of COMSOL Multiphysics Software

COMSOL Multiphysics is an extensive, multi-functional finite element analysis (FEA) solver and simulation software package. Starting as a base program, additional software modules can be added to solve specific multiphysics problems. For this research, the Structural Mechanics Module was used with the Nonlinear Structural Materials Module for the analysis of hyperelastic geometries under static loads. The Material Library Module is used to implement material properties related to PDMS (10:1 mixing ratio, cured at 25°C). The CAD Import Module and LiveLink for SolidWorks add-on are used to synchronize the generated SolidWorks models with COMSOL simulations.

COMSOL Multiphysics provides a reliable and efficient method of analysis. Based on the simulations, the deformation of a particular actuator geometry can be calculated and used to quantify performance. This is advantageous to the process of soft robotic design, as it permits numeric comparison of various design geometries, identification of sources of strain, and a benchmark for assessing acceptability of performance.

Performing simulations introduces the benefit of being able to assess the impact of numerous geometrical parameters on the actuator's performance at a significantly accelerated rate relative to fabricating physical iterations. By selecting a single geometrical parameter at a time, COMSOL can solve for a swept range of parameter values and provide quantitative results for each. These simulations can be performed in time-independent (stationary) and time-dependent conditions. In addition, COMSOL includes a detailed data-solving system with which a single simulation can provide a multitude of different results including displacements, stresses, strains, and contact forces generated by pressure loads. These results can be viewed in one, two, or three dimensions.

3.3.1 Defining PDMS Material Properties for Finite Element Modelling

COMSOL's Material Library Module includes data for PDMS, shown in Figure 3.5. Initial bulk and shear moduli for PDMS are listed as 3.333×10^7 Pa and 6.67×10^5 Pa, respectively [25].

»	Property	Variable	Value	Unit	Property group
✓	Density	rho	970[kg/m...	kg/m ³	Basic
	Coefficient of thermal expansion	alpha_is...	9e-4[1/K]	1/K	Basic
	Heat capacity at constant pressure	Cp	1460[J/(kg...	J/(kg·K)	Basic
	Relative permittivity	epsilon_r...	2.75	1	Basic
	Thermal conductivity	k_iso ; ki...	0.16[W/(m...	W/(m·K)	Basic
	Young's modulus	E	750[kPa]	Pa	Young's modulus and Poisson's...
	Poisson's ratio	nu	0.49	1	Young's modulus and Poisson's...

Figure 3.5 Material data for PDMS from COMSOL Multiphysics' Material Library Module.

To satisfy both the shear moduli relation and approximation described in Section 2.1.1, $\mu_1 = \frac{7}{16}\mu = 2.918 \times 10^5$ and $\mu_2 = \frac{1}{16}\mu = 0.417 \times 10^5$. Separate tests were performed on standard tensile specimens to assess the mechanical properties of the PDMS material used in the prototype development. In general, the measured results were in agreement with the trends reported by Johnston et al. [41] with minor deviations arising from slight differences in the ambient curing temperature.

When a rubber-like material is subjected to a very high hydrostatic pressure, the observed change in volume is very small. Changing the shape of a rubber-like material is much easier than changing its volume. Thus, it is common practice in computational modelling to consider them as incompressible [27], introducing the constraint condition of the elastic volume ratio $J = 1$, as described in Section 2.1.1. With this assumption, the Poisson's ratio (ν) of the simulated PDMS is 0.5. However, this results in computational errors due to the use of the Poisson's ratio in the denominator of equations of properties such as, for example, the bulk moduli

$$K_1 = \frac{E}{3(1 - 2\nu)} \quad (3.1)$$

To avoid division by zero, the Poisson's ratio is set to 0.49. However, this introduces the possibility of displacement-based finite element analysis producing skewed results due to volumetric locking. Locking affects the model by creating an overly stiff response. Locking effects can be diminished by ensuring that the "Nearly Incompressible Material"

option is selected in the COMSOL hyperelasticity toolbar. In this case, the compressibility of the material is small enough to be considered negligible.

3.3.2 Model Implementation in COMSOL Multiphysics 5.3

A model for a single actuator geometry is imported from SolidWorks. To replicate the strain-limiting layer and 3D printed structure backing on the physical actuator, a fixed constraint is applied to the model's rear convex wall, highlighted in yellow in Figure 3.6a. A boundary load is applied to the chamber's primary deforming wall, highlighted in blue in Figure 3.6b.

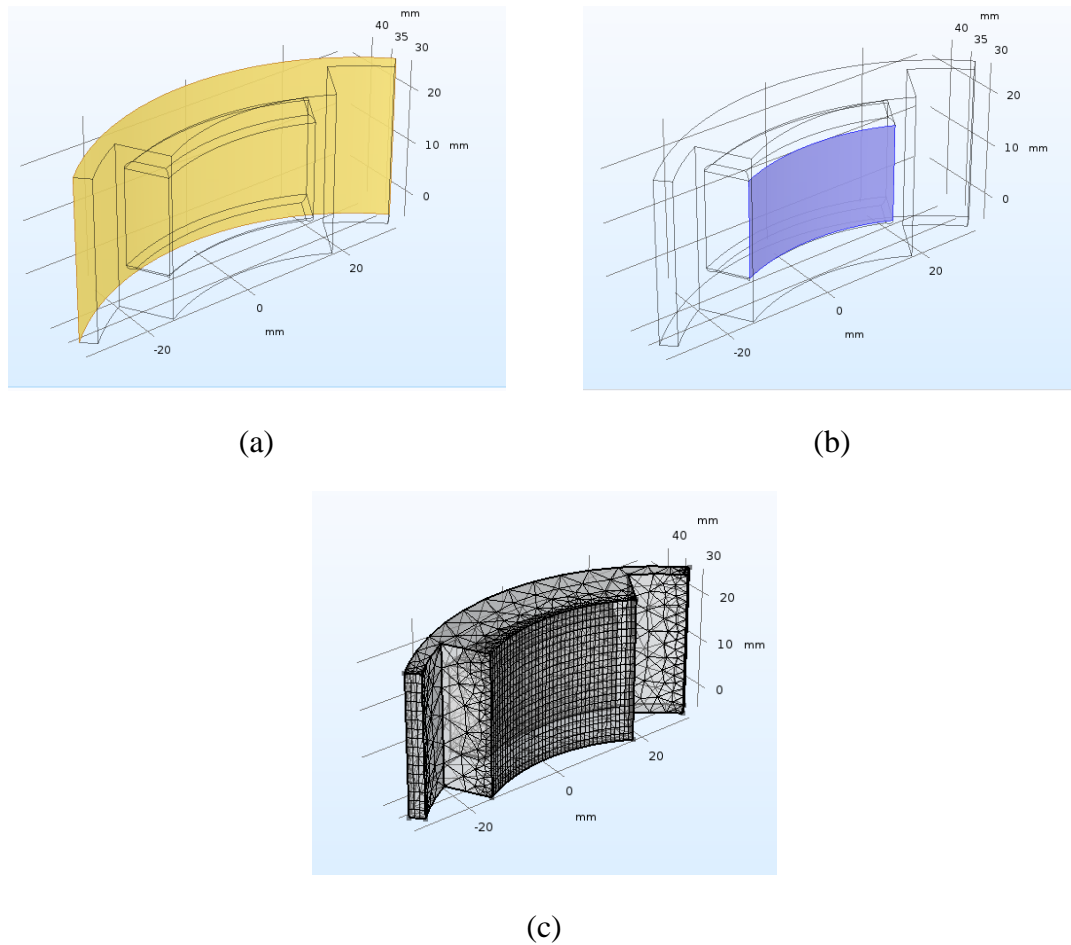


Figure 3.6 Wireframe of single actuator. (a) Fixed constraint highlighted in yellow; (b) Boundary load to concave deformable wall highlighted in blue; (c) Finite element mesh generated over model geometry and locally refined at concave deformable wall surface.

Data is solved for at a point located in the center of the concave primary active deformable wall. The goal of the model is to solve for the actuator's wall displacement for input pressures and geometry (e.g., t_d , h , α). Total displacement at the point (δ_d) is determined by the (x, y, z) components of the displacement field, u , v , and w .

$$\delta_d = \sqrt{u^2 + v^2 + w^2} \quad (3.2)$$

3.3.3 Mesh Generation for Finite Element Modelling

As mentioned, COMSOL Multiphysics primarily uses the finite element method (FEM) to solve for any given study. Thus, creating a mesh is necessary, and COMSOL provides a detailed system to create meshes both automatically and manually. Mesh settings determine the resolution of the mesh created to discretize the model by dividing the model into small elements of geometrically simple shapes [71]. A set of partial differential equations (PDEs) is used in each of these elements to approximate the structural displacement field. That is, how much the model deforms in the (x, y, z) directions. Analysis of the three coordinate directions means that each element has its own volume.

Ideally, COMSOL would quickly solve for an incredibly fine mesh, providing accurate results in but a few seconds of computations. That is unfortunately not the case, as meshes made too fine may never converge to a solution. It is again important to note that the accuracy of a solution is directly related to the size of the created mesh (Figure 3.6c). All computations are limited by finite computational resources and time; thus, it is unreasonable to try to solve for the exact solution with a mesh size nearing or equaling zero. Computations must instead rely on an approximation of the real solution. It is therefore critical that the difference or error between the exact solution and its computed approximation is minimized. This is known as mesh refinement or independence. This was ensured in this research thesis by performing the same simulation over a range of finite meshes, from very coarse to very fine. Once the computed data stopped being affected by the coarseness of the mesh, it was considered mesh-independent. In addition, it is important to consider the quality of the mesh itself. Mesh quality is an indication of the length-to-width ratio of the mesh elements. For thin membrane geometries, a general rule of thumb

is to keep a minimum mesh quality of at least 0.1. For this research, the minimum mesh quality solved for was 0.1734, and the average mesh quality was 0.599.

As shown in Figure 3.6c, mesh refinement is localized to the primary deformable wall. A custom mapped mesh generates quadrilateral mesh elements over the wall surface. This allows the quality of the mesh over the primary surface to be controlled. Quadrilateral elements are also mapped over the end surfaces of the actuator's extremities. The Free Tetrahedral operation is used over the remainder of the unmeshed geometry. This creates tetrahedral elements over the rest of the model, which can be refined through the selection of simple classifications (i.e., very fine, fine, normal, coarse, very coarse, etc.). COMSOL applies optimized solver types and settings based on the chosen domain, physics, and study type [71].

3.4 Chapter Summary

This chapter outlined the design of a compact single-DOF PDMS actuator in preparation for assembly into a soft pneumatic gripper. Key design parameters for analysis in nonlinear software are listed. The multi-step fabrication process was presented, and the 3D printed and interchangeable mould components can create up to three actuators at a time. Care is taken throughout the process to ensure that air bubbles are removed to the uncured PDMS, and each mould surface is prepared with a surfactant consisting of gentle detergent and water to prevent PDMS-surface adhesion during the curing process. The role and functionality of COMSOL Multiphysics was described. Material properties for PDMS used in simulation were shown, and the model setup was presented, including the steps taken to ensure study accuracy. This model can now be used to simulate deformation under load, and the impact of various parameter changes on that deformation.

Chapter 4

COMSOL Simulations and Results

This chapter outlines the simulations performed with the generated actuator model. The displacement of the primary concave wall is simulated under different parameter conditions. Contact pressures are calculated for use in the next chapter. Simulation data is additionally acquired to investigate the legitimacy of the results by relating studies performed back to the governing equations presented in Section 2.1. Finally, principal stretches and principal strains are presented, and their relationship is shown.

4.1 Wall Displacement for a Parameter Change

Each simulation starts with the same initial conditions as described in Section 3.3.2. That is, the PDMS structure is restricted so that the applied pressure (P_a) causes only the concave wall of the chamber to deform (Figure 4.1). For the first study, $P_a = 34.47$ kPa (5 psi) is applied to the expandable chamber wall with different wall thicknesses (i.e., $t_d = 1.5$ mm, 2 mm, 2.5 mm). The material behaviour in the hyperelastic PDMS structure is simulated using the Mooney-Rivlin model given by equation (2.10).

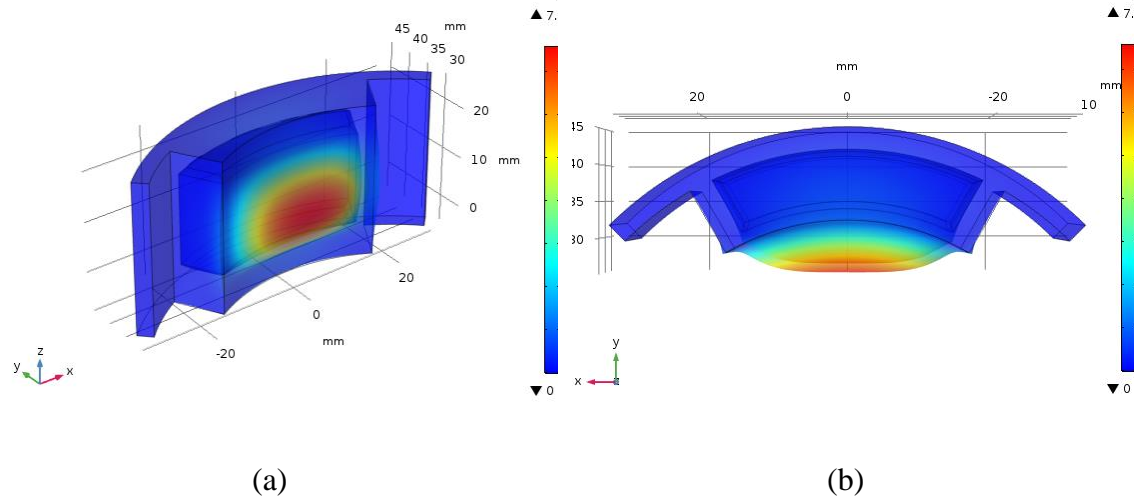


Figure 4.1 (a) Simulated model showing wall displacement due to expansion; (b) top view of simulated model of single actuator with expansion of the principle active wall.

A graph extracted from COMSOL Multiphysics is shown in Figure 4.2. The thinnest wall exhibits the greatest displacement of approximately $\delta_d = 5.50$ mm. In contrast, the thickest wall ($t_d = 2.5$ mm) has a displacement of only $\delta_d = 4.11$ mm. The result is realistic because the additional PDMS on the deformable wall provides greater resistance to the applied load.

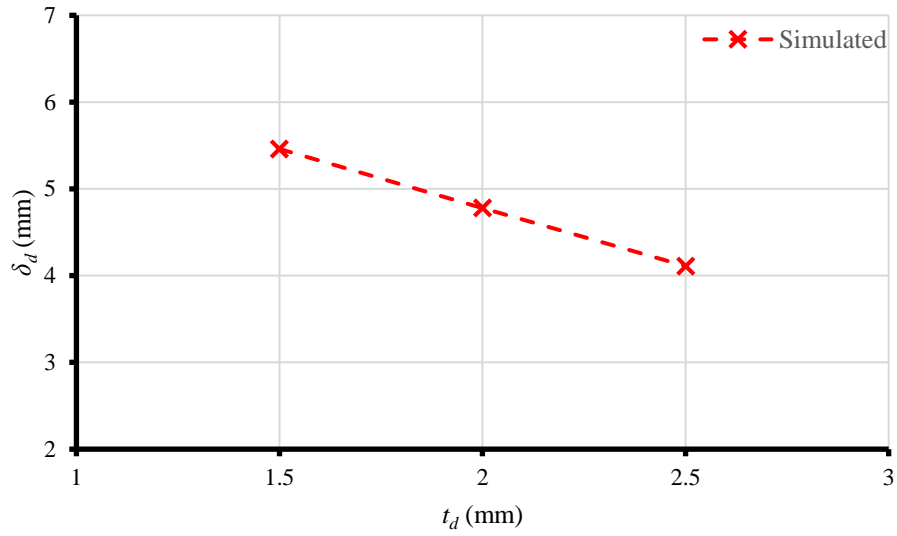


Figure 4.2 Simulated displacement (δ_d) values for three expandable wall thicknesses (t_d) at $P_a = 34.47$ kPa.

To examine the impact of applied pressure (P_a) on actuator wall deformation, a range of pressures of $P_a = 0 - 68.94$ kPa (0 – 10 psi) is applied to each wall thickness (Figure 4.3). Note that the rate at which the wall displaces does decrease at higher pressures because the PDMS is already stretched to near maximum.

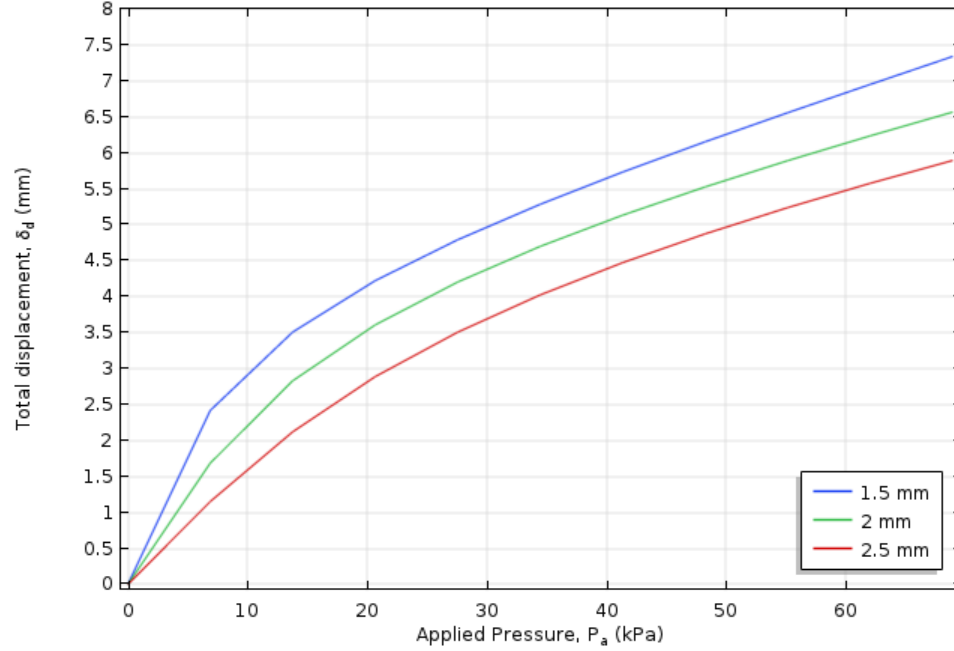


Figure 4.3 Simulated displacement values (δ_d) of different applied pressures (P_a , kPa).

A series of simulations were then performed to assess the impact of chamber height and actuator arc angle on the actuator's active wall displacement. In each case, the thickness of the active wall is kept at $t_d = 2$ mm, and $P_a = 6.89$ kPa of pressure is applied. The results show a near linear change in displacement for increased actuator height (Figure 4.4a) while increasing the arc angle (Figure 4.4b) only has a minimal impact on the actuator displacement. Note that as the α increases the active surface area of the actuator becomes bigger and modestly reduces the observed displacement when given the same internal pressure (P_a).

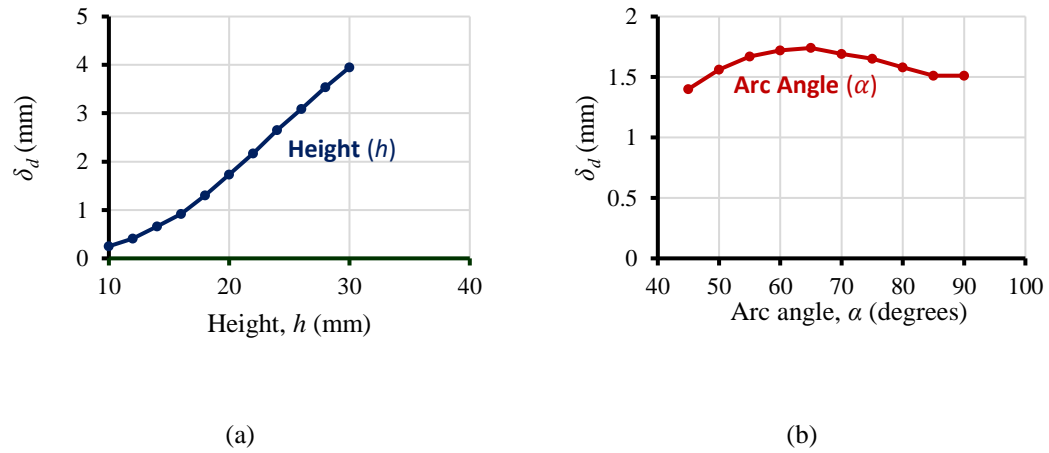
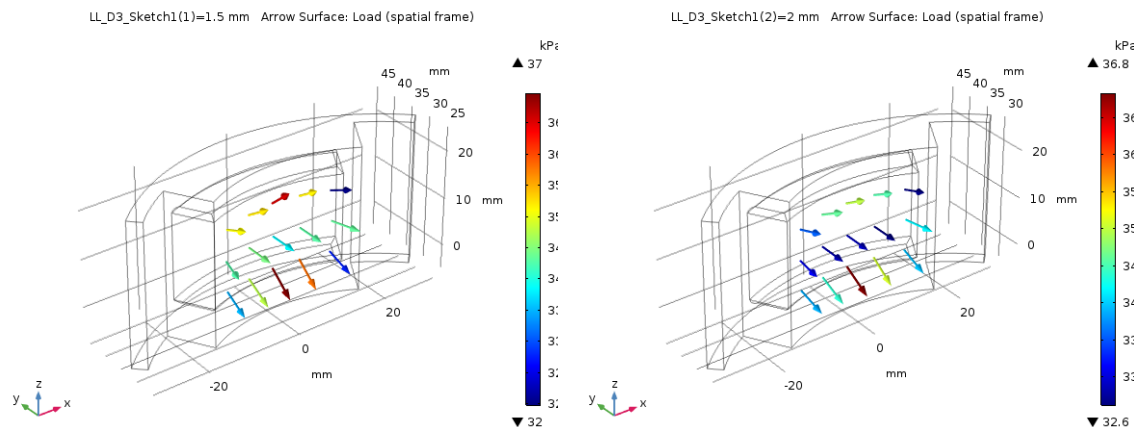


Figure 4.4 Displacement (δ_d) as a function of both (a) actuator height (h) and (b) arc angle (α) for $t_d = 2$ mm and $P_a = 6.89$ kPa.

4.2 Surface Loads

Conditions identical to the first study were then used to solve for surface loads (Figure 4.5). At an applied pressure of $P_a = 34.47$ kPa, each wall thickness can apply a proportional load. These surface loads can be defined as applicable contact pressures. With a $t_d = 1.5$ mm wall thickness, the actuator can apply a load of $P_c = 37$ kPa, whereas with thicknesses of $t_d = 2$ mm and $t_d = 2.5$ mm the actuator can apply loads of $P_c = 36.8$ and $P_c = 35.5$ kPa, respectively. These pressure values will be used later on in Chapter 5.



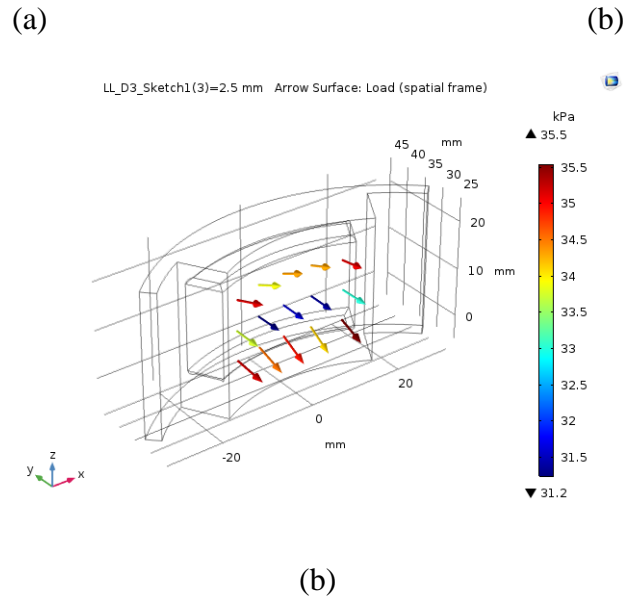


Figure 4.5 Simulated surface loads (P_c) with an applied pressure of 34.37 kPa. (a) $t_d = 1.5 \text{ mm}$; (b) $t_d = 2 \text{ mm}$; (c) $t_d = 2.5 \text{ mm}$

4.3 Relating to the Strain-Energy Function

To validate the accuracy of the simulations performed prior to comparison of computed results with the experiments outlined in Chapter 5, simulation results can be tied back to the governing equations. Recall from Section 2.1.1, where strain-energy is defined as the energy stored internally throughout a material's volume under deforming load. The total elastic strain-energy for the hyperelastic actuator model subjected to an applied pressure range of $P_a = 0 - 68.94 \text{ kPa}$ is shown in Figure 4.6. The data in the graphs shown in this section, as well as Section 4.4 for pressure-dependent data, are acquired from the same simulations as the data shown in Figure 4.6.

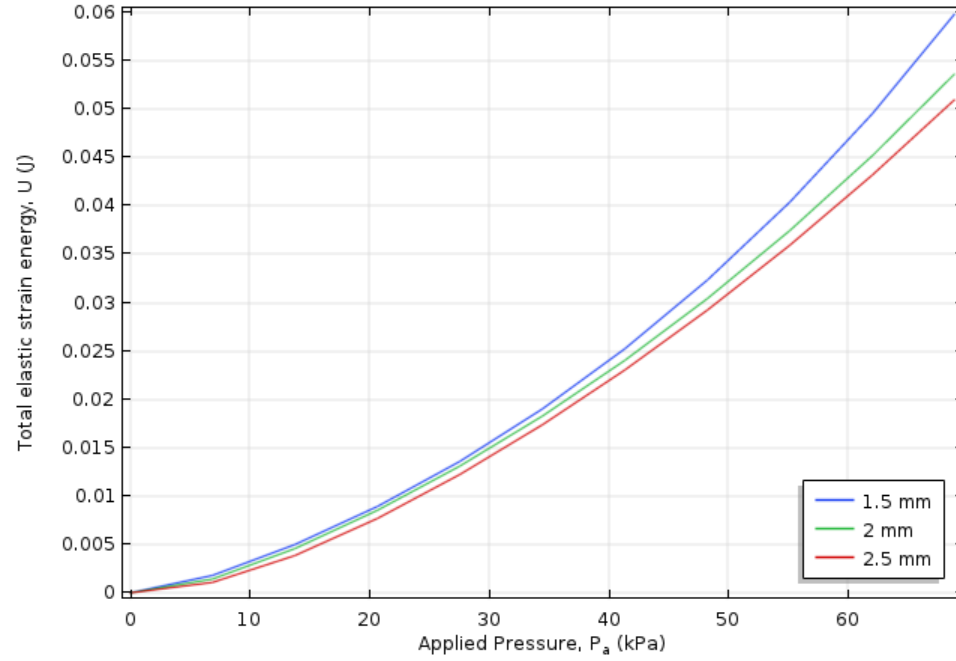


Figure 4.6 Simulated total elastic strain-energy (U) at different pressures (P_a , kPa).

Equation (2.4) then redefines the function to become the strain-energy per unit volume of material. The total stored strain-energy density is shown in Figure 4.7. The energy density is quantified in terms of J/m^3 .

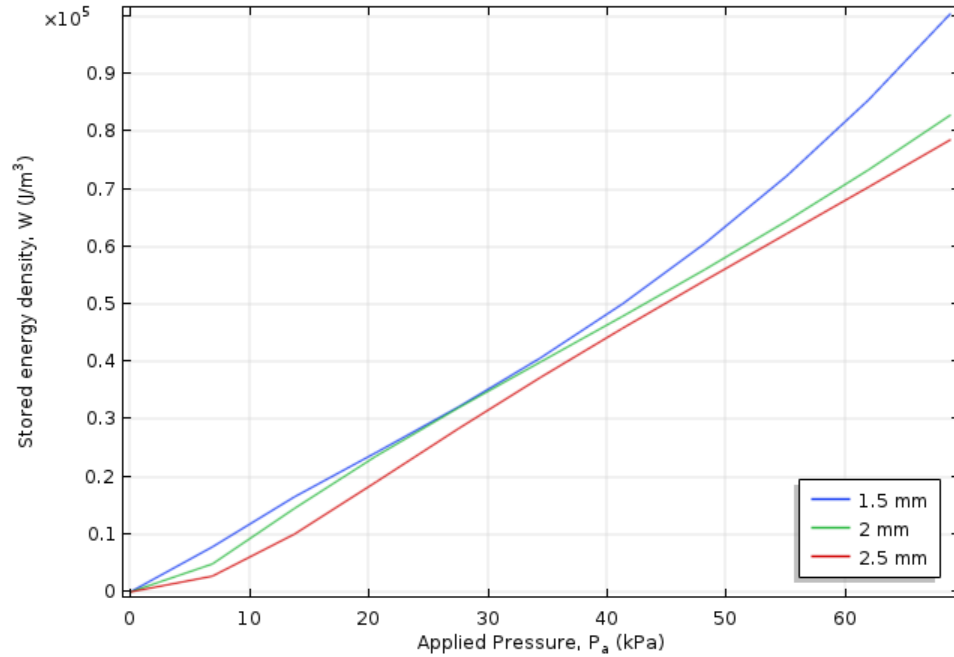


Figure 4.7 Simulated stored energy density (W) at different pressures (P_a , kPa).

As per equation (2.9), the strain-energy density function from equations (2.4) and (2.6) can be split into two distinct parts. The volumetric strain-energy density for all three actuator wall thicknesses is shown in Figure 4.8. The isochoric strain-energy density for all three actuator wall thicknesses is shown in Figure 4.9. Note that the sum of both graphs results in the total stored energy density from Figure 4.7. Thus, the relationship described by equation (2.9) is proven and the validity of the model setup in COMSOL Multiphysics is established.

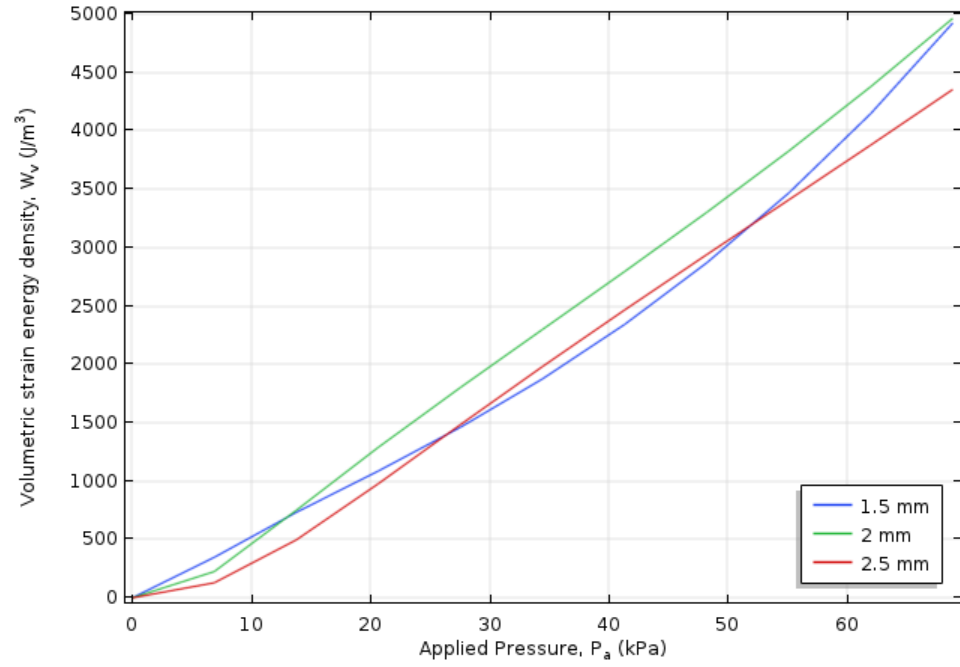


Figure 4.8 Simulated volumetric strain energy density (W_v) at different pressures (P_a , kPa).

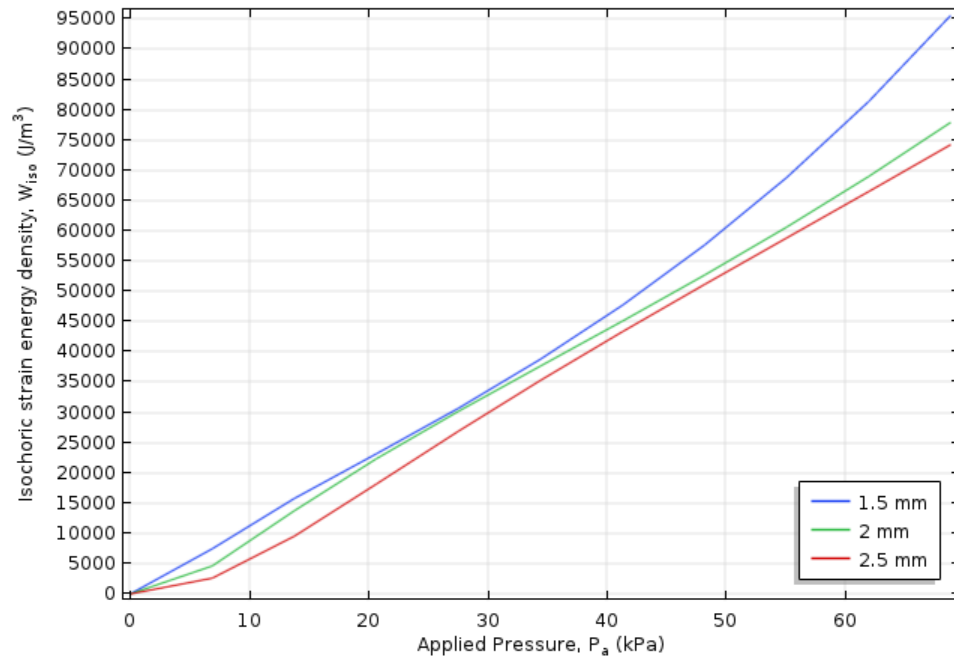


Figure 4.9 Simulated isochoric strain energy density (W_{iso}) at different pressures (P_a , kPa).

4.4 Principal Strain and Principal Stretch

Principal strain directions for nodes on the model's primary wall surface are shown in Figure 4.10 at the extremes of the applied pressure range of $P_a = 0 - 68.94$ kPa. Note the distinct change in direction between the two models shown, which define the deformation of the wall for a given applied pressure.

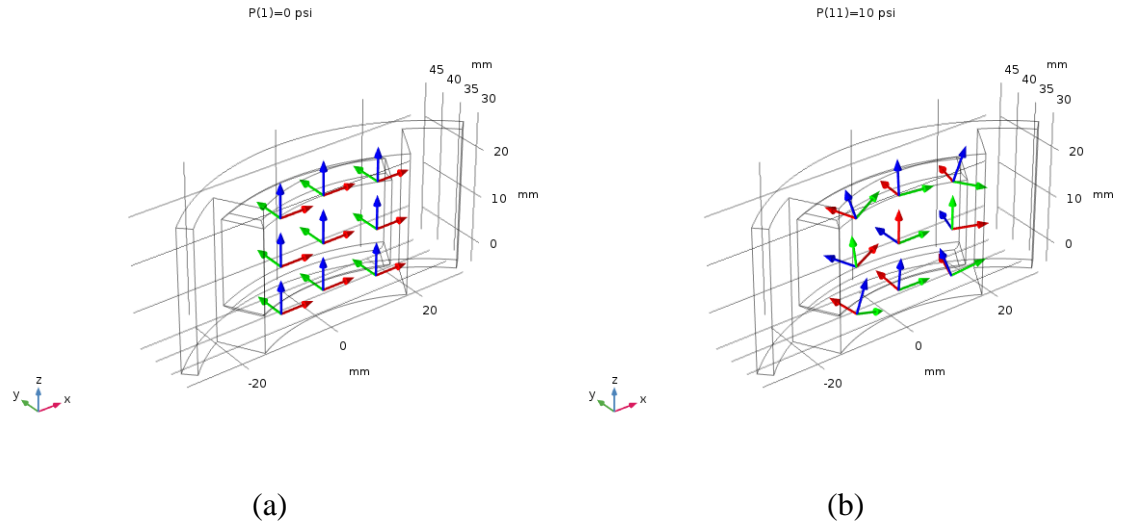


Figure 4.10 Principal strain directions under applied pressures (P_a , kPa). (a) 0 kPa; (b) 68.94 kPa.

The three principal strains for the element at the point in the center of the concave wall surface is shown in Figure 4.11. Recall from equation (2.7) that the principal stretch can be defined as the sum of the associated principal strain and 1. This is shown in Figure 4.12. Graphs shown are for a wall thickness of $t_d = 1.5$ mm. Graphs for the $t_d = 2$ mm and $t_d = 2.5$ mm show a similar trend and relationship.

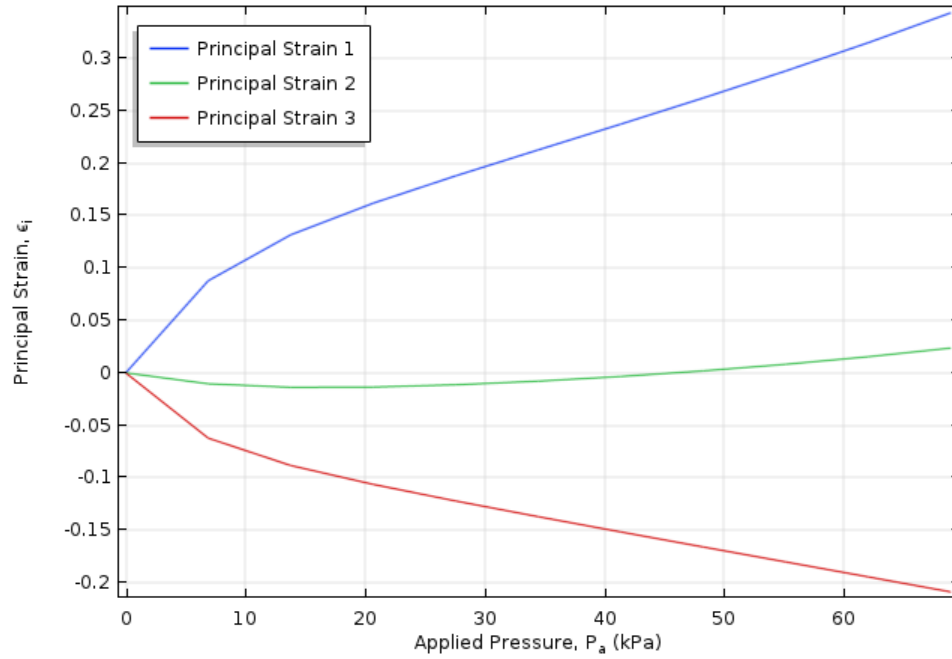


Figure 4.11 Principal strains (ϵ_i) under applied pressure (P_a , kPa) for an actuator wall thickness of $t_d = 1.5$ mm.

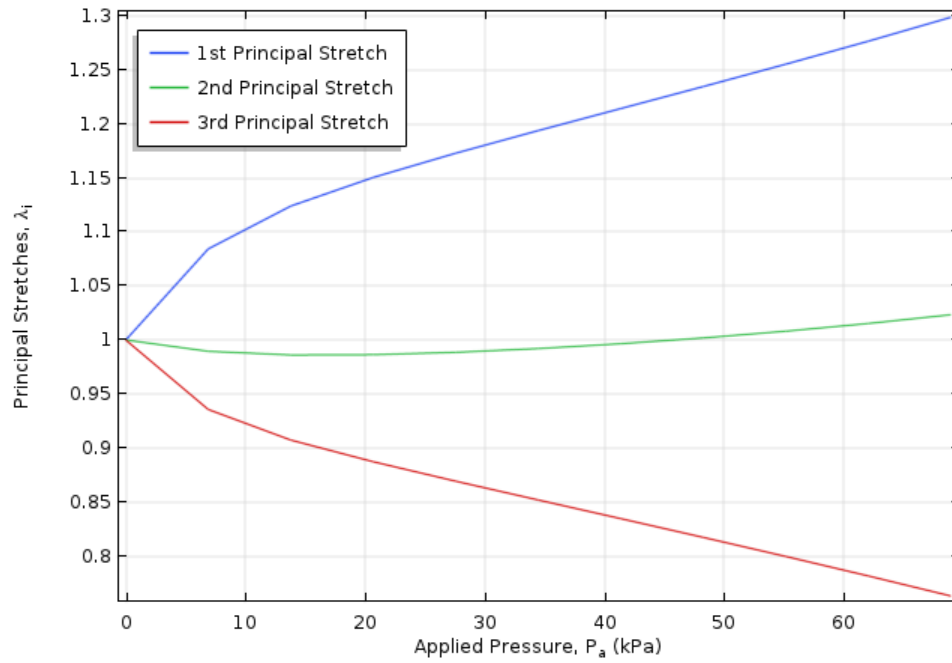


Figure 4.12 Principal stretches (λ_i) under applied pressure (P_a , kPa) for an actuator wall thickness of $t_d = 1.5$ mm.

Next, principal stretch ratios are simulated over a period of 1 second with an applied pressure of $P_a = 34.47$ kPa. For each wall thickness, the time-dependent simulations exhibit instability in the first few milliseconds of the study. Despite the instability shown, each case follows a trend similar to the principal stretches over a pressure range (Figures 4.13 – 4.15).

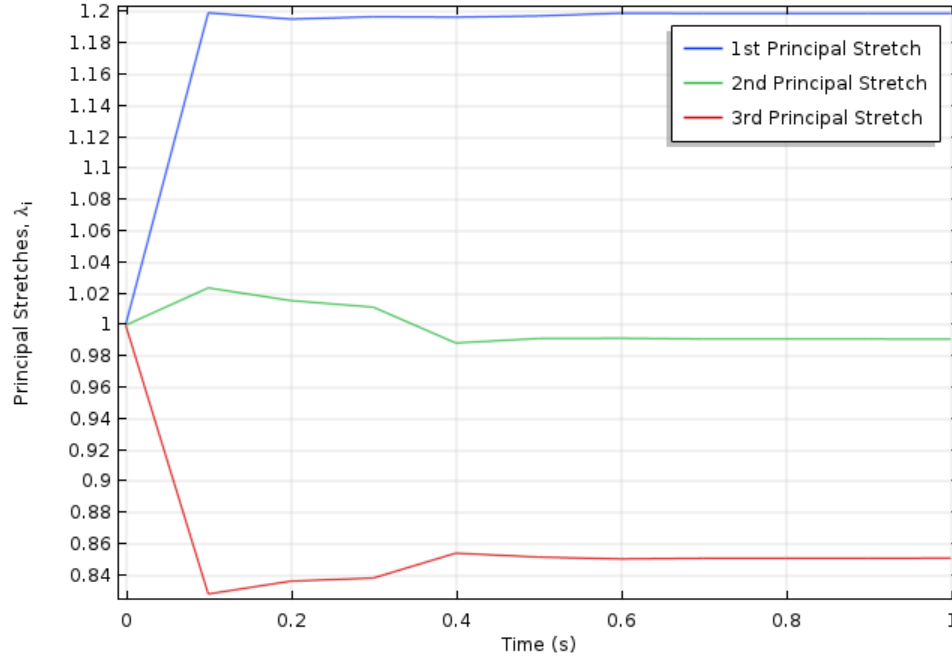


Figure 4.13 Principal stretches (λ_i) over time for an actuator wall thickness of $t_d = 1.5$ mm.

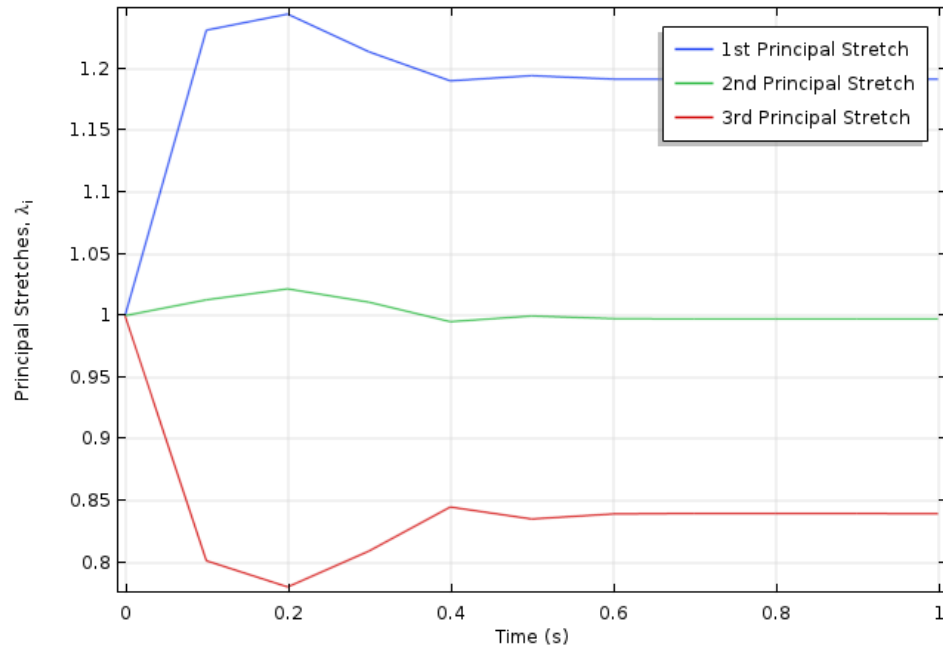


Figure 4.14 Principal stretches (λ_i) over time for an actuator wall thickness of $t_d = 2$ mm.

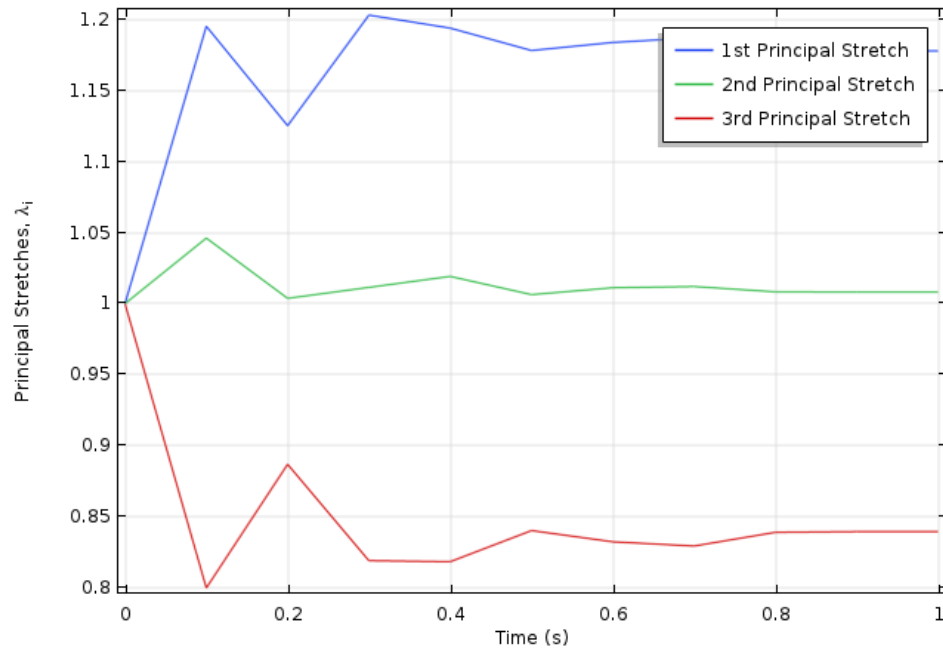


Figure 4.15 Principal stretches (λ_i) over time for an actuator wall thickness of $t_d = 2.5$ mm.

For both time-dependent and independent cases, simulation results for principal stretch ratios exhibit values less than 1.3. As per equation (2.7), this corresponds to a maximum strain value of 130%. Recall that in Section 2.2.2 the maximum strain of PDMS is listed as 150%. Thus, the strains produced in simulations are within acceptable limits.

4.5 Chapter Summary

This chapter outlined the simulations performed on the computational actuator model for deformation under load. Initially, displacement over a pressure range and displacement given different wall thicknesses were presented. Simulated data showed that for both cases the thinnest of the three simulated wall thicknesses exhibits the greatest displacement. Contact pressures were simulated in terms of surface loads, to be used in the following chapter. Results from simulating various chamber heights and arc lengths were presented. Data showed that while increasing chamber height in turn increases wall displacement, modifying arc length has a less significant impact. Simulations tying back to the strain-energy density function were performed. They proved that the use of COMSOL Multiphysics and the model setup implemented did not produce erroneous results. Principal stretches and principal strains were presented and related to each other. Time-dependent results exhibited a form of instability that may be caused by the application of an instantaneous load. Simulated values for maximum strain, acquired in terms of stretch ratios, are lower than the maximum strain before fracture of PDMS.

Chapter 5

Experimental Setup and Testing

With simulations completed, complementary experiments were developed and performed. This chapter outlines the setup for these experiments. Experimental results for an actuator subjected to a deforming pressure load are presented and compared to their associated COMSOL simulations. The setup and results of tests investigating the designs' gripping capabilities with curved geometries are also provided. Literature related to the design of soft pneumatic actuators typically include experiments investigating the actuator's durable life cycle [4], [33]. These tests may take weeks to complete and thus require a secure environment without any possibility of interference. The entirety of the experiments presented in Chapter 5 are performed in an open-access undergraduate laboratory. It is therefore not possible to perform any durability tests that may require a substantial period of time.

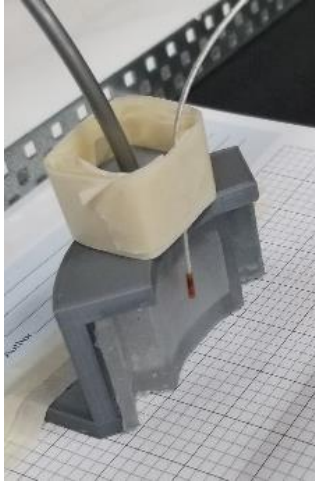
5.1 Actuator Displacement Under Applied Pressure

A series of experimental tests were performed on several fabricated PDMS actuators to examine the impact of changes in key design parameters (t_d, P_a) on the active wall displacement (δ_d). In all cases, the chamber height was fixed at $h = 20$ mm to match the width of the strain-limiting fiber strips used in fabrication. Furthermore, an arc angle of

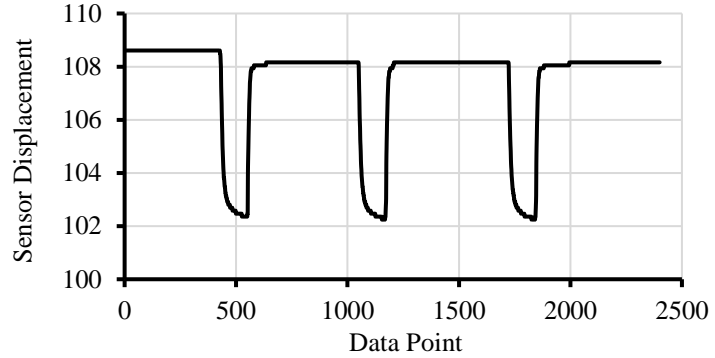
$\alpha = 60^\circ$ was selected because simulation studies showed that it was near optimal for the various fixed parameters of the proposed soft actuators and gripper housing unit. The thicknesses of the deformable walls for the tested actuators were $t_d = 1.5$ mm, 2 mm and 2.5 mm. Fabrication of these actuators is described in Section 3.2.

5.1.1 Experimental Setup

Fabricated actuators are attached to a 3D printed ABS backing structure. The displacement of the actuating surface was measured using a 3D Guidance TrakSTAR position sensor system (static accuracy ± 1.4 mm) [72] with an EM sensor capable of measuring 6 DOF (Figure 5.1a). The measurement values correspond to the distance between the sensor probe and fixed transmitter location. The displacement (δ_d) is, therefore, the change in distance with respect to the initial non-inflated actuating surface. For the experiments the applied pressure (P_a) was varied between 34.47 to 68.94 kPa (5 – 10 psi) at 6.89 kPa (1 psi) increments. For each (P_a) the displacement (δ_d) was measured three separate times over a 10 second time trial, for 1 second of actuation, at a sampling frequency of 120 Hz (Figure 5.1b). An average displacement reading is then calculated. The pressure range was selected because $P_a < 34.47$ kPa resulted in inaccurate readings due to the limitations of the pressure regulator and gauge used in the experiments. In addition, $P_a > 68.94$ kPa caused a number of the fabricated actuators to prematurely rupture.



(a)



(b)

Figure 5.1 Experimental setup and test procedure. (a) Testing of a single actuator with a positioning sensor; (b) Sensor data for displacement testing of a single actuator. The dips in the figure show three separate instances of displacement for one test. Note that this the test shown in this figure is performed over a period of 20 seconds. The time period is reduced to 10 seconds after the TrakSTAR system underwent initial calibration.

5.1.2 Measured Actuator Displacement

The measured and COMSOL simulated displacements for the three different wall thicknesses and an applied air pressure input of $P_a = 34.47$ kPa are shown in Figure 5.2. Note that the measured value is the average steady-state displacements over a 0.5 second window. The observed differences in the measured and simulated displacements ($|\Delta\delta_{m-s}|$) are partly the result of limitations in the Mooney-Rivlin hyperelastic model, the theoretical values for the shear and bulk moduli, and the computational limitations imposed by the size of the finite element mesh used in the simulations. These deviations may also be due, in part, to limitations in precise pneumatic control of the basic regulator used in testing (accuracy ± 1 psi) and the static accuracy of the TrakSTAR positioning sensor (± 1.4 mm). The smallest difference occurs at $t_d = 2$ mm where $|\Delta\delta_{m-s}| = 0.08$ mm and the largest at $t_d = 2.5$ mm where $|\Delta\delta_{m-s}| = 1.11$ mm. The latter case represents a $\sim 25\%$ error.

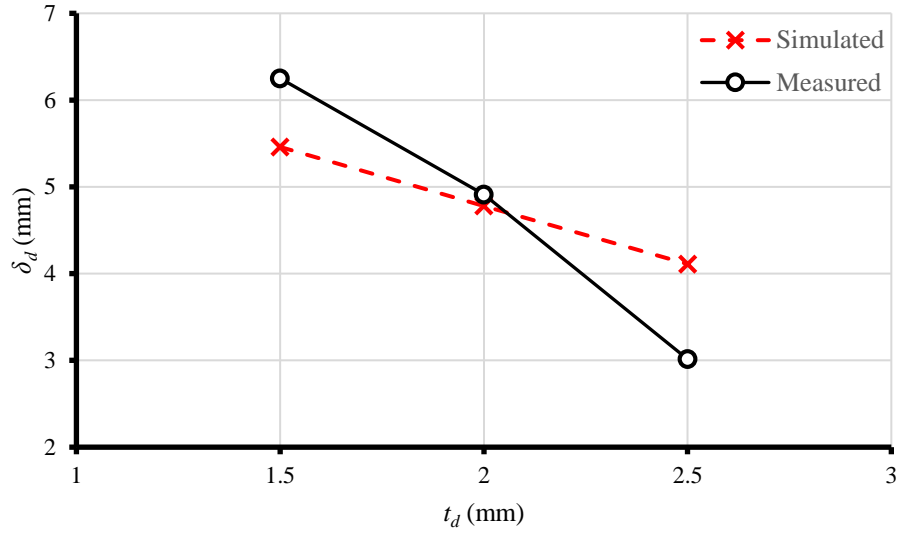


Figure 5.2 Comparison of measured and simulated data for wall displacements (δ_d) for different wall thicknesses (t_d).

5.1.3 Wall Displacement over Pressure

Figure 5.3 shows the impact of changes in (P_a) on the displacement of the actuating wall (δ_d) for each wall thickness. The deviation between simulated and experimental data may be due to limitations introduced by the hyperelastic material model. Though simple in its implementation, the Mooney-Rivlin model is unable to capture larger strains measurable by more comprehensive material models [23]. However, a more accurate model would require additional variables that can only be acquired through additional testing of material samples. Again, discrepancies between the compared data sets could also be attributed to experimental errors related to pneumatic pressure control and sensor positioning.

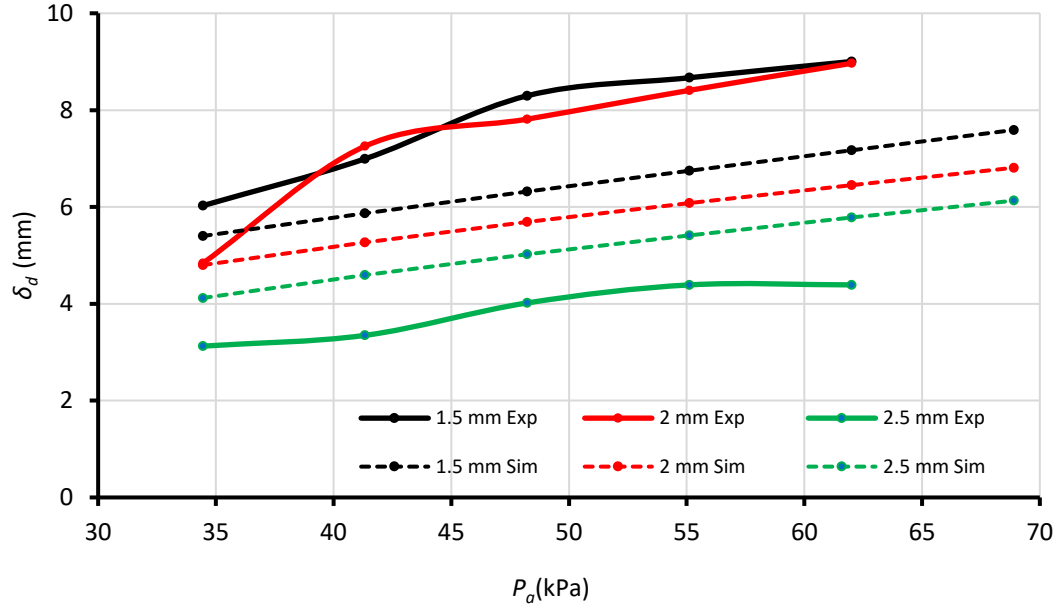


Figure 5.3 Comparison of experimental and simulation data for wall displacement (δ_d) at different input pressures (P_o) for different wall thicknesses (t_d).

5.2 Gripper Contact Forces and Maximum Payload Capabilities

5.2.1 Experimental Setup

Contact forces of each gripper geometry are characterized with a combination of simulation results and experimental testing. For simulations, a pressure of $P_a = 34.47$ kPa is applied to the interior of the COMSOL model's displacing wall. Contact pressure is acquired in kPa as a load applied by the displacing wall's whole concave surface in Section 4.1. To experimentally measure contact area when the actuator applies pressure to the surface of the target object, paint is applied to the deformable walls of the soft actuators in the gripper assembly and the device is then used to grasp a Styrofoam sphere (dia. 60 mm). When the target sphere is released after pressure has been applied, an imprint of (A_c) is left on the surface in the form of three marks. The dimensions of these marks are measured and recreated in SolidWorks (Figure 5.4), where the contact area can then be obtained. In

general, the contact force is a function of the contact pressure (P_c) and area of contact with the target (A_c), and can be simply given as

$$F_c = P_c \cdot A_c \quad (5.1)$$

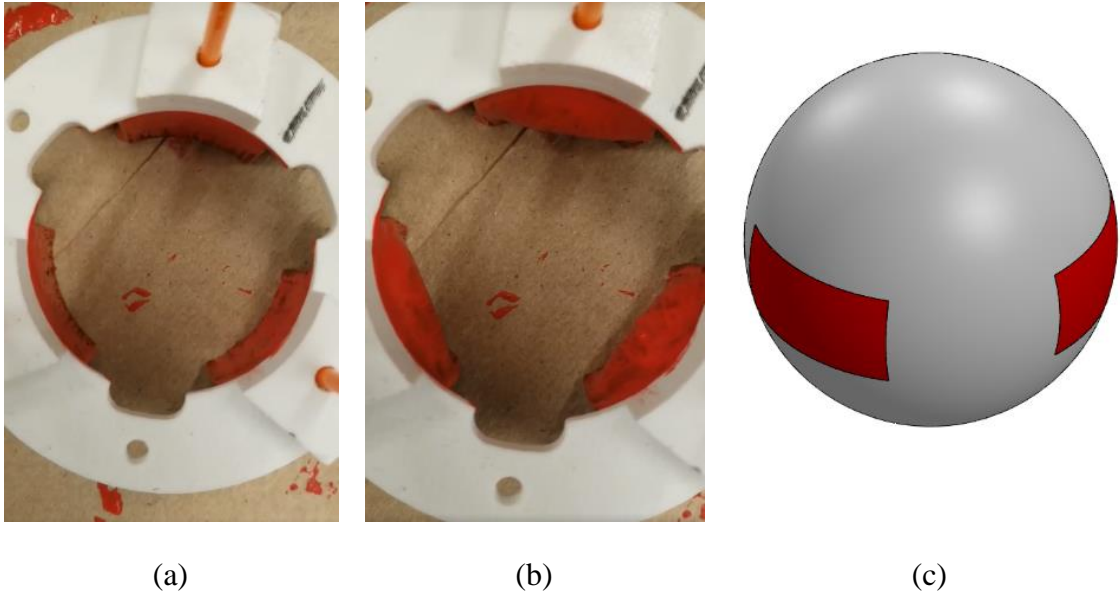


Figure 5.4 Setup for contact force tests. Top view of painted gripper ring in (a) deflated and (b) inflated states; (c) 3D model of contact area on sphere.

It is also important to investigate the design's grip strength by measuring the payload capabilities of the pneumatic gripper with different actuator wall thicknesses. In this experiment, a Styrofoam sphere and cylinder with equal diameters (dia. 60 mm, cylinder height 30 mm) are used as the target objects (Figure 5.5). Each target was modified by attaching a 50 g payload platform that would enable additional weights to be applied in a controlled fashion. This apparatus created a downward force on the grippers hold on the object and is represented as a slip test payload mass (m_L). The maximum payload of the soft pneumatic gripper is verified using free weights.

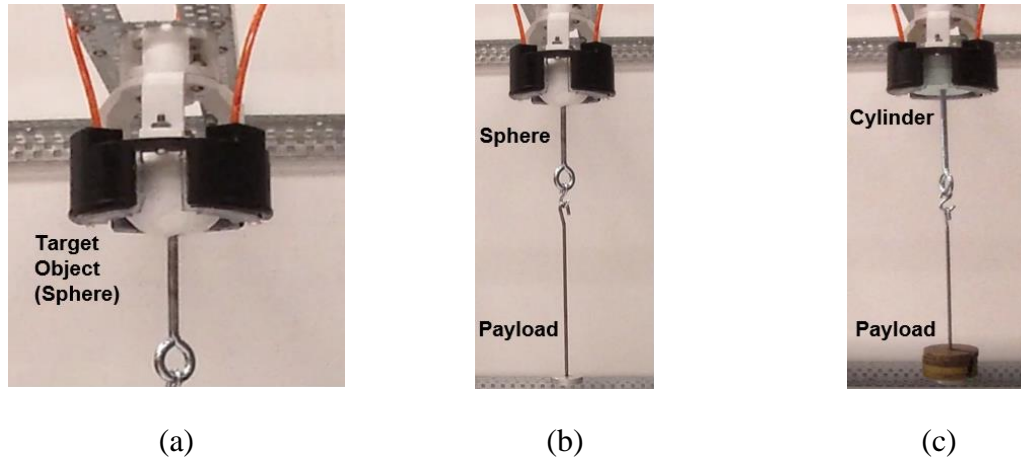


Figure 5.5 Experimental setup for payload tests. (a) Close-up of spherical target held in gripper; (b) sphere target for payload test; and (c) cylindrical target for payload test.

5.2.2 Contact Force and Maximum Payload Results

At a single constant pressure input of $P_a = 34.47$ kPa, thicker actuator walls result in lower displacements and lower contact pressures. This means that the actuator wall is not being forced against the target object, in this case the foam sphere, and is not pushing the soft target structure away. The result is that more of the actuator's deforming wall is in contact with the target, thus the contact area is greater. Using equation (5.1) it is found that thicker deforming wall thicknesses offer greater contact forces as the contact pressures are distributed over a larger area.

Overall, the grippers exhibit roughly double the maximum payload capacity for cylindrical shapes over spheres. This may be due to the greater surface area that the actuators can come into contact with. At these maximum payloads, and with similar gripper weights of about 76 g, the $t_d = 1.5$ mm, 2 mm and 2.5 mm gripper variants have respective payload-to-weight ratios of 30, 26, and 18. These results, however, appear contrary to an initial assumption that the maximum payload tests would follow the same trend as contact force experiments. The inverse relationship may be the result of increased surface friction between the thinner inflated elastic actuator and target object. Clearly, the surface effects

between the hyperelastic actuator and object need to be explored in greater detail. Results for both contact force and payload tests are shown in Table 5.1.

Table 5.1 Contact force and payload test results for all gripper geometries. Test object is a foam sphere unless stated otherwise in brackets.

Wall Thickness (t_d)	Contact Pressure (P_c)	Contact Area (A_c)	Contact Force (F_c)	Slip Test Payload (m_L)
1.5 mm	37 kPa	424.4 mm ²	15.7 N	1.175 kg 2.3 kg (cylinder)
2 mm	36.8 kPa	498.5 mm ²	18.4 N	0.875 kg 1.975 kg (cylinder)
2.5 mm	35.5 kPa	542.3 mm ²	19.3 N	0.675 kg 1.375 kg (cylinder)

5.3 Chapter Summary

This chapter outlined the experiments performed in this research. Actuator wall displacement showed a match within ± 1.11 mm between simulated and experimental results. Comparison of displacement values over a range of applied pressures showed greater discrepancy between simulations and experiments. This may be attributed to limitations of the hyperelastic material model used or experimental error. Regardless, the close match between the displacement values proves that simulations could be used to improve the design of soft robotic actuators by reducing the number of iterations required. However, the associated $\sim 25\%$ error also shows that the method presented is not yet a precision tool. Gripper tests investigating contact forces present that the applied load is distributed over a broad surface area. Thicker actuator walls allowed the load to be applied over a greater area, resulting in a higher contact force. Payload tests that establish the designs' gripping capabilities with curved geometries are provided. Payload capabilities are greater with thinner actuator walls, and the maximum payload is doubled for curved geometries with larger applicable contact area.

Chapter 6

Application Study and Discussion

This chapter outlines the comparative study between the novel soft PDMS gripper designs and standard vacuum cup grippers in a mushroom harvesting application. The performance of each tested gripper is evaluated in terms of gripper success and damage inflicted. In addition, a summary of design guidelines to modify the gripper design for different applications is provided. It is important to note the difference between experiments in laboratory and field settings. Individual mushrooms are used for in-lab testing. In reality, mushrooms grow in densely packed growing beds. Different sizes and shapes of fungi may overlap one another, making gripping with the design proposed in this thesis difficult if not impossible. This is due, in part, to the 3D printed housing ring to which the actuators are connected. The 3D printed ring is neither optimal nor appropriate for a true field test. Its sole purpose is to act as a robust frame that can hold and protect the PDMS actuators. The goal of the application study presented in this chapter is therefore not to verify the current design for a true field test, but to assess the design's capability of grasping a delicate structure without inflicting any damage.

6.1 Robotic Harvesting Systems in Horticulture

Every automated harvesting system in the horticultural sector is dependent on its unique working environment (i.e., crop environment). A system's specific crop environment is

influenced by sources of variation. There can be significant variety between objects in the same crop. They can be in uncertain or poorly defined positions, and have different shapes, sizes and colors. In some cases, these objects can be overlapping or covered by obstacles, making them difficult to reach and collect. Environmental conditions suitable for production of a specific crop can also introduce new factors such as weather, lighting, humidity, and harvesting space. Both sources of variation become distinct when considering a specific high-value crop [10].

Though each robotic harvesting system must be designed for a specific high-value crop, they share common engineering specifications. A review by N. D. Tillett [73] states that, for horticultural applications, typical robotic manipulator systems have a maximum payload of at least 1 kg. For manipulators using pneumatic gripper systems, the static point-to-point accuracy for target alignment is generally ± 1 mm, though it can be influenced by the degree of compliance in the gripper structure. Dynamic accuracy for trajectory control and collision prevention can be ± 10 mm, though it is usually only considered in special cases such as outdoor applications in high wind conditions. It can be considered for this research thesis, as a compliant soft gripper is likely to sway and jolt under motion.

Common performance indicators can be used to evaluate all robotic harvesting systems. Indicators relevant to this research thesis are shown in Table 6.1. Reported performance values are listed from the review by Wouter Bac et al. [10]. They are calculated averages over several different harvesting studies.

Table 6.1 Standard performance indicators for robotic harvesting systems.

Performance Indicator	Reported Performance	Description
Harvest Success (%)	75%	Successfully Harvested vs. Sample Size
Damage Rate (%)	5 %	Damaged vs. Sample Size
Sample Size (#)	6 – 2500	Number of Objects per Test

6.1.1 Review of Existing Mushroom-Harvesting End-Effectors

There have been numerous patented attempts at developing suction-based robotic mushroom harvesters. This following section provides a description of some of these systems. Though the patents are for the whole robotic system, this section will focus primarily on their vacuum-based end-effectors.

6.1.1.1 “Harvesting of Delicate Produce”, Patent Number US 5,058,368

Issued on October 22, 1991, the device patented by Wheeler et al. [18] includes a bellows-style suction gripper with an internal porous foam block. The block is intended to support the mushroom cap, distributing the grasping forces generated by vacuum pressure over a larger area. Once the cup has a hold on the target mushroom, it is harvested with a series of lifting and twisting actions. After being lifted from its growing bed, the mushroom stem is removed with a cutting blade. The mushroom is then deposited in an adjacent box. The flaw discovered with this design is that the porous foam block would quickly fill with compost and debris from the mushroom growing bed. This resulted in a disruption of the vacuum flow required to pick up the mushrooms.

6.1.1.2 “Device for the Automatic Selective Harvesting of Mushrooms”, Patent Number US 5,471,827

Another system, the patent of which was issued on December 5, 1995, to Janssen et al [21], includes a suction cup gripper with a long series of bellows. This long bellows is intended to compensate for the possibility of angled mushroom targets. Not all mushrooms grow in a completely vertical direction. Some grow on oblique angles or are pushed to some orientations by their larger neighbors. Using a longer bellows component allows the suction cup to deform to match an angled target’s orientation. Once the suction cup is aligned with the mushroom and grasping contact is made, the target is again harvested with a series of lifting and twisting motions before being destemmed with a cutting blade. The problem with this design is that it was not capable of providing sufficient angular and axial rigidity

to make the required lifting and rotating motions to harvest the target from its growing bed. A longer column of flexible and uncontrolled bellows also creates additional complexity in trying to make contact with any mushroom targets, angled or vertical.

6.1.1.3 “Apparatus for Picking Mushrooms”, Patent Number US 8,033,087 B2

The patent issued on October 11, 2011, by Rapila et al. [17], describes a harvesting system that uses commercially available suction pads for gripping mushrooms. The system again collects the target through a series of twisting and lifting actions. Testing of several commercially available suction cups [19] has shown that they are not well-suited for harvesting mushrooms. Standardized commercial suction cups inflict increased damage to the mushroom cap, in the form of discoloration, bruising and denting. Standard cups are also unable to support a practical range of cap diameters. This patent is mentioned in this thesis to introduce the use of commercially available vacuum cups. It provides justification for the work on custom vacuum cup geometries, as described in Appendix B.

6.1.1.4 “Mushroom Harvester”, Patent Number WO/029299 A1

The system patented on March 3, 2016 by Van De Vegte et al. [19] includes a robotic end-effector that is configured to interchangeably switch between multiple different suction grippers. Each gripper configuration has a suction cup with a size and shape profile intended for gripping a range of mushroom cap diameters and geometries. This system is still at the Vineland research facility and was in use before the switch over to the PreciseFlex infrastructure (Appendix C). Vineland’s reasoning behind the transition to the PreciseFlex system is partly due to the complexity of this design and the size constraints associated with the cramped Dutch Shelving organization method. The manipulator system that this gripper design is intended for is unable to fit within the cramped growing environment with Vineland’s proprietary identification system. In addition, despite the wide range of grasping capabilities introduced by the interchangeable cup sizes, the suction cups still inflicted damage to the grasped mushroom.

6.1.2 Standard Vacuum Cups Provided by Vineland

Vineland has also provided two of the vacuum cups that they use for harvesting mushrooms. The first (Figure 6.1a) is a common bellows-type cup [74] commonly used for robotic pick-and-place operations. The second (Figure 6.1b) is the bell-type suction cup [75], originally used to collect soft chocolates. The bell-type cup is used as the starting template for iterations that are presented in Appendix B.



(a)



(b)

Figure 6.1 Commercially-available vacuum cups provided by Vineland. (a) Bellows-type cup; (b) Bell-type cup.

6.2 Parameters for Evaluation

Application tests are performed to compare the performance of the proposed soft gripper with the commercial vacuum cups. Each test consists of manually placing the gripper over a mushroom and attempting to lift it. The mushrooms are wedged onto a threaded bolt to simulate being embedded in a soil bed, as shown in Figure 6.2. Parameters for analysis are grasping success and damage inflicted.

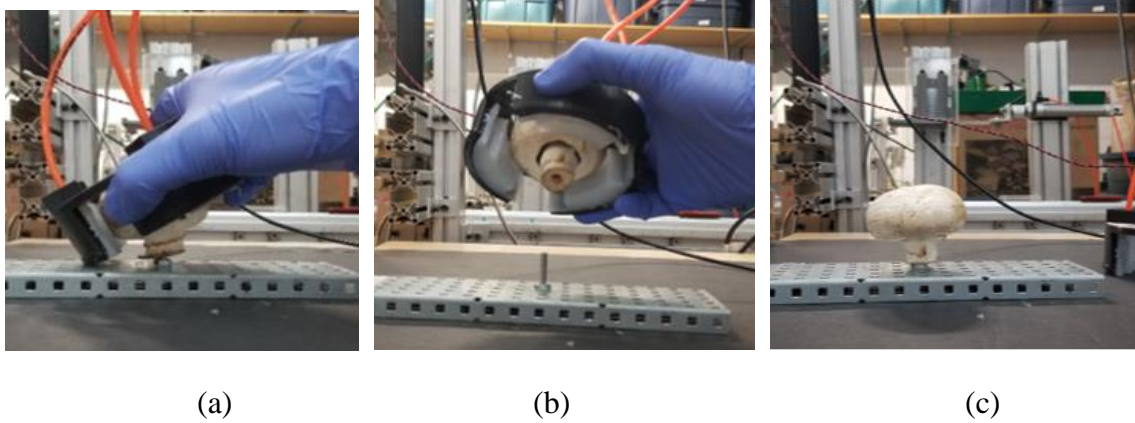


Figure 6.2 Experimental setup and manual test procedure. (a) Gripper placed over mushroom; (b) Gripper lifting mushroom from threaded rod; (c) Organic test object (i.e., mushroom) embedded on threaded rod.

Grasping success is determined by whether the end-effector is capable of getting a hold of the target mushroom on the first attempt. Dropping the mushroom or being unable to make sufficient contact to lift it are both considered failures. Damage infliction is assessed by whether the gripper causes any disfigurement to the mushroom surface on contact. Note that damage tests are qualitative and based on observation, not measurement.

6.3 Application Testing

Commercial vacuum cup structures have already been discussed in Section 6.1.2. Designated as the Bellows and Bell-type cups, each is tested for a sample size of $n = 8$ mushrooms. The Bell-type cup is also the starting template for three custom cup geometries. All information related to these custom structures is available in Appendix B.

Tests for the vacuum gripper are initially performed at 68.94 kPa of compressed air input. Conversion to vacuum pressure and losses in the rudimentary vacuum system used result in a corresponding vacuum pressure of 0.85 kPa. Note that for the bellows cup, another series of tests were performed at 82.73 kPa, which corresponds to 1.19 kPa. Performance data for the vacuum cup gripper geometries are shown in Figure 6.3.

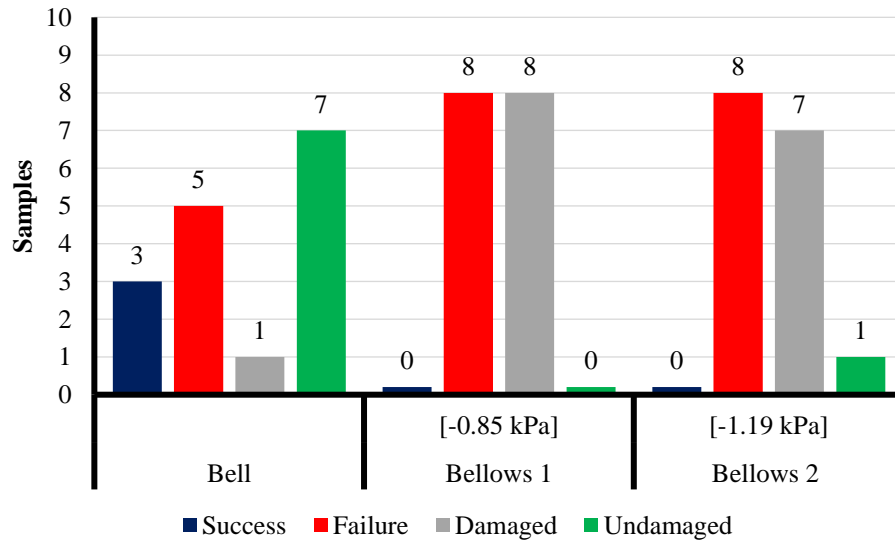


Figure 6.3 Results of grasp-and-hold experiments (success/failure) and observed damage to mushroom surfaces during the tests (damaged/undamaged). These results are for tests with the vacuum cups.

The Bell-type suction cup was able to successfully collect the mushroom for less than $\frac{1}{2}$ of the grasping attempts. Only one of the grasping attempts resulted in damage to the mushroom cap structure. The Bellows-type cup was unable to grasp the target mushroom in any case. Damage was inflicted to the mushroom cap in all but one attempt. Damage inflicted was typically observed in the form of an indented ring (Figure 6.4).

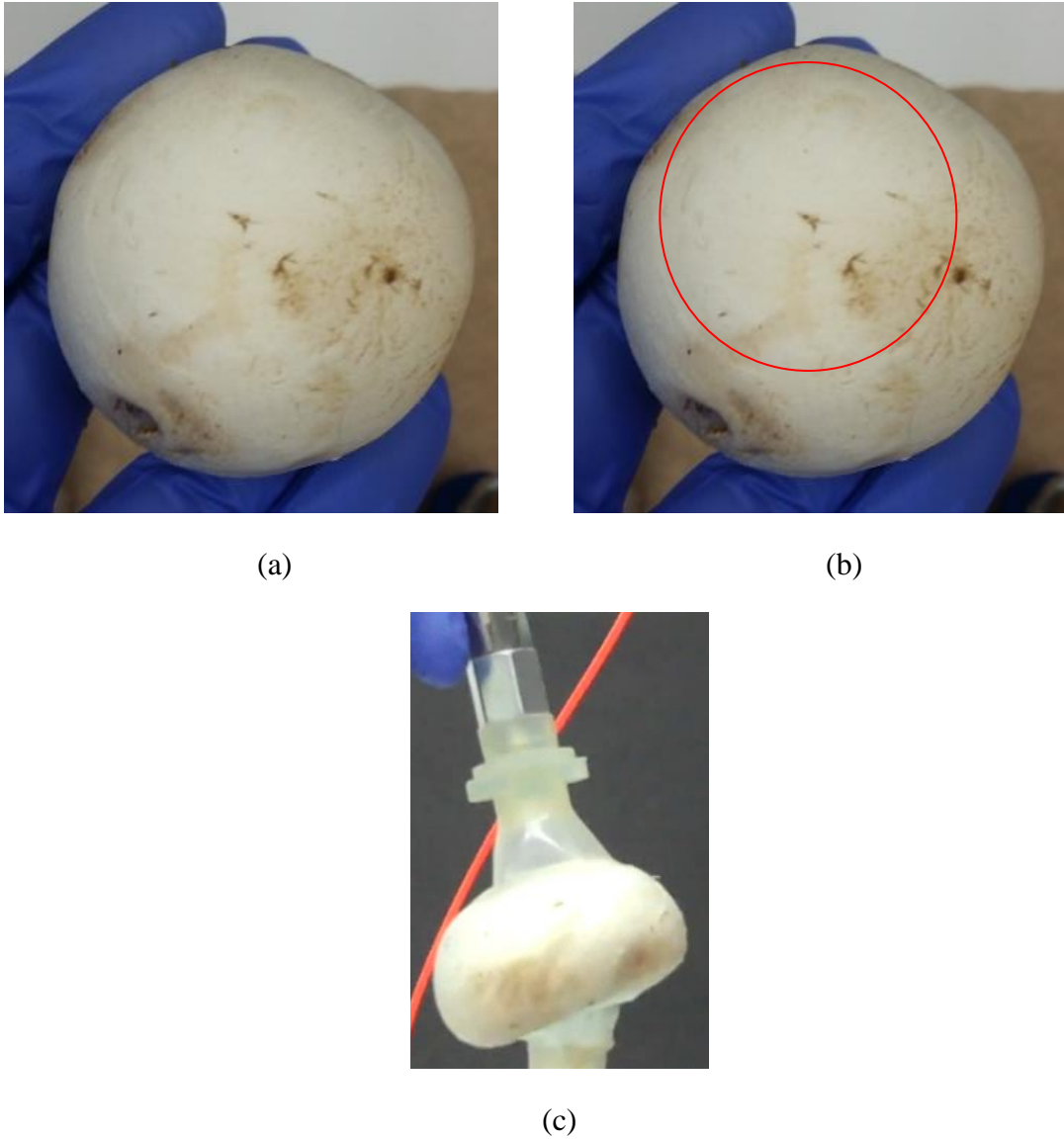


Figure 6.4 Observed damage on mushroom cap inflicted by vacuum cup. (a) Indented ring of damage; (b) Inflicted damage outlined with red circle; (c) Bell-type cup geometry collapsing under vacuum pressure.

The PDMS soft actuators were assembled in three gripper assemblies with concave wall thicknesses of $t_d = 1.5$ mm, 2 mm and 2.5 mm. For each gripper assembly two sets of tests were performed with the applied air pressure (P_a) equal to 34.47 kPa (5 psi) and 41.37 kPa (6 psi), respectively. A single test involved grasping, pulling and holding $n = 30$ organic mushrooms of similar size. At $P_a = 34.47$ kPa, the experimental observations of

the various soft grippers (Figure 6.5) indicate that PDMS actuators with $t_d = 1.5$ mm and 2 mm performed well for both the grasp-and-hold(success/failure) and minimal infliction of surface damage (damaged/undamaged). In contrast, the gripper with soft actuators that had wall thickness of $t_d = 2.5$ mm failed $2/3^{\text{rds}}$ of the grasp-and-hold tests but still did not produce any significant surface damage on the target mushroom. For the second test set, at $P_a = 41.37$ kPa, all soft gripper variants exhibited perfect rasping success. In all cases, the proposed soft pneumatic gripper did not inflict any damage to the mushroom cap surface.

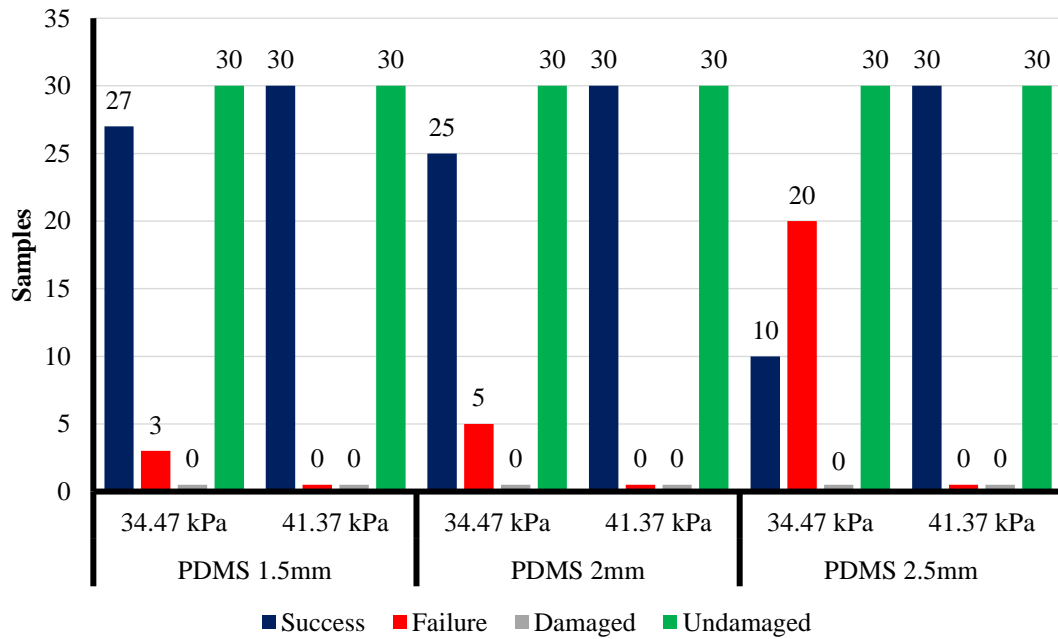


Figure 6.5 Results of grasp-and-hold experiments (success/failure) and observed damage to mushroom surfaces during the tests (damaged/undamaged). These results are for tests with the soft PDMS gripper variants.

6.4 Discussion of Results

The new soft gripper design has demonstrated greater performance than the conventional vacuum cups. This higher performance suggests that the broader force distribution applied by the soft grippers resulted in the elimination of contact-based damage. Table 6.2 provides

CHAPTER 6. APPLICATION STUDY AND DISCUSSION

a quantitative comparison of the soft grippers' performance with respect to the vacuum cups. The table also lists the general performance indicators listed in Table 6.1, including the ± 1 mm static accuracy standard in harvesting manipulator systems. Using the ± 1.11 mm match between the simulated and experimental results for wall displacement, presented in Chapter 4 and Chapter 5, respectively, the accuracy of the actuator's displacement is in relative accordance with the reported value for harvesting manipulators. The listed ± 1.4 mm static accuracy for the TrakSTAR positioning sensor is also acceptable relative to the listed manipulator value.

Table 6.2 Comparison of test results for Vacuum Cup and PDMS Soft Gripper performance with reported performance indicators in literature.

Performance Indicator	Reported Performance	Vacuum Cup			Soft Gripper						Description
		Bell	Bellows		1.5 mm		2 mm		2.5 mm		
			-0.85 kPa	-1.19 kPa	34.47 kPa	41.37 kPa	34.47 kPa	41.37 kPa	34.47 kPa	41.37 kPa	
Harvest Success (%)	75.0%	37.5%	0.0%	0.0%	90.0%	100.0%	83.3%	100.0%	33.3%	100.0%	Successfully harvested vs. Sample Size
Damage Rate (%)	5. %	12.5%	100.0%	87.5%	0.0%	0.0%	0.0%	0.0%	0.0%	0.0%	Damaged vs. Sample Size
Sample Size (#)	6-2500	8	8	8	30	30	30	30	30	30	Number of Objects per Test
Static Accuracy (± mm)	± 1 mm	-			± 1.11 mm						Simulated vs. Experimental

Comparing the vacuum cup performance to the reported indicators show that, within the conditions of the experiment, the cups are not suitable for a mushroom harvesting application. The only cup to achieve any success in grasping the mushroom, the Bell cup, exhibited a grasping success percentage (37.5%) that was only half the reported indicator (75%). Increasing the vacuum pressure may improve grasping success at the potential risk of increasing the damage rate. Figure 6.4c shows the Bell-type cup deforming under the vacuum pressure. The more rigid Bellows-type cup did not exhibit such compliance, which may have caused the significantly higher damage rate. During the first test case for the Bellows-type cup, all mushrooms are damaged (100%). The second case shows a lower damage rate (87.5%), corresponding to 1 of an $n = 8$ sample size. Future studies should be conducted with higher sample sizes to provide more accurate characterization of the vacuum cup's performance.

In terms of the reported performance, the soft gripper design surpasses the performance of current harvesting systems. At an applied air pressure of $P_a = 41.37$ kPa, each tested variant of the soft gripper design exhibits 100% grasping success and a 0% damage rate. A sample size of $n = 30$ for each test provides greater accuracy over the vacuum cup tests' smaller sample size, but future studies should be conducted with significantly higher sizes. It is important to note that these reported indicators are for multiple harvesting manipulator systems, for different crops, in both lab and field operations. This research focuses entirely on the performance of a single manipulator component, the end-effector, in a lab environment. Performing tests in a field environment, that is by attaching the gripper design to the PreciseFlex manipulator and attempt to harvest mushrooms from a growing bed, would have the dual benefit of significantly increasing the sample size and provide a realistic assessment of the gripper's utility. Due to unforeseen and unknown circumstances it was not possible to perform field experiments for this research.

6.5 Design for Different Applications

The proposed pneumatic hyperelastic actuator and curved gripper design were able to successfully grasp and hold light-weight delicate objects. In addition, the compact gripper geometry was not affected by gravity in the same manner as longer soft actuator designs, thereby making it suitable for attachment to conventional robotic manipulators with spherical wrists. Simulated studies on the generated model and experimental tests on the fabricated prototypes suggest that the current gripper design could be easily modified and adapted for a variety of applications including, but not limited to, the harvest of horticultural products. By modifying the geometrical parameters and input pressure, the gripper design can be adapted for different targets. For example, the thickness of the actuator's deforming wall (t_d) could be adjusted for different target loads or target geometries. In addition, the actuator height (h) can be changed for different target sizes or to change the number of active actuators in the gripper assembly (i.e., more than three).

Modifying the arc of the actuator (α) had minimal impact on the performance but this parameter can be adjusted to accommodate more or fewer actuators in an assembly. For example, the design can be reduced to two actuators opposing each other to grasp flat objects by its sides. Another example would be to increase the number of actuators (and, therefore, the gripper's overall size) to grasp a much larger object that would require a greater number of contact points. A summary of application-dependent design guidelines is provided in Table 6.3.

Table 6.3 Summary of design guidelines.

Target Condition	Performance Requirement	Design Adjustment
Heavier Target	Increased Maximum Payload (m_L)	Decrease t_d
Larger Target	Greater A_c and F_c	Increase both t_d and h ; Increase Number of Actuators
Delicate Target Structure	Greater Distribution of A_c and F_c	Increase t_d
Flat Target Geometry	Adapt to Different Target Shape	Reduce Number of Actuators (i.e., only 2)

6.6 Chapter Summary

This chapter outlined the comparative study between the soft PDMS gripper and vacuum cup grippers in use at the Vineland facility. The comparison was presented in terms of a mushroom harvesting application. All soft gripper prototypes tested at $P_a = 41.37$ kPa showed overall higher grasping success than the vacuum cups. What distinguished the soft grippers as viable replacements for vacuum cups is the observed damage inflicted. Both vacuum cup geometries tested inflicted some damage to the mushroom surface in at least one of the tests. The soft grippers inflicted no damage to the mushroom surface during any of the tests. Simulated and experimental data from Chapters 4 and 5, combined with the application performance evaluated in Chapter 6, suggest that the actuator and gripper designs can be modified and adapted for different applications. A summary of design guidelines is finally provided.

Chapter 7

Concluding Remarks

7.1 Summary of Thesis

In its entirety this thesis offers the background information, theoretical equations and analysis required for the design of a compliant hyperelastic actuator, using a hybrid simulation-experiment design process. Polydimethylsiloxane (PDMS) was selected because it is a hyperelastic material with well-known properties and, therefore, can be analyzed through computational simulations using nonlinear COMSOL Multiphysics software, which are detailed in Chapter 4. The comparative analysis described in this work was able to match data for the simulated displacement of a deforming actuator wall with its empirical equivalent within ± 1.11 mm. Once the comparison was performed, three identical soft actuators were formed in a gripper assembly to investigate the design's viability for harvesting delicate structures like the *Agaricus Bisporus* mushroom. Tests performed at $P_a = 41.37$ kPa in a laboratory environment showed that the gripper design performed with a 100% success rate for gripping the mushroom cap by its sides, and a 0% damage rate by not leaving any mark on the mushroom geometry.

Chapter 1 of the thesis describes how this work fits into the scientific community of existing research on the topic of pneumatically-driven soft robotic grippers. Specifically, existing research typically implements tedious trial-and-error experimentation on multiple design iterations of soft actuators and grippers fabricated with ultra-soft and unpredictable

CHAPTER 7. CONCLUDING REMARKS

hyperelastic elastomers. Chapter 1 also presents a summary of the economic incentive for these devices, specifically for Canadian mushroom harvesting, to emphasize the importance of this work. Existing mushroom harvesting systems use vacuum cup grippers. These frequently damage the target's delicate cap structure by applying forces over a narrow contact area. Chapter 2 provides a review of hyperelastic material theory as well as relevant literature in the field of soft robotic technology.

Chapter 3 details the design methodology and fabrication process used in the development of the compact single-DOF soft actuator, describing the key parameters used to evaluate the actuator's performance. This chapter includes the role and functionality of COMSOL Multiphysics nonlinear software in the generation of a soft PDMS actuator's 3D model. Chapter 4 focuses on the simulations performed on this model, chiefly on the deformation of the curved actuator's primary concave wall. The parameters described in the previous chapter were analyzed for their impact on the primary wall's deformation. Optimal parameter values were selected for the fabrication of three separate actuator variants, distinguishable by the thickness of their primary wall. Chapter 5 goes through the experiments performed on these actuators, followed by a comparison of the acquired results with simulated data. This chapter demonstrates the close match between some of the experiments performed with their corresponding simulations, with the furthest match within ± 1.11 mm.

Chapter 6 demonstrates the actuators' capabilities in a soft gripper assembly. From the controlled experiments, it was shown that increasing the thickness of the actuating wall allows the gripper to apply greater contact forces over a broader surface. Three tested wall thicknesses of 1.5 mm, 2 mm, and 2.5 mm at 34.47 kPa air pressure exhibited contact forces with the target object of 15.7 N, 18.4 N, and 19.3 N, respectively. In contrast, further slip testing showed that the thinnest tested wall exhibited almost double the payload capacity over the thickest. In the same order, for a cylindrical test object, the actuators show maximum payloads of 2.3 kg, 1.975 kg, and 1.375 kg. The grasp-and-hold capabilities of the proposed gripper were further assessed by performing a series of application tests involving organic mushrooms. These preliminary tests showed that the gripper, with the soft pneumatic actuators, performed better than conventional vacuum cup end-effectors and inflicted less surface damage on the target produce. These simulations and

experimental tests have enabled a number of key design guidelines to be summarized for the development of other types of similar pneumatic hyperelastic actuators and gripper assemblies.

7.2 Summary of Conclusions

This thesis explores the issues surrounding the development of compliant hyperelastic actuators for a pneumatic soft robotic gripper tailored for grasping delicate produce. Each single-chambered pneumatically-driven actuator has only one deformable wall that expands when inflated to make contact and then conform to the non-planar surface of the target object. Initial analysis is performed using COMSOL Multiphysics simulations which illustrate the impact of changing key geometrical parameters on the deformation of the primary concave wall. This work is supported with experimental tests that help confirm the predicted results.

In addition, the design and performance of a simple robotic gripper with three identical soft actuators assembled in a circular configuration was investigated. This design enabled the gripper to grasp and pick up round organic shapes, such as mushroom caps, without causing damage to the delicate surface. The design guidelines established in Chapter 6 of this thesis provide a method of adapting the proposed actuator and gripper designs for different applications.

The soft actuators presented in this thesis differ from existing work in several ways; primarily that they combine both computational modelling and experimental testing. The soft actuator design is compact and simple, deviating from conventional bending actuators with long multipart structures. This reduces or negates the impact of disturbances such as structure swaying or gravity. Besides being compatible with COMSOL Multiphysics' material library, the use of PDMS over more common ultra-soft materials also reduces sources of material instability such as snap-through buckling.

The PDMS actuator's simple and straightforward geometry make it widely applicable for compliant soft end-effectors capable of delicately grasping irregularly-shaped objects.

According to the requirements and constraints of the target application, the optimal geometry may be identified by the guidelines presented in Chapter 6 of this thesis, in order to design an effective soft pneumatic gripper for a wide variety of applications. Analysis through simulation reduces the need for extensive design iterations fabricated. In conclusion this thesis describes the successful design and hybrid analysis of a mechanically compliant soft robotic gripper capable of grasping delicate curved objects.

7.3 Recommendations for Future Research

The research performed in this thesis also shows the limitations of the current computational modelling approach. The hyperelastic material model used, the Mooney-Rivlin model, cannot accurately interpret an elastomer's behaviour at higher strains [23]. In order to further validate and improve the results of COMSOL Multiphysics simulations, it is necessary to implement a more comprehensive hyperelastic model capable of more accurately depicting the stress-strain relationship of hyperelastic materials at higher pressures. These more accurate models require additional data that can only be acquired through experimental testing of PDMS samples, the acquisition of which were beyond the scope and capabilities of this work. It is therefore recommended that future work on this topic starts with a focus on experimentally acquiring the additional data required for more detailed, and therefore more accurate, hyperelastic models.

In addition, COMSOL Multiphysics is capable of performing contact modelling between contacting geometries of different materials. However, these studies require material data on all geometries involved. In this case, this would include material data for *Agaricus Bisporus*. Future work for this specific gripper application could include material sampling of fresh mushrooms. Simulations could then be performed that study the interaction between the soft gripper and the delicate mushroom cap surface.

Additional future work could address some of the limitations of the gripper experiments performed, specifically that they were performed in a laboratory environment. By transitioning from a lab to a field environment, a more realistic assessment of the design's

CHAPTER 7. CONCLUDING REMARKS

performance can be made. Field tests would also benefit from the significantly larger sample size available on the mushroom growing bed.

Time and resources permitting, future work could also include verifying the durability and life cycle of the proposed actuator design. Appropriate experiments can take days, if not weeks, to perform, and require a secure environment free of disturbances. This was beyond the scope and capabilities of this work.

Bibliography

- [1] L. Wang, S. G. Nurzaman, and F. Iida, “Soft-Material Robotics,” *Found. Trends Robot.*, vol. 5, no. 3, pp. 191–259, 2017.
- [2] D. Rus and M. T. Tolley, “Design, fabrication and control of soft robots,” *Nature*, vol. 521, no. 7553, pp. 467–475, May 2015.
- [3] J. Shintake, V. Cacucciolo, D. Floreano, and H. Shea, “Soft Robotic Grippers,” *Adv. Mater.*, vol. 30, no. 29, pp. 1–33, Jul. 2018.
- [4] B. Mosadegh *et al.*, “Pneumatic Networks for Soft Robotics that Actuate Rapidly,” *Adv. Funct. Mater.*, vol. 24, no. 15, pp. 2163–2170, Apr. 2014.
- [5] R. F. Shepherd *et al.*, “Multigait soft robot,” *Proc. Natl. Acad. Sci.*, vol. 108, no. 51, pp. 20400–20403, Dec. 2011.
- [6] F. Ilievski, A. D. Mazzeo, R. F. Shepherd, X. Chen, and G. M. Whitesides, “Soft Robotics for Chemists,” *Angew. Chemie Int. Ed.*, vol. 50, no. 8, pp. 1890–1895, Feb. 2011.
- [7] B. Mosadegh *et al.*, “Pneumatic Networks for Soft Robotics that Actuate Rapidly - Supporting Information,” *Adv. Funct. Mater.*, vol. 24, no. 15, pp. 2163–2170, Apr. 2014.
- [8] Vineland Research and Innovation Centre Inc., “An Automation Technology Strategy for the Canadian Horticulture Sector,” Vineland Station, ON, 2017.
- [9] E. A. Laate, “The Economics of Production and Marketing of Greenhouse Crops in Alberta,” Edmonton, 2013.
- [10] C. Wouter Bac, E. J. van Henten, J. Hemming, and Y. Edan, “Harvesting Robots for High-value Crops: State-of-the-art Review and Challenges Ahead,” *J. F. Robot.*, vol. 31, no. 6, pp. 888–911, Nov. 2014.
- [11] C. Parisses and E. Marinis, “Design of an autonomous robotic vehicle and development of a suitable gripper for harvesting sensitive agricultural products,” in *International Conference on Information and Communication Technologies for Sustainable Agri-production and Environment*, 2011, no. 8–11, pp. 339–349.
- [12] G. C. Wheeler and T. A. Russell, “Suction Cup Assemblies,” 5 491 965, 1996.
- [13] T. A. Russel and G. C. Wheeler, “Mushroom Harvesting,” 5 185 989, 1993.
- [14] J. H. Rowley, “Developing flexible automation for mushroom harvesting (*Agaricus bisporus*),” University of Warwick, 2009.

BIBLIOGRAPHY

- [15] N. A. Kuchinskiy, "Development of an Autonomous Robotic Mushroom Harvester," Western University, 2016.
- [16] J. N. Reed, S. J. Miles, J. Butler, M. Baldwin, and R. Noble, "Automatic Mushroom Harvester Development," *J. Agric. Eng. Res.*, vol. 78, no. 1, pp. 15–23, Jan. 2001.
- [17] T. Rapila, J. Kantola, and T. Rapila, "Apparatus for Picking Mushrooms," 8,033,087, 2011.
- [18] G. C. Wheeler, B. Vale, and T. Hill, "Harvesting of Delicate Produce," 5,058,368, 1991.
- [19] J. Van De Vegte, J. Renfrew, M. Jandrisits, and R. Lau, "Mushroom Harvester," WO 2016/029299 A1, 2016.
- [20] A. Azoyan, "Feasibility analysis of an automated mushroom harvesting sytem," University of Georgia, 2004.
- [21] J. J. J. Janssen, J. J. H. van Nunen, and M. M. J. L. Giebels, "Device for the automatic selecive harvesting of mushrooms," 5,471,827, 1995.
- [22] J. Van De Vegte, M. Lawson, J. Renfrew, and M. Koshy, "Graze Harvesting of Mushrooms," US 2017/0042095 A1, 2017.
- [23] M. Shahzad, A. Kamran, M. Z. Siddiqui, and M. Farhan, "Mechanical Characterization and FE Modelling of a Hyperelastic Material," *Mater. Res.*, vol. 18, no. 5, pp. 918–924, Oct. 2015.
- [24] A. F. Bower, "Hyperelasticity- time independent behavior of rubbers and foams subjected to large strains," in *Applied Mechanics of Solids*, Taylor & Francis, 2014, pp. 1–19.
- [25] S. Karimi, "Three Dimensional Numerical Simulation, Design and Structural Optimization of Pneumatically Actuated Cell Stretching Device," Tampere University of Technology, 2015.
- [26] R. Jakel, "Analysis of Hyperelastic Materials with MECHANICA - Theory and Application Examples," *2nd SaxSIM Tech. Univ. Chemnitz*, no. 1, 2010.
- [27] G. A. Holzapfel, "Some Forms of Strain-energy Functions," in *Nonlinear Solid Mechanics: A Continuum Approach For Engineering*, 1st ed., John Wiley & Sons, LTD, 2010, p. 238.
- [28] E. Omid, "Characterization and Assessment of Mechanical Properties of Adipose Derived Breast Tissue Scaffolds as a Means for Breast Reconstructive Purposes," Western University, 2014.
- [29] H. Mehrabian, G. Campbell, and A. Samani, "A constrained reconstruction

BIBLIOGRAPHY

- technique of hyperelasticity parameters for breast cancer assessment,” *Phys. Med. Biol.*, vol. 55, no. 24, pp. 7489–7508, Dec. 2010.
- [30] R. C. Hibbeler, “Strain Energy,” in *Mechanics of Materials*, 9th ed., Pearson Higher Education Inc., 2011, p. 96.
 - [31] M. Mooney, “A Theory of Large Elastic Deformation,” *J. Appl. Phys.*, vol. 11, no. 9, pp. 582–592, Sep. 1940.
 - [32] L. Anand, “Moderate deformations in extension-torsion of incompressible isotropic elastic materials,” *J. Mech. Phys. Solids*, vol. 34, no. 3, pp. 293–304, Jan. 1986.
 - [33] G. Miron, B. Bédard, and J.-S. Plante, “Sleeved Bending Actuators for Soft Grippers: A Durable Solution for High Force-to-Weight Applications,” *Actuators*, vol. 7, no. 3, p. 40, Jul. 2018.
 - [34] N. F. H. Muhamad, W. N. Z. W. Zainon, S. Kormin, N. Akhir, and M. S. Ali, “Snap-Through Buckling Problem of Spherical Shell Structure,” *Int. J. Sci. Eng.*, vol. 8, no. 1, pp. 54–59, 2015.
 - [35] G. Mao, T. Li, Z. Zou, S. Qu, and M. Shi, “Prestretch effect on snap-through instability of short-length tubular elastomeric balloons under inflation,” *Int. J. Solids Struct.*, vol. 51, no. 11–12, pp. 2109–2115, Jun. 2014.
 - [36] J. T. B. Overvelde, T. Klok, J. J. A. D’haen, and K. Bertoldi, “Amplifying the response of soft actuators by harnessing snap-through instabilities,” *Proc. Natl. Acad. Sci.*, vol. 112, no. 35, pp. 10863–10868, Sep. 2015.
 - [37] J. Friend and L. Yeo, “Fabrication of microfluidic devices using polydimethylsiloxane,” *Biomicrofluidics*, vol. 4, no. 2, p. 026502, Jun. 2010.
 - [38] T. Fujii, “PDMS-based microfluidic devices for biomedical applications,” *Microelectron. Eng.*, vol. 61–62, pp. 907–914, Jul. 2002.
 - [39] “Polydimethylsiloxane Safety Data Sheet.” SIGMA-ALDRICH, pp. 1–6, 2018.
 - [40] T. K. Kim, J. K. Kim, and O. C. Jeong, “Measurement of nonlinear mechanical properties of PDMS elastomer,” *Microelectron. Eng.*, vol. 88, no. 8, pp. 1982–1985, Aug. 2011.
 - [41] I. D. Johnston, D. K. McCluskey, C. K. L. Tan, and M. C. Tracey, “Mechanical characterization of bulk Sylgard 184 for microfluidics and microengineering,” *J. Micromechanics Microengineering*, vol. 24, no. 3, p. 035017, Mar. 2014.
 - [42] M. Liu, J. Sun, and Q. Chen, “Influences of heating temperature on mechanical properties of polydimethylsiloxane,” *Sensors Actuators A Phys.*, vol. 151, no. 1, pp. 42–45, Apr. 2009.

BIBLIOGRAPHY

- [43] J. C. McDonald and G. M. Whitesides, "Poly(dimethylsiloxane) as a Material for Fabricating Microfluidic Devices," *Acc. Chem. Res.*, vol. 35, no. 7, pp. 491–499, Jul. 2002.
- [44] "RTV615 Technical Data Sheet," vol. HCD-10333. MOMENTIVE, pp. 1–6, 2012.
- [45] R. Green, "Fabrication of Large Mechanically Flexible Multi-Layered PDMS Optical Devices," The University of Western Ontario, 2016.
- [46] F. M. White, "Buoyancy and Stability," in *Fluid Mechanics*, 7th ed., New York: McGraw-Hill, 2011, pp. 92–93.
- [47] M. Wehner *et al.*, "An integrated design and fabrication strategy for entirely soft, autonomous robots," *Nature*, vol. 536, no. 7617, pp. 451–455, 2016.
- [48] R. V. Martinez, C. R. Fish, X. Chen, and G. M. Whitesides, "Elastomeric Origami: Programmable Paper-Elastomer Composites as Pneumatic Actuators," *Adv. Funct. Mater.*, vol. 22, no. 7, pp. 1376–1384, Apr. 2012.
- [49] W. Chen, R. H. W. Lam, and J. Fu, "Photolithographic surface micromachining of polydimethylsiloxane (PDMS)," *Lab Chip*, vol. 12, no. 2, pp. 391–395, 2012.
- [50] C. Con and B. Cui, "Effect of mold treatment by solvent on PDMS molding into nanoholes," *Nanoscale Res. Lett.*, vol. 8, no. 1, p. 394, Dec. 2013.
- [51] M. Zhang, J. Wu, L. Wang, K. Xiao, and W. Wen, "A simple method for fabricating multi-layer PDMS structures for 3D microfluidic chips," *Lab Chip*, vol. 10, no. 9, p. 1199, 2010.
- [52] D. A. Chang-Yen, R. K. Eich, and B. K. Gale, "A monolithic PDMS waveguide system fabricated using soft-lithography techniques," *J. Light. Technol.*, vol. 23, no. 6, pp. 2088–2093, Jun. 2005.
- [53] M. A. Eddings, M. A. Johnson, and B. K. Gale, "Determining the optimal PDMS–PDMS bonding technique for microfluidic devices," *J. Micromechanics Microengineering*, vol. 18, no. 6, p. 067001, Jun. 2008.
- [54] J. F. Wilson and U. Mahajan, "The Mechanics and Positioning of Highly Flexible Manipulator Limbs," *J. Mech. Transm. Autom. Des.*, vol. 111, no. 2, p. 232, 1989.
- [55] K. Suzumori, S. Iikura, and H. Tanaka, "Development of flexible microactuator and its applications to robotic mechanisms," in *Proceedings. 1991 IEEE International Conference on Robotics and Automation*, 1991, pp. 1622–1627.
- [56] K. Suzumori, S. Iikura, and H. Tanaka, "Flexible microactuator for miniature robots," in *[1991] Proceedings. IEEE Micro Electro Mechanical Systems*, 1991, pp. 204–209.
- [57] L. Wang and F. Iida, "Deformation in Soft-Matter Robotics: A Categorization and

BIBLIOGRAPHY

- Quantitative Characterization,” *IEEE Robot. Autom. Mag.*, vol. 22, no. 3, pp. 125–139, Sep. 2015.
- [58] Y. Hao *et al.*, “Universal soft pneumatic robotic gripper with variable effective length,” in *2016 35th Chinese Control Conference (CCC)*, 2016, vol. 35, pp. 6109–6114.
- [59] P. Polygerinos *et al.*, “Towards a soft pneumatic glove for hand rehabilitation,” in *IEEE International Conference on Intelligent Robots and Systems*, 2013, pp. 1512–1517.
- [60] S. R. Toolkit, “Textile-Silicone Hybrid Sensor - An Educator’s Guide.” 2017.
- [61] S. R. Toolkit, “Soft Gripper - An Educator’s Guide.” 2017.
- [62] P. Polygerinos, B. Mosadegh, and A. Camp, “Soft robotics toolkit - Fabrication,” [Http://Softroboticstoolkit.Com/](http://Softroboticstoolkit.Com/). [Online]. Available: <https://softroboticstoolkit.com/book/pneunets-fabrication>.
- [63] K. C. Galloway, P. Polygerinos, C. J. Walsh, and R. J. Wood, “Mechanically programmable bend radius for fiber-reinforced soft actuators,” in *2013 16th International Conference on Advanced Robotics (ICAR)*, 2013, pp. 1–6.
- [64] J. Baer, “Material Handling Apparatus and the Like,” 3343864, 1967.
- [65] F. Daerden and D. Lefeber, “Pneumatic artificial muscles: actuators for robotics and automation,” *Eur. J. Mech. Environ. Eng.*, vol. 47, no. 1, pp. 11–21, 2002.
- [66] H. Al-Fahaam, S. Davis, and S. Nefti-Meziani, “The design and mathematical modelling of novel extensor bending pneumatic artificial muscles (EBPAMs) for soft exoskeletons,” *Rob. Auton. Syst.*, vol. 99, pp. 63–74, Jan. 2018.
- [67] B. Tondu, “Modelling of the McKibben artificial muscle: A review,” *J. Intell. Mater. Syst. Struct.*, vol. 23, no. 3, pp. 225–253, Feb. 2012.
- [68] D. Trivedi, A. Lotfi, and C. D. Rahn, “Geometrically exact dynamic models for soft robotic manipulators,” in *2007 IEEE/RSJ International Conference on Intelligent Robots and Systems*, 2007, vol. 24, no. 4, pp. 1497–1502.
- [69] D. Trivedi, D. Dienno, and C. D. Rahn, “Optimal, Model-Based Design of Soft Robotic Manipulators,” *J. Mech. Des.*, vol. 130, no. 9, p. 091402, 2008.
- [70] K. C. Galloway *et al.*, “Soft Robotic Grippers for Biological Sampling on Deep Reefs,” *Soft Robot.*, vol. 3, no. 1, pp. 23–33, Mar. 2016.
- [71] C. Multiphysics, *Introduction to COMSOL Multiphysics 5.3*. COMSOL Multiphysics, 2017.
- [72] Ascension Technology Corporation, “3D Guidance TrakSTAR User Guide,” no. 2.

BIBLIOGRAPHY

- Northern Digital Inc., Waterloo, Ontario, 2014.
- [73] N. D. Tillett, "Robotic Manipulators in Horticulture: A Review," *J. Agric. Eng. Res.*, vol. 55, no. 2, pp. 89–105, Jun. 1993.
- [74] "Bellows Suction Pads FG PVS (2.5 Folds)." Schmalz Vacuum Technology Ltd., Mississauga, ON, pp. 202–205.
- [75] "Bell suction cup (round)." Schmalz Vacuum Technology Ltd., Mississauga, ON, pp. 1–3, 2017.
- [76] "Mushrooms Canada," *The Canadian Business Journal*, 2015. [Online]. Available: <http://www.cbj.ca/mushrooms-canada/>. [Accessed: 18-Jan-2018].
- [77] J. Van Leeuwen and H. J. Wichers, "Tyrosinase activity and isoform composition in separate tissues during development of *Agaricus bisporus* fruit bodies," *Mycol. Res.*, vol. 103, no. 4, pp. 413–418, Apr. 1999.
- [78] A. Weijn, "Unravelling the bruising-discoloration of *Agaricus bisporus*, the button mushroom," Wageningen University, 2013.
- [79] J. B. W. HAMMOND and R. NICHOLS, "Carbohydrate Metabolism in *Agaricus bisporus* (Lange) Sing.: Changes in Soluble Carbohydrates during Growth of Mycelium and Sporophore," *J. Gen. Microbiol.*, vol. 93, no. 2, pp. 309–320, Apr. 1976.
- [80] "The PreciseFlex 400 Robot Hardware Reference Manual." Precise Automation Inc., Los Altos, California, pp. 1–132, 2016.
- [81] "Basic ejector SBP 20 G03 SDA." Schmalz Vacuum Technology Ltd., Mississauga, ON, pp. 1–4, 2017.
- [82] "Operating Principles of Vacuum Generation - Venturi Principle," *SCHMALZ*. [Online]. Available: <https://www.schmalz.com/en/vacuum-knowledge/basic-knowledge/operating-principles-of-vacuum-generation/>.
- [83] A. McGarry and K. S. Burton, "Mechanical properties of the mushroom, *Agaricus bisporus*," *Mycol. Res.*, vol. 98, no. 2, pp. 241–245, Feb. 1994.

Appendix A

PneuNet Actuators

Pneumatic networks, or PneuNets are a series of chambers and channels embedded within an extensible elastomer layer. This layer is bonded to a flat inextensible layer. A single pressure source inflates the top layer's chambers, which creates a strain difference between the extensible and inextensible layers. This creates a bending motion [4]. A series of PneuNet actuators were fabricated at Western University. Standard PneuNet actuators were fabricated in collaboration with the MME 4499 Undergraduate Design Project group, led by Marcus Dottermann. Under the supervision of Dr. George Knopf, the author of this graduate research thesis provided consultation on soft robotic technology, fabrication methods, and 3D printed mould design. In that capacity, the author fabricated a number of PneuNet actuators to demonstrate proper fabrication techniques to the undergraduate design team. These actuators were kept, and tests were attempted for the purposes of this thesis.

Each PneuNet actuator is fabricated using methods as described by the Harvard Biodesign Lab website Soft Robotics Toolkit [62]. Acrylonitrile butadiene styrene (ABS) moulds were created using a 3D printed based on SolidWorks models. Each mould was cast with EcoFlex 00-30. A narrow strip of synthetic fiber mesh was placed in the bottom-most mould halfway through casting to create the inextensible layer. Each actuator is 11.5 cm in length, with chambers 2 cm tall. Deforming inner walls are 3 mm in thickness.

APPENDIX A. PNEUNET ACTUATORS

At low pressures and brief actuation times, the PneuNets performed as shown in Figure A.1. However, high input pressures or actuation for any significant period of time resulted in unstable and unpredictable behaviour. Tests were ultimately not performed due to these instabilities. The excessive compliance of the ultra-soft Ecoflex also rendered the associated gripper unable to grasp any object. A series of attempts at actuation and grasping is illustrated in Figures A.2–A.6.

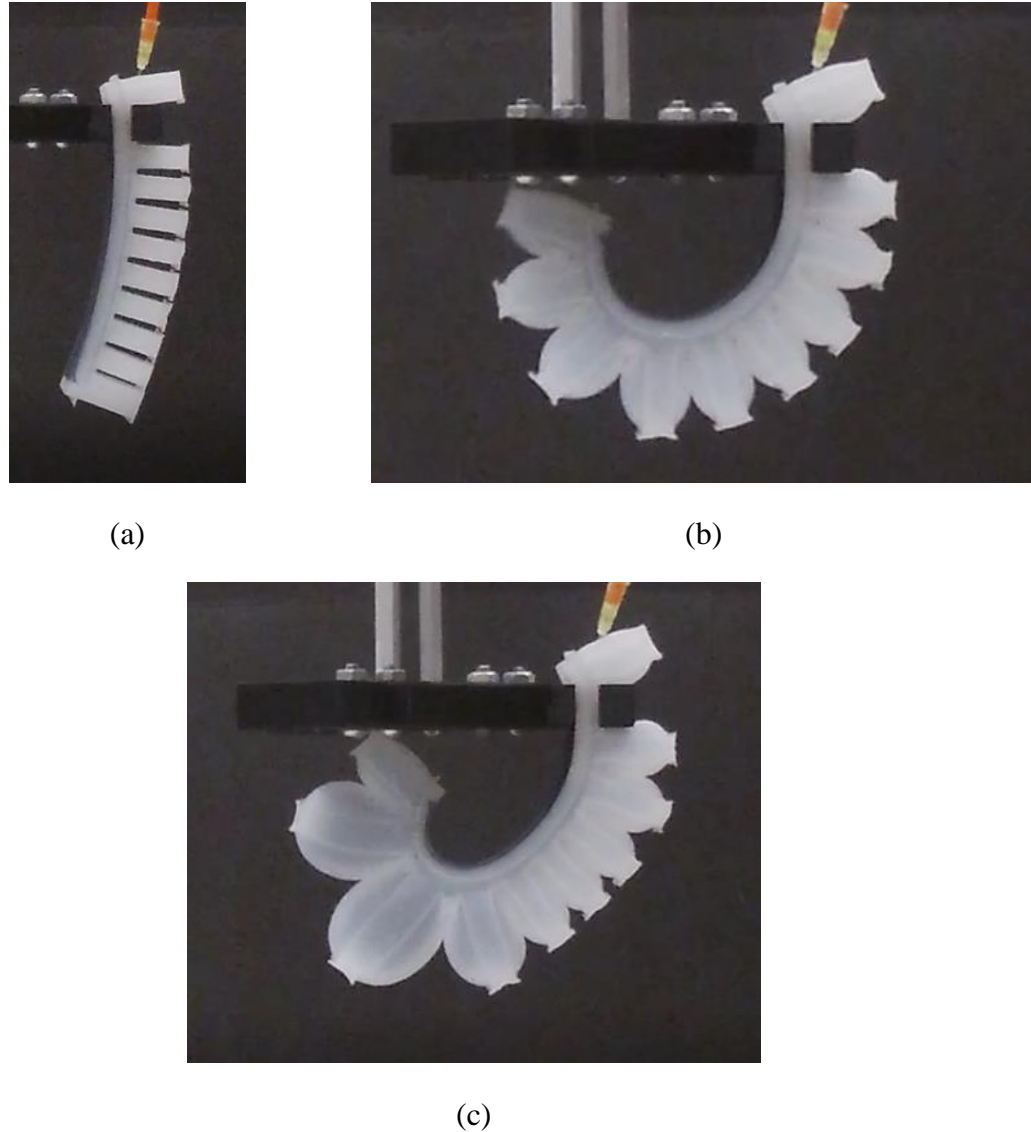
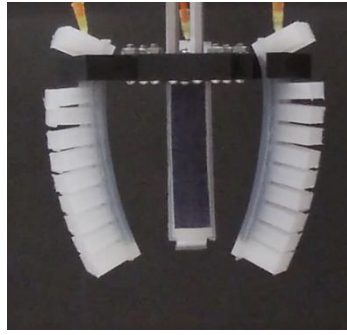
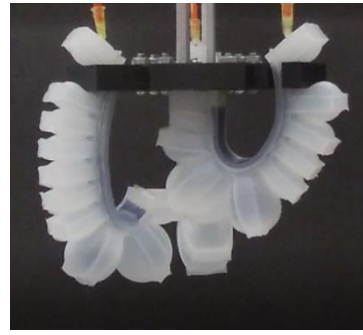


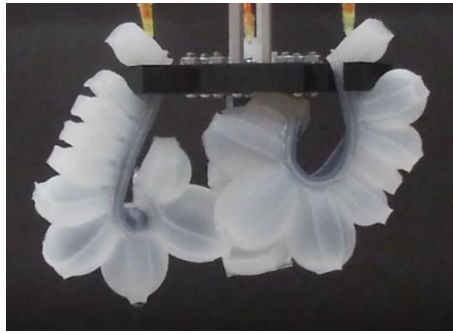
Figure A.1 PneuNet Actuator. (a) At rest; (b) Full Actuation; (c) Observed Instability due to ultra-soft hyperelastic Ecoflex 00-30.



(a)

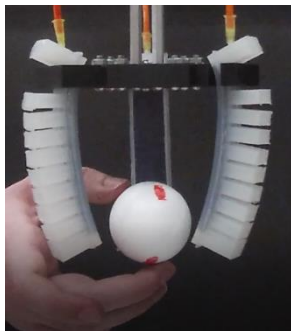


(b)

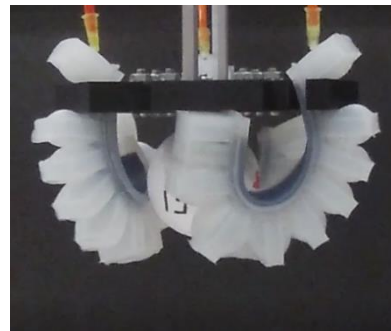


(c)

Figure A.2 PneuNet Gripper. (a) At rest; (b) and (c) show two separate instances of snap-through instability.



(a)



(b)

Figure A.3 Grasping attempt with 4 cm diameter foam sphere. (a) Positioning the sphere between the PneuNet actuators; (b) PneuNet gripper failing to properly hold 4 cm diameter foam sphere by its fingertips.

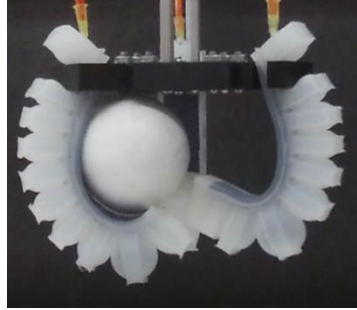
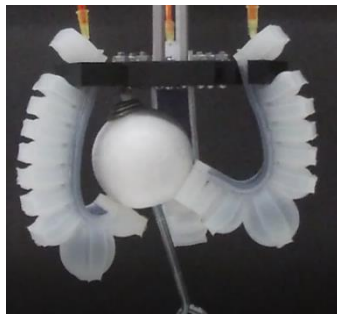
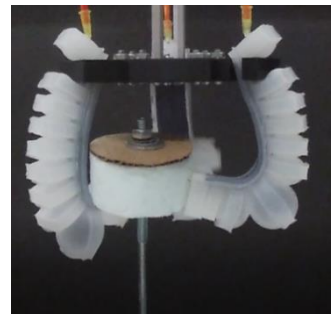


Figure A.4 PneuNet gripper failing to properly hold 6 cm diameter foam sphere by its fingertips.

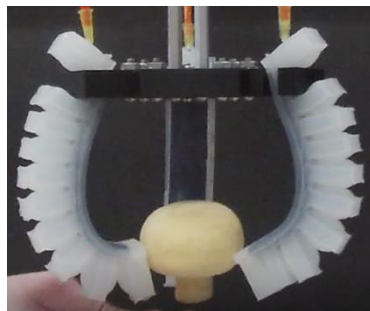


(a)

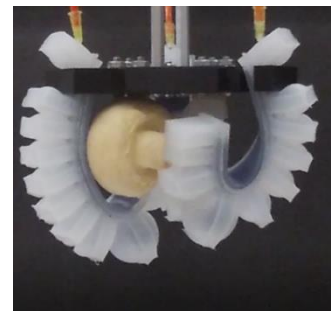


(b)

Figure A.5 PneuNet gripper failing to properly hold the (a) spherical and (b) cylindrical payload rigs by its fingertips.



(a)



(b)

Figure A.6 PneuNet gripper attempting to grasp a soft foam mushroom. (a) Initially succeeding but (b) eventually failing to grasp by its fingertips.

Appendix B

Vacuum Cups

A vacuum cup does not function by attaching itself to an object's surface. It is instead pressed against the surface by the internal application of a vacuum pressure. This is achieved when the internal pressure between the cup and the surface is lower than the external ambient pressure (Figure B.1).

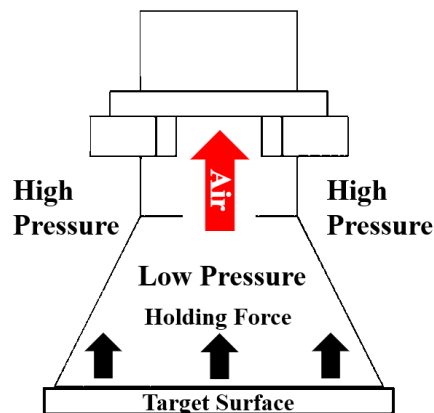
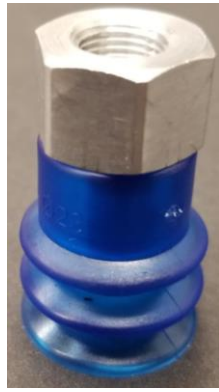


Figure B.1 Sketch of vacuum cup operating principle.

Members of Vineland Research and Innovation Centre Inc. have graciously provided two standard vacuum cups currently used for mushroom harvesting operations. These are the common bellows-type (Figure B.2a) and bell-type (Figure B.3b) cups previously shown in Section 6.1.2. The bell-type vacuum cup is used as a basis for the development of three

APPENDIX B. VACUUM CUPS

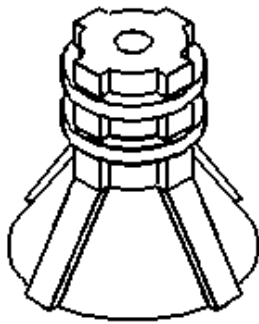
vacuum cup iterations, labelled as Cup Iterations 1, 2, and 3. In each case, the cup has a height of 35 mm and a bottom diameter of 30 mm. Iteration 1 (B.2c) has structural beams running along the side of the cup structure and rings around the cup neck. These additions are intended to fortify the cup's structure to allow fabrication with ultra-soft elastomers like Ecoflex 00-30. The base of the cup has a wall thickness of 2 mm. Iteration 2 (B.2d) has a thicker cup neck, and the base thickness is reduced from 2 mm to 1 mm. Iteration 3 (B.2e) reduces the width of the structural beams and increases their number from 4 to 12. The base thickness is further reduced to 0.5 mm. To investigate the merit of changing material flexibility, each of the three vacuum cup iterations are fabricated with both PDMS and Ecoflex 00-30.



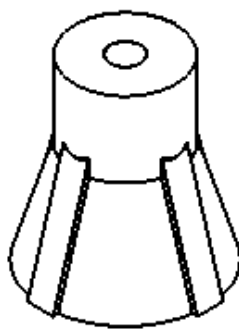
(a)



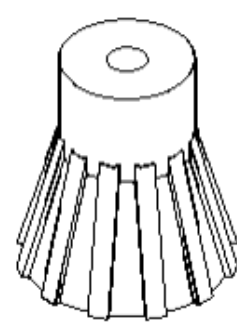
(b)



(c)



(d)



(e)

Figure B.2 Vacuum cup geometries tested. (a) Bellows-type cup; (b) Bell-type cup; (c) Cup Iteration 1; (d) Cup Iteration 2; (e) Cup Iteration 3.

APPENDIX B. VACUUM CUPS

Grasping tests use the same evaluation parameters as described in Section 6.2, and the identical conditions to test results presented in Section 6.3. Performance data for the vacuum cup gripper geometries, including commercial and custom structures, are shown in Figure B.3. Overall, the custom geometries do significantly improve grasping success. Observable cap surface damage is still present in every case. Using the softer Ecoflex 00-30 does reduce damage inflicted to the cap structure to some extent for each custom geometry, however damage is not fully eliminated.

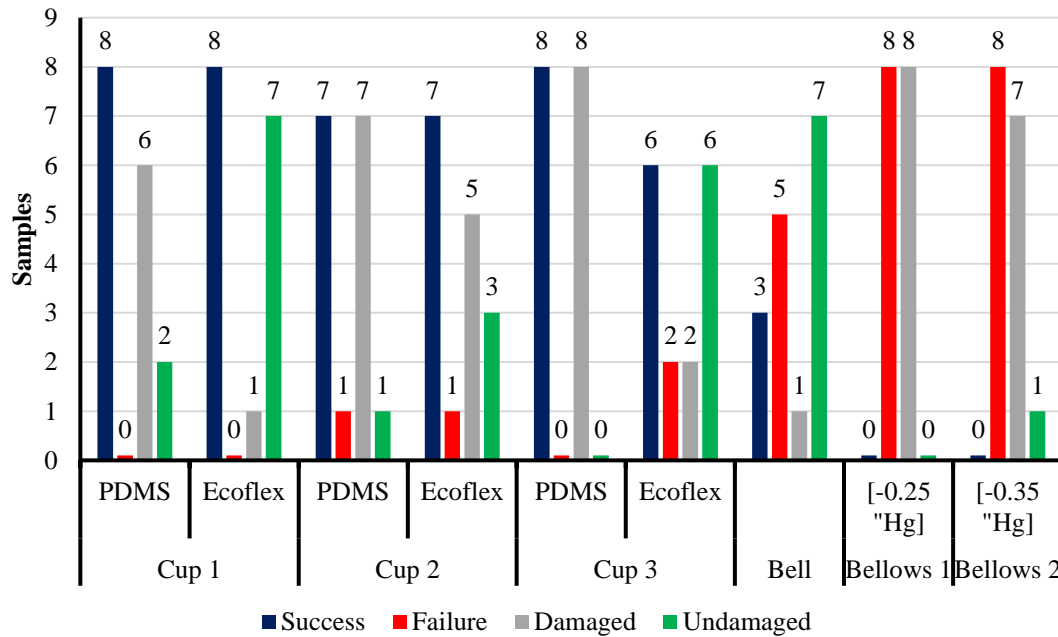


Figure B.3 Results of grasp-and-hold experiments (success/failure) and observed damage to mushroom surfaces during the tests (damaged/undamaged). These results are for tests with all vacuum cups.

Appendix C

Supporting Information on Mushrooms

C.1 The White Mushroom, *Agaricus Bisporus*

Of the thousands of edible mushrooms, only about 20 are grown on an industrial scale. The most commercially popular species of mushroom is the white or button mushroom, *Agaricus Bisporus*, making up 90% of the total mushroom crop in Canada [76]. A mushroom's basic anatomy is shown in Figure C.1.

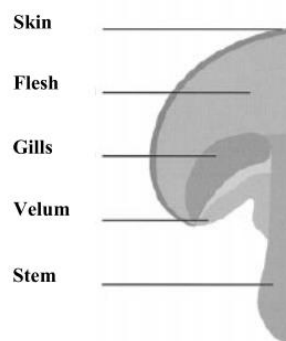


Figure C.1 Basic anatomy of a mushroom (Leeuwen et al. [77], © 1999 Elsevier, included with permission).

APPENDIX C. SUPPORTING INFORMATION ON MUSHROOMS

Variants of *Agaricus Bisporus* are distinguishable by their level of development, which are categorized into 7 stages [78]. Cap geometries undergo significant changes in diameter and shape throughout the mushroom's growth. Early-to-mid stage variants all have a round cap, whereas the final stage of development has a flat cap surface. Development stages are shown in Figure C.2 and described in Table C.1.

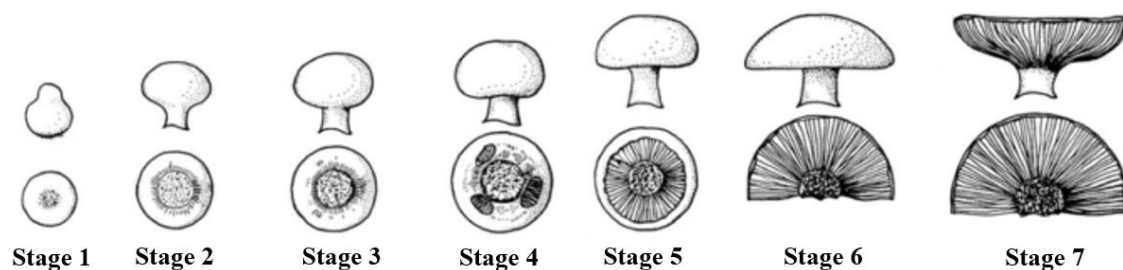


Figure C.2 Development stages of *Agaricus Bisporus* in terms of growth (Hammond et al. [79], © 1976 Journal of General Microbiology, included with permission).

Table C.1 Development stages of *Agaricus Bisporus* in terms of mushroom cap diameter ranges. Adapted from [78].

Stage	Description	Cap Diameter
1	Pinhead, characterized by undifferentiated velum	< 5 mm
2	Button, characterized by visible and intact (but not stretched) velum	20-30mm
3	Closed cup, velum is stretched but still intact	30-40mm
4	Cup, velum starting to tear	30-40mm
5	Cup, velum torn, cap still cup shaped, gills clearly visible	30-50mm
6	Flat, gill surface flat or slightly concave	40-60mm
7	Flat, gill surface curving upwards	50-70mm

Mushroom bed positioning follows the conventional Dutch Shelving organizational structure [22]. There is approximately 30 *cm* between the growing bed stacks.

C.2 Graze Harvesting Strategy

Graze harvesting involves the strategic collection of produce to maximize crop yield. For mushrooms, graze harvesting is more sophisticated than simply collecting the largest mushrooms from the soil bed. It requires the identification and harvesting of smaller mushrooms, making room for the adjacent fungi to grow to their optimal size. This pre-emptive harvest is known as separation [22]. Mushroom graze harvesting must also consider the varying maturities of the growth flushes within the growing bed. Harvesting the appropriate generation of fungi ensures that the bed consistently holds mushrooms ready to be picked throughout the entire harvesting process. This maturity-based selection process is known as staggering [22]. Controlling both separation and stagger is critical for efficiently and consistently harvesting a mushroom bed.

Another research team at Vineland is developing an identification system for graze harvesting, the details of which are proprietary. As such, this research thesis focuses solely on the end-effector, and no identification methods shall be discussed.

C.3 Overview of Existing Infrastructure at Vineland Research and Innovation Centre Inc.

Parts of this research are in collaboration with the Vineland Research and Innovation Centre (Vineland). They have a testing facility that approximates the working environment common for mushroom harvesting. This includes a robotic manipulator upon which the proposed soft gripper design would be attached.

Vineland has graciously provided a reference manual for a version of this robotic system, the PreciseFlex400 [80]. The four-axis robotic system includes a 48 VDC motor power supply and a 24 VDC logic power supply located in the manipulator's base. A

kinematic diagram of the manipulator is shown in Figure C.3. The diagram outlines the manipulator components as named in the reference manual. Note that Vineland has replaced the original end-effector with a vacuum cup mounted on an aluminum plate. An embedded pneumatic system provides up to 75 psi of air pressure to a compact Venturi vacuum ejector fixed to this mounting plate. This ejector converts the compressed (plenum) air pressure into vacuum pressure. Vineland has loaned a similar ejector [81] for work on Western University campus.

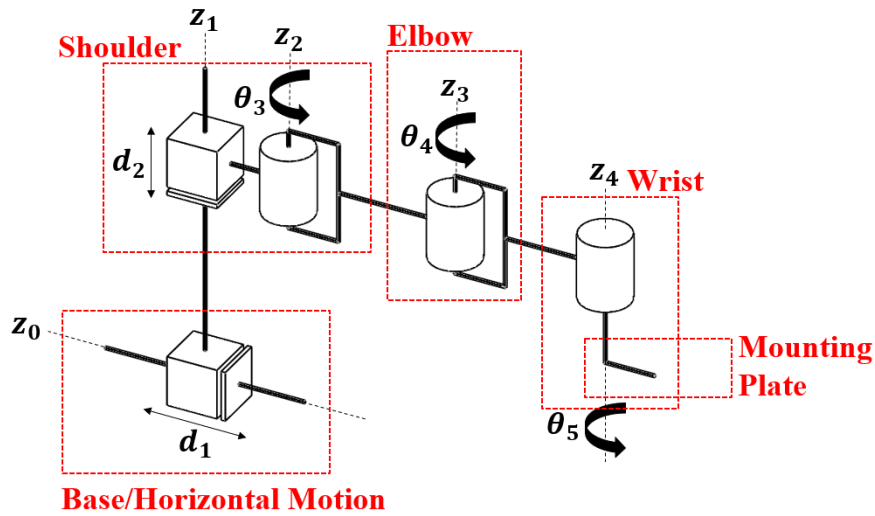


Figure C.3 Kinematic diagram of PreciseFlex robotic manipulator in use at the Vineland facility. Adapted from PreciseFlex reference manual [80].

The vacuum-generating ejector's principle of operation is based on the Venturi principle [82] (Figure C.4). Compressed air is introduced into the ejector (A). It is directed through a tapered section known as the motive or Venturi nozzle (B). Due to the reduced cross-section of this segment, the compressed air is accelerated. The dynamic pressure increases, while the static air pressure simultaneously decreases. Once it has passed the motive nozzle, the accelerated air expands and leaves a void. This void must be filled, and thus a vacuum is generated. Air is drawn through the vacuum connection (D) into the ejector. The ejector that Vineland provided for lab testing includes a silencer to reduce

sound (C). The compressed air, along with the drawn-in vacuum air, both escape through this component.

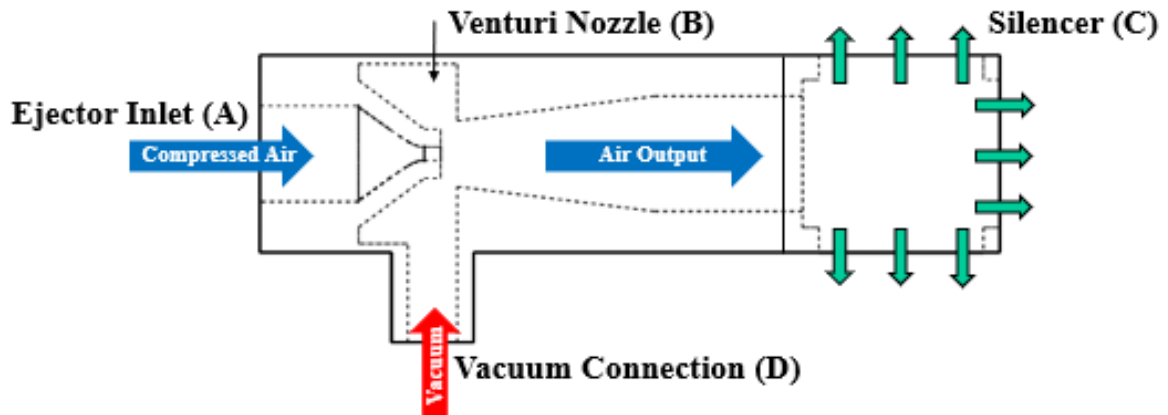


Figure C.4 Operating principle of Venturi vacuum ejector. (A) Ejector inlet; (B) Venturi nozzle; (C) Sound-reducing silencer; (D) Vacuum connection. As described by the SCHMALZ webpage [82].

The manipulator is fixed to a horizontal track as shown in Figure C.3. Along with the vertical column to which the shoulder is connected, this allows the system to travel along the rows and columns that make up the stacked mushroom growing beds. The referenced hardware manual lists the original gripper's payload as up to 500 g [80]. However, it is important to note that this payload value is for the specific gripper and not the whole manipulator system. In addition, the provided manual is for an older version of the manipulator. Sources at Vineland responsible for purchasing the manipulator state the modern version they purchased has a manipulator payload of up to 3 kg.

C.4 Mushroom Sample Measurements

As mentioned in Appendix C.1, *Agaricus Bisporus* grows through 7 distinguishable stages of development, during which the cap geometries can change drastically. To accelerate the design process and reduce costs incurred from purchasing multiple sizes of

APPENDIX C. SUPPORTING INFORMATION ON MUSHROOMS

test mushrooms, the size class was reduced to a small range of cap diameters. Mushrooms were purchased from a local grocery store ($n = 8$ mushroom) to acquire consistent testing dimensions. Both external and cross-sectional measurements were taken. Measurement data can be found in Table C.2. Cap diameters and physical appearance approximate these samples to the 5th stage of development.

Though masses are recorded, it is important to note that the purchased mushrooms have a cut stem, meaning that a portion of their true mass is missing. Measurements were also taken two days after purchase. They were stored at 35 °F, the standard refrigerator temperature. Though they were left at ambient temperature for 2 hours before being measured and weighed, the storage time does affect the mushroom's moisture content and therefore its mass [83]. As a result, the mass values shown may not be an accurate representation of a whole and embedded mushroom. Figure C.6 illustrates the measurements taken of the mushroom samples. Figure C.7 presents the sample group for $n = 8$ mushrooms.

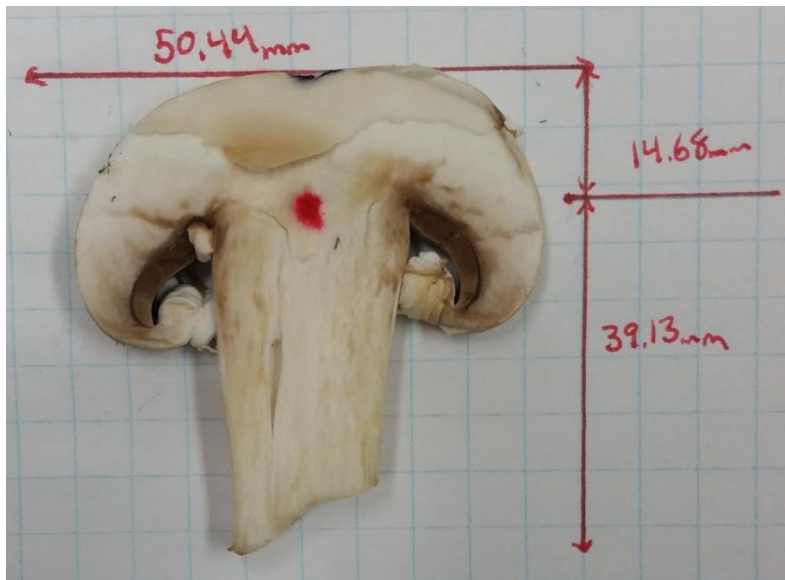
Summary of mushroom sizes and experimental parameters.

- Sample Size ($n = 8$)
- Mushrooms Purchased on: 2018/07/08
- Measurements taken on: 2018/07/10
- Mass Measurements taken with: Mettler Toledo ME204E (max = 220 g, d = 0.0001 g)
- Stored in refrigerator at: $T = 35$ °F (1.6 °C)
- Cross-sections of mushroom middle cut of approx. 5 mm thickness

APPENDIX C. SUPPORTING INFORMATION ON MUSHROOMS

Table C.2 Summary of mushroom sample measurements.

Mushroom	Cap [mm]			Stem (Cut) [mm]		Whole Specimen	
	Diameter	Height	Radius of Curvature	Diameter (Thickness)	Height	Mass [g]	Height [mm]
1	50.44	29.15	14.68	17.75	39.13	26.67	49.82
2	52.28	28.76	14.24	19.21	33.37	23.46	46.70
3	51.62	28.43	15.21	19.59	28.80	29.06	46.32
4	54.64	27.59	14.86	18.61	37.11	31.19	52.42
5	57.16	29.08	15.76	19.86	43.17	34.69	59.81
6	56.20	30.50	14.71	17.92	37.93	35.56	56.81
7	48.57	27.23	12.16	18.49	35.73	25.66	49.23
8	49.53	27.14	14.19	18.17	31.52	23.92	49.46
Average	52.56	28.49	14.48	18.70	35.85	28.78	51.32



(a)



(b)

Figure C.5 Mushroom sample measurements. (a) Cross-section dimensions; (b) Mass measurements with Mettler Toledo digital scale.

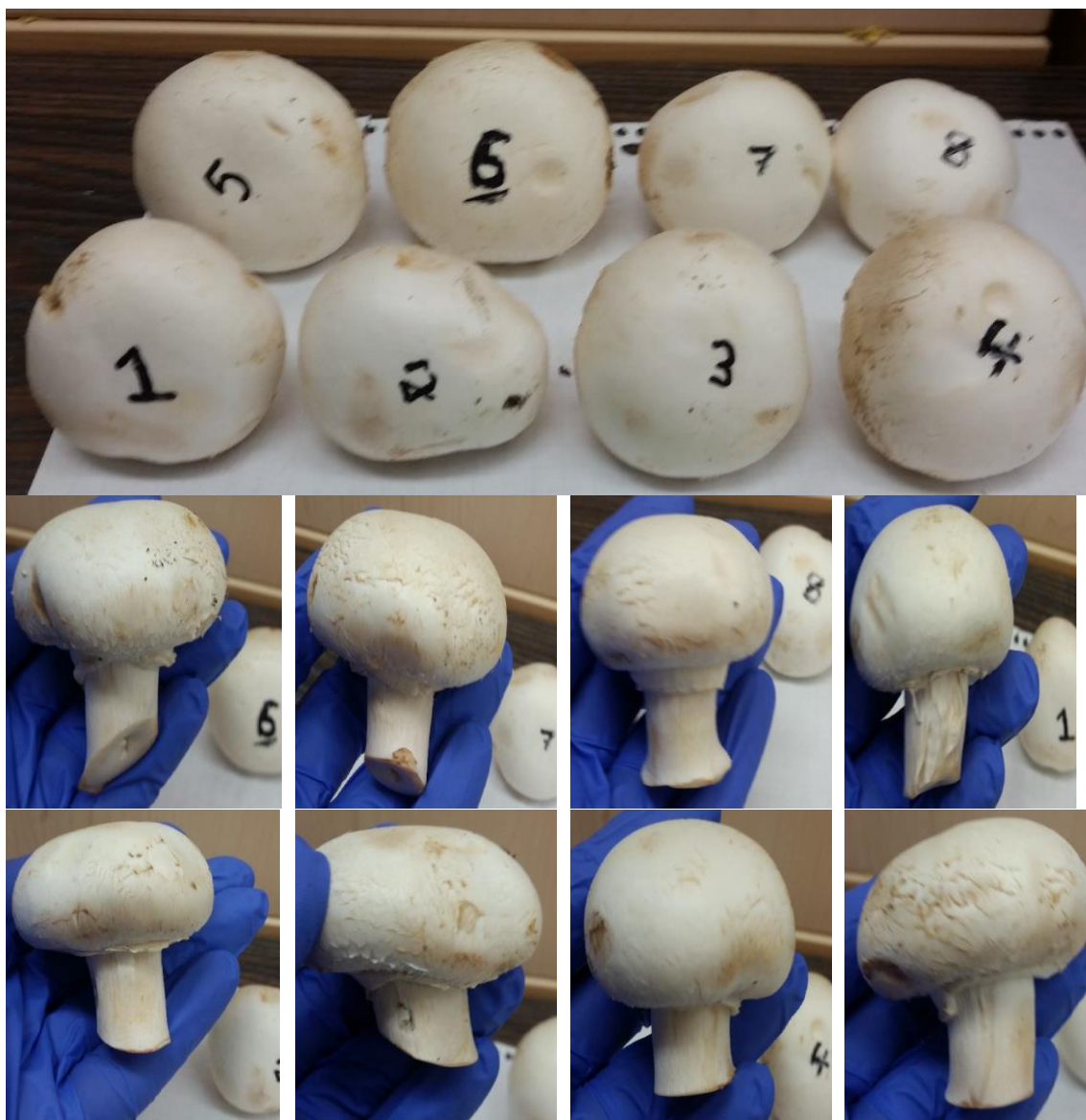
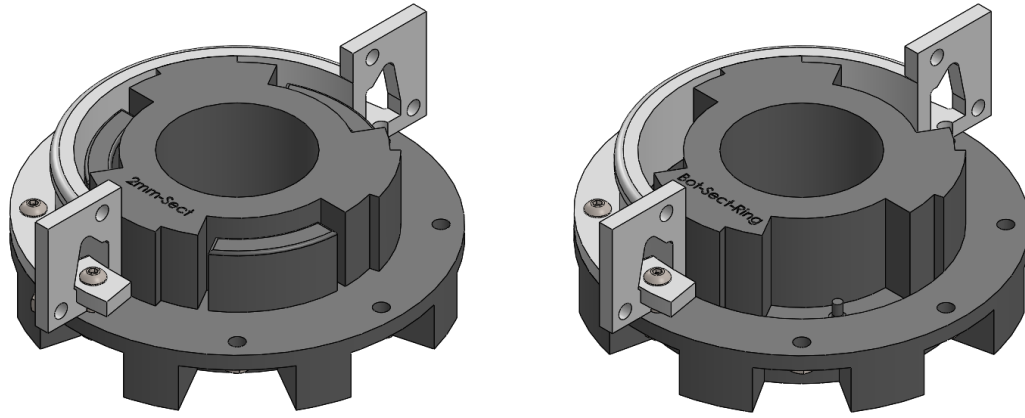


Figure C.6 Mushroom population for sample measurements (sample size $n = 8$).

Appendix D

Actuator Moulding System CAD & Drawings

The following pages are CAD drawings from SolidWorks Student Edition. The mould drawings shown are for fabricating actuators with wall thicknesses of 2 mm. Some design, assembly, and dimensions are not detailed within these drawings compared to traditional engineering CAD drawings. Instead, the drawings are intended for design insight and to give the reader an idea of how these mould sets were fabricated using a 3D printer. Several 3D printers were used in the fabrication of multiple mould sets, based on printer availability. The final mould sets used were fabricated with the Dremel 3D45 Printer. Each part was fabricated with an infill density of 18%, a layer height of 0.2 mm, and auto-generated support structures for overhanging parts of the printed model. Fragile parts of the mould, like the inlet ports in the bottom mould, have a 1 mm fillet at their base to help prevent shearing. Sharp corners that may come into contact with the actuator that are not critical to the soft geometry are also curved with fillets. Each SolidWorks model is saved as an STL file and uploaded to the Dremel DigiLab 3D Slicer software. The software converts the solid model into layered paths that the printer follows as it extrudes the filament. The prepared model is then uploaded to the printer as a G-code file by USB. Each mould assembly is bolted together with M4 socket button head cap screws and M4 hex nuts. Figure D.1 shows the CAD models for each mould set.



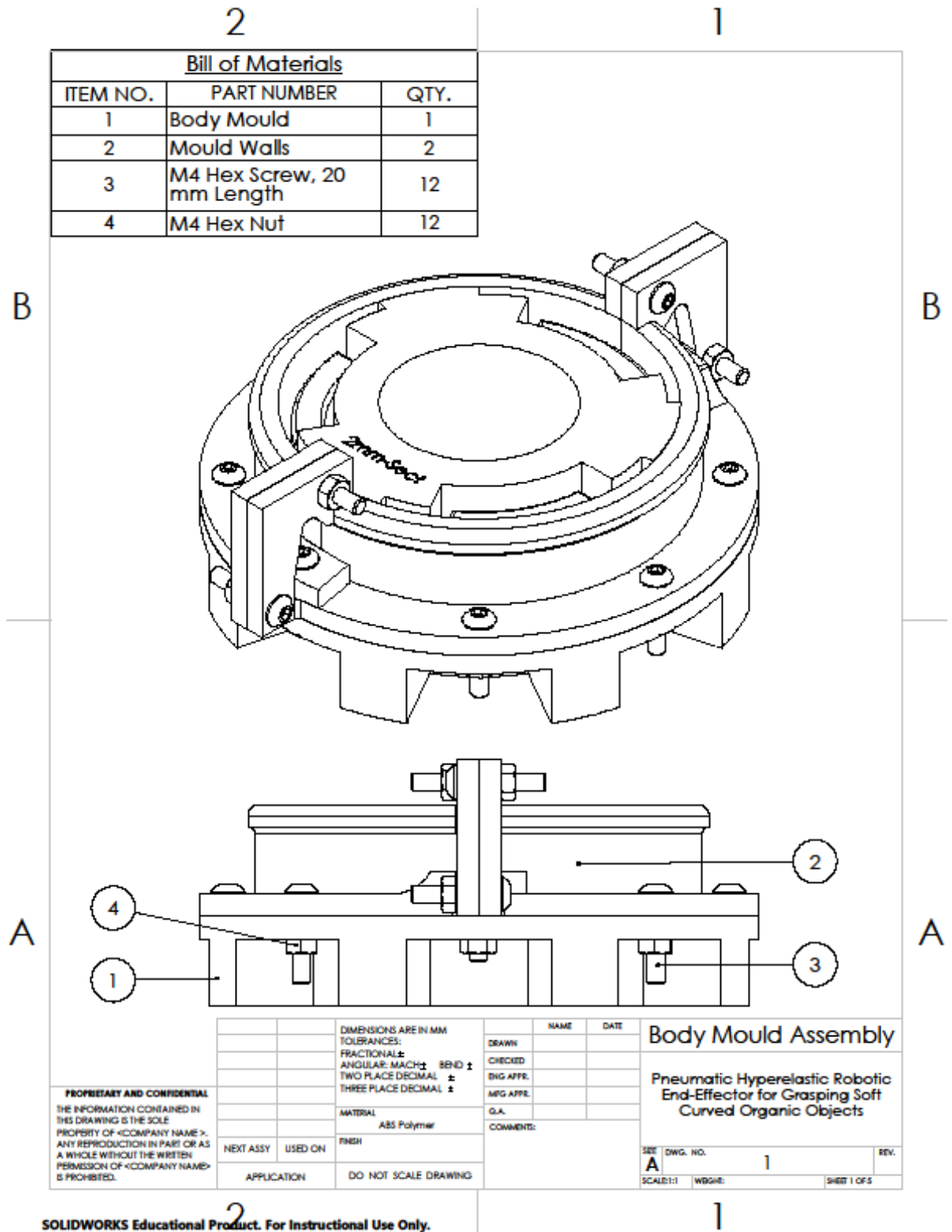
(a)

(b)

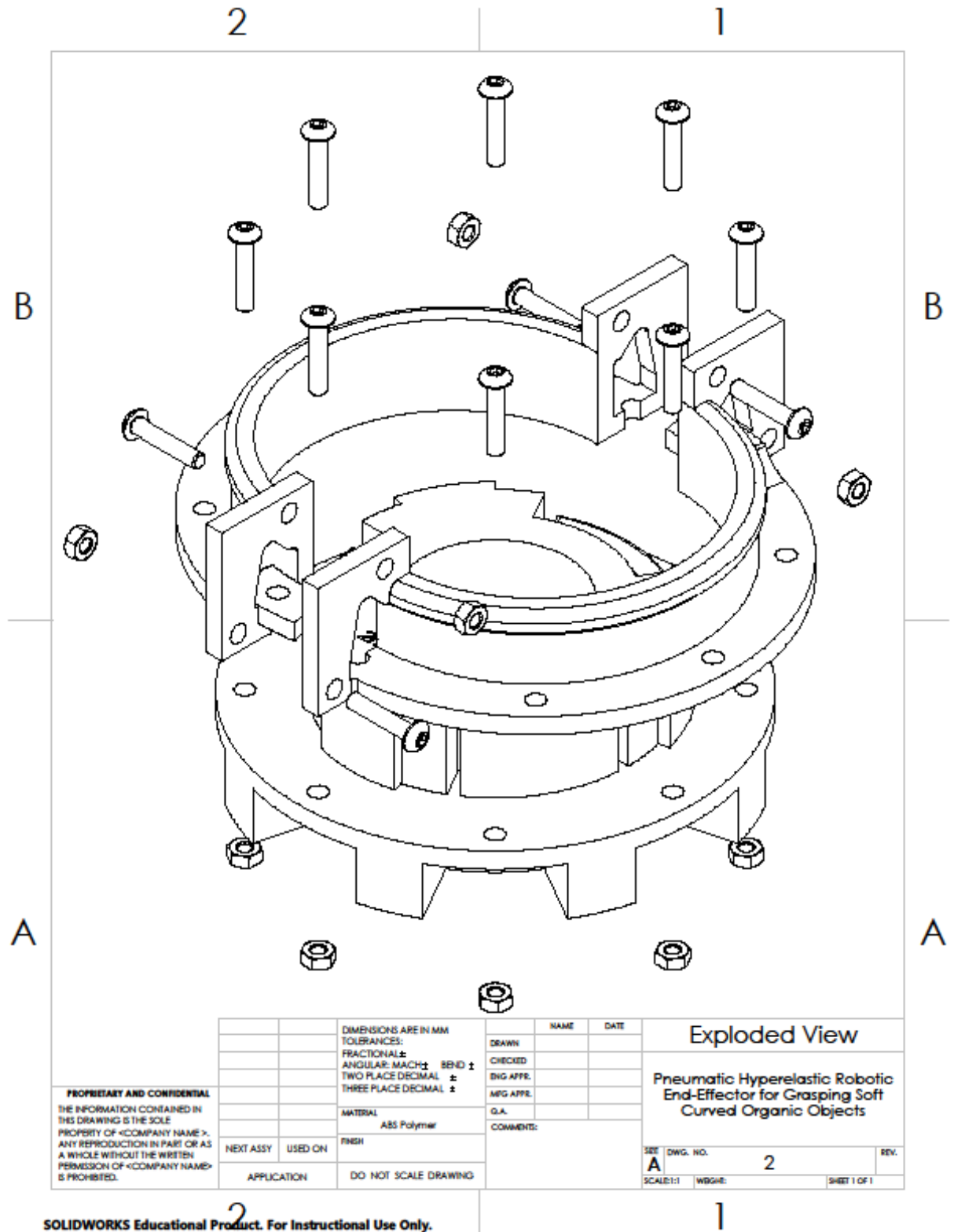
Figure D.1 CAD of actuator mould assemblies. (a) Mould set for actuator body; (b) Mould set for actuator bottom. Both models shown have the closest wall, nuts, and bolts hidden to provide a view of the mould interior.

The following pages of this research thesis present the CAD drawings for the mould sets. Units are in mm, and the drawings are at a 1:1 scale.

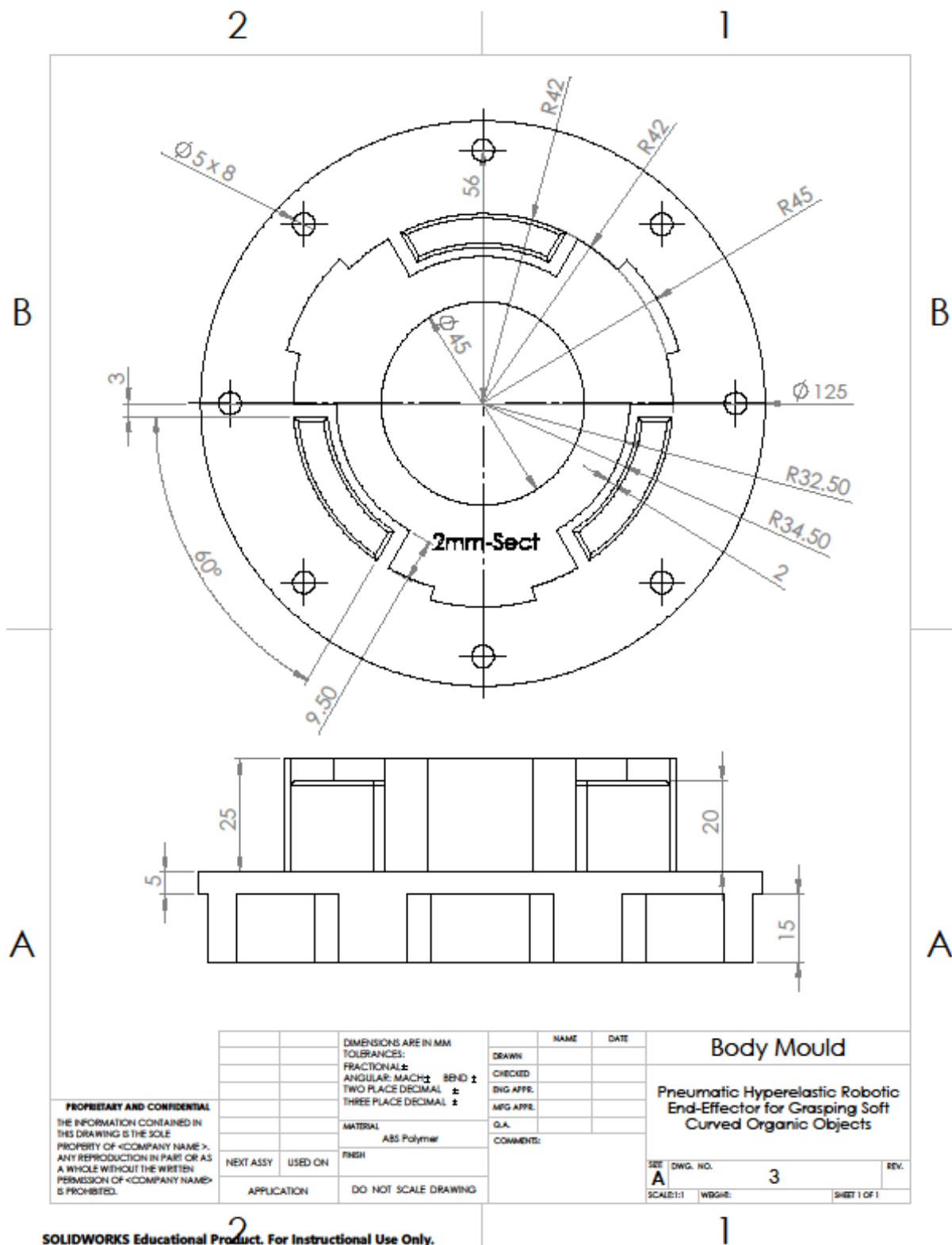
APPENDIX D. ACTUATOR MOULDING SYSTEM CAD & DRAWINGS



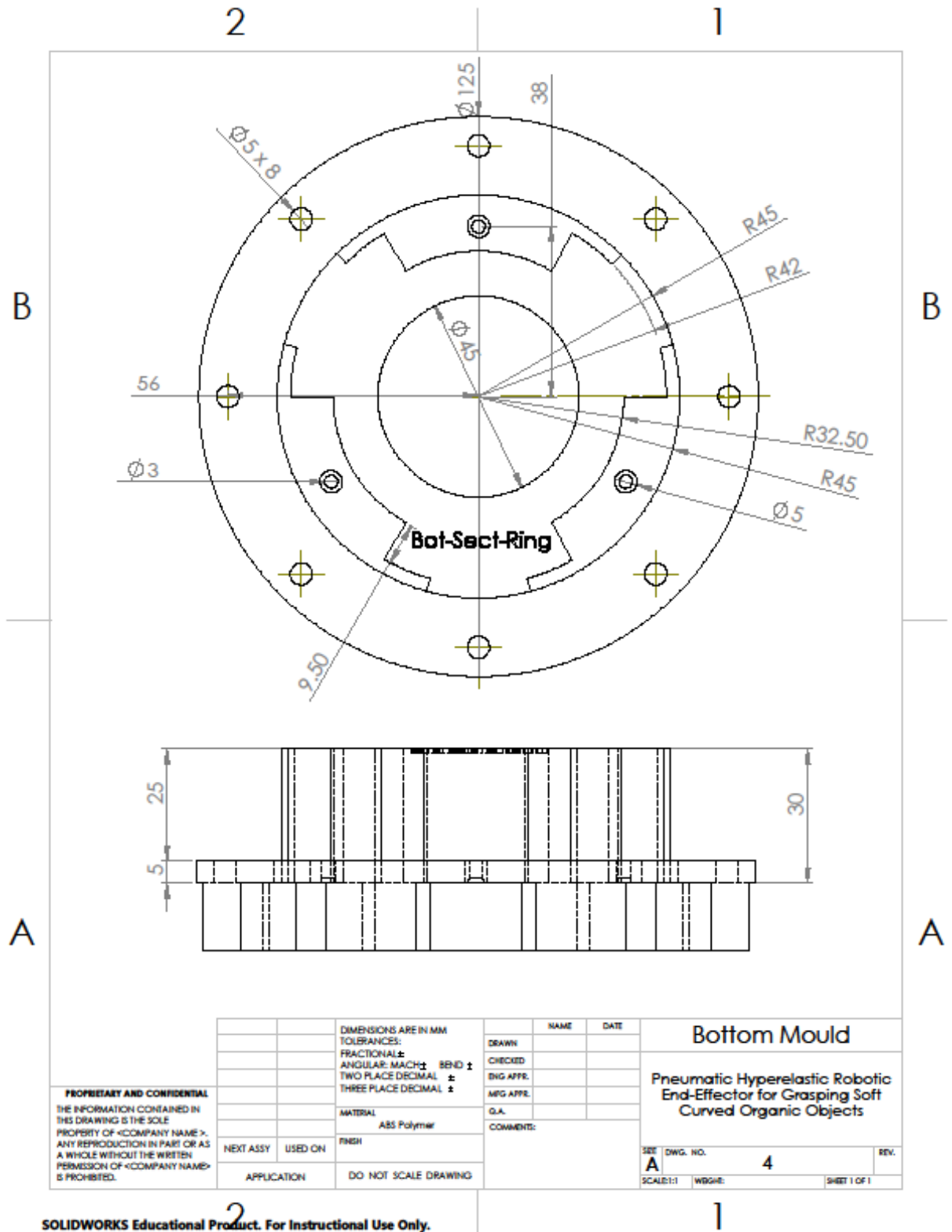
APPENDIX D. ACTUATOR MOULDING SYSTEM CAD & DRAWINGS



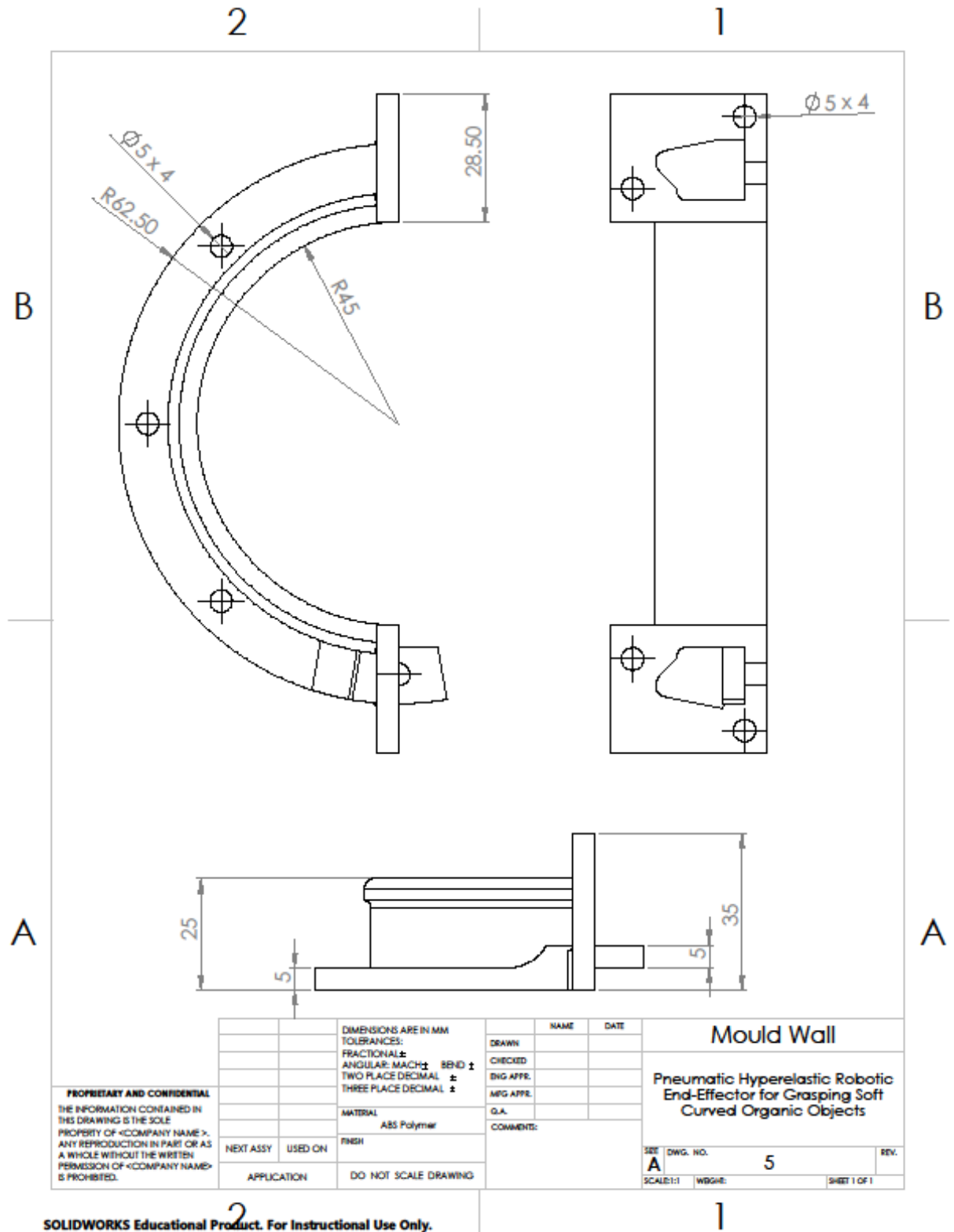
APPENDIX D. ACTUATOR MOULDING SYSTEM CAD & DRAWINGS



APPENDIX D. ACTUATOR MOULDING SYSTEM CAD & DRAWINGS



APPENDIX D. ACTUATOR MOULDING SYSTEM CAD & DRAWINGS



Appendix E

Copyright Permissions

The following pages provide confirmation of acquired copyright permissions for the appropriate referenced figures in this thesis. Included is a table summarizing the copyright information, followed by excerpts of the relevant emails. The table presents the figure permissions as they appear in the thesis. The excerpts are provided as figures. They are cropped to remove any personal information and only outline the copyright permission. Note that copyright permission from IEEE publications is provided based on the conditions outlined in the relevant statement below. Also note that copyright permission from MDPI publications is provided through the Creative Commons license (CC BY).

Table E.1 Summary of Copyright Permission Information. The column labelled “Reference Figure #” may include further annotations in parentheses. These correspond to their labelling within the thesis itself.

Thesis Figure #	Reference Title	Reference # in Thesis	Reference Figure #	1st Author	Publication	Publisher	License Confirmation #
2.5	Mechanically programmable bend radius for fiber-reinforced soft actuators	59	Figure 5	Kevin C. Galloway	2013 16th International Conference on Advanced Robotics (ICAR)	IEEE	IEEE Statement
2.6 (a), (b)	Mechanically programmable bend radius for fiber-reinforced soft actuators	59	(a) Figure 2 (b) Figure 3	Kevin C. Galloway	2013 16th (ICAR)	IEEE	IEEE Statement
2.7	Sleeved Bending Actuators for Soft Grippers: A Durable Solution for High Force-to-Weight Applications	29	Figure 2	Genevieve Miron	Actuators	MDPI	CC BY
2.9	The design and mathematical modelling of novel extensor bending pneumatic artificial muscles (EBPAMs) for soft exoskeletons	62	Figure 1	Hassanin Al-Fahaam	Robotics and Autonomous Systems	Elsevier B.V.	11824368, 11824388
2.10	Soft Robotics for Chemists	6	Figure 5	Filip Ilievski	Angewandte Chemie International Edition	Wiley	4611460433957
2.11	Soft Robotic Grippers for Biological Sampling on Deep Reefs	66	Figure 16 (A)	Kevin C. Galloway	Soft Robotics	Mary Ann Liebert Inc.	11824398
2.12	Universal soft pneumatic robotic gripper with variable effective length	54	Figure 4	Yufei Hao	2016 35th Chinese Control Conference (CCC)	IEEE	IEEE Statement
2.13	Mechanically programmable bend radius for fiber-reinforced soft actuators	59	Figure 11	Kevin C. Galloway	2013 16th (ICAR)	IEEE	IEEE Statement
2.14	Sleeved Bending Actuators for Soft Grippers: A Durable Solution for High Force-to-Weight Applications	29	Figure 3	Genevieve Miron	Actuators	MDPI	CC BY
C.1	Tyrosinase activity and isoform composition in separate tissues during development of Agaricus bisporus fruit bodies	74	Figure 4	J Van Leeuwen	Mycological Research	Elsevier LTD.	11824409
C.2	Carbohydrate Metabolism in Agaricus bisporus (Lange) Sing.: Changes in Soluble Carbohydrates during Growth of Mycelium and Sporophore	75	Figure I	J B W Hammond	Journal of General Microbiology	SOCIETY FOR GENERAL MICROBIOLOGY	11824411

APPENDIX E. COPYRIGHT PERMISSIONS

Publisher: IEEE
Date: Nov. 2013
Copyright © 2013, IEEE

Thesis / Dissertation Reuse

The IEEE does not require individuals working on a thesis to obtain a formal reuse license, however, you may print out this statement to be used as a permission grant:

Requirements to be followed when using any portion (e.g., figure, graph, table, or textual material) of an IEEE copyrighted paper in a thesis:

- 1) In the case of textual material (e.g., using short quotes or referring to the work within these papers) users must give full credit to the original source (author, paper, publication) followed by the IEEE copyright line © 2011 IEEE.
- 2) In the case of illustrations or tabular material, we require that the copyright line © [Year of original publication] IEEE appear prominently with each reprinted figure and/or table.
- 3) If a substantial portion of the original paper is to be used, and if you are not the senior author, also obtain the senior author's approval.

Requirements to be followed when using an entire IEEE copyrighted paper in a thesis:


- 1) The following IEEE copyright/ credit notice should be placed prominently in the references: © [year of original publication] IEEE. Reprinted, with permission, from [author names, paper title, IEEE publication title, and month/year of publication]
- 2) Only the accepted version of an IEEE copyrighted paper can be used when posting the paper or your thesis on-line.
- 3) In placing the thesis on the author's university website, please display the following message in a prominent place on the website: In reference to IEEE copyrighted material which is used with permission in this thesis, the IEEE does not endorse any of [university/educational entity's name goes here]'s products or services. Internal or personal use of this material is permitted. If interested in reprinting/republishing IEEE copyrighted material for advertising or promotional purposes or for creating new collective works for resale or redistribution, please go to http://www.ieee.org/publications_standards/publications/rights/rights_link.html to learn how to obtain a License from RightsLink.

If applicable, University Microfilms and/or ProQuest Library, or the Archives of Canada may supply single copies of the dissertation.

Figure E.1 Copyright permission statement by IEEE Publisher.

APPENDIX E. COPYRIGHT PERMISSIONS

7/4/2019 Copyright Clearance Center

 Copyright Clearance Center

Confirmation Number: 11824368

Citation Information

Order Detail ID: 71925000

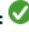
Robotics and autonomous systems by ELSEVIER BV. Reproduced with permission of ELSEVIER BV in the format Thesis/Dissertation via Copyright Clearance Center.

Order Details

Robotics and autonomous systems

Billing Status:
N/A

Order detail ID: 71925000
ISSN: 0921-8890
Publication Type: Journal
Volume:
Issue:
Start page:
Publisher: ELSEVIER BV

Permission Status:  **Granted**
Permission type: Republish or display content
Type of use: Thesis/Dissertation
Order License Id: 4611420709119

[View details](#)


Note: This item was invoiced separately through our **RightsLink service**. [More info](#)

\$ 0.00

Figure E.2 Copyright permission information for confirmation number 11824368.

APPENDIX E. COPYRIGHT PERMISSIONS

7/4/2019 Copyright Clearance Center



Confirmation Number: 11824388

Citation Information


Order Detail ID: 71925103

Robotics and autonomous systems by ELSEVIER BV. Reproduced with permission of ELSEVIER BV in the format Thesis/Dissertation via Copyright Clearance Center.

Order Details

Robotics and autonomous systems

Order detail ID: 71925103
ISSN: 0921-8890
Publication Type: Journal
Volume:
Issue:
Start page:
Publisher: ELSEVIER BV

Permission Status:  **Granted**
Permission type: Republish or display content
Type of use: Thesis/Dissertation
Order License Id: 4611450092365

[View details](#)

Billing Status:
N/A


Note: This item was invoiced separately through our **RightsLink service**. [More info](#)

\$ 0.00

Figure E.3 Copyright permission information for confirmation number 11824388.

APPENDIX E. COPYRIGHT PERMISSIONS

7/4/2019 Copyright Clearance Center

 Copyright Clearance Center

Confirmation Number: 11824398

Citation Information

Order Detail ID: 71925125


Soft robotics by Mary Ann Liebert, Inc., in the format Thesis/Dissertation via Copyright Clearance Center.

Order Details

Soft robotics

Billing Status:
N/A

Order detail ID: 71925125
ISSN: 2169-5172
Publication Type: Journal
Volume:
Issue:
Start page:
Author/Editor: Mary Ann Liebert, Inc.,

Permission Status:  **Granted**
Permission type: Republish or display content
Type of use: Thesis/Dissertation
Order License Id: 4611451188847

[View details](#)

Note: This item was invoiced separately through our **RightsLink service**. [More info](#) **\$ 0.00**

Figure E.4 Copyright permission information for confirmation number 11824398.

JOHN WILEY AND SONS LICENSE
TERMS AND CONDITIONS

Jul 04, 2019

This Agreement between Alexandre W Galley ("You") and John Wiley and Sons ("John Wiley and Sons") consists of your license details and the terms and conditions provided by John Wiley and Sons and Copyright Clearance Center.

License Number	4611460433957
License date	Jun 17, 2019
Licensed Content Publisher	John Wiley and Sons
Licensed Content Publication	Angewandte Chemie International Edition
Licensed Content Title	Soft Robotics for Chemists
Licensed Content Author	Filip Ilievski, Aaron D. Mazzeo, Robert F. Shepherd, et al
Licensed Content Date	Jan 20, 2011
Licensed Content Volume	50
Licensed Content Issue	8
Licensed Content Pages	6
Type of use	Dissertation/Thesis
Requestor type	University/Academic
Format	Print and electronic
Portion	Figure/table
Number of figures/tables	1
Original Wiley figure/table number(s)	Figure 5. The top row shows a 9 cm tip-to-tip PneuNet gripping an uncooked chicken egg. A string suspends the gripper and assists in lifting the egg; a tube, visible on the left side of the gripper, runs into the central portion of the gripper to provide pressurized air for actuation. On the bottom, a modified version of the starfish-based gripper with 14 cm tip-to-tip distance; thinner and longer fingers can pick up a live anesthetized mouse; here also, a string (dashed arrow) suspends the gripper, and a tube (solid arrow) from the side provides compressed air. A video of the gripper in action is available in the Supporting Information.
Will you be translating?	No
Title of your thesis / dissertation	Pneumatic Hyperelastic Robotic End-Effector for Grasping Soft Curved Organic Objects

Figure E.5 Copyright permission information for confirmation number 4611460433957.

APPENDIX E. COPYRIGHT PERMISSIONS

Confirmation Number: 11824409

Citation Information

Order Detail ID: 71925170

Mycological research by BRITISH MYCOLOGICAL SOCIETY ; FEDERATION OF EUROPEAN MICROBIOLOGICAL SOCIETIES Reproduced with permission of ELSEVIER LTD. in the format Thesis/Dissertation via Copyright Clearance Center.

Order Details

Mycological research

Billing Status:
N/A

Order detail ID: 71925170

ISSN: 0953-7562

Publication Type: Journal

Volume:

Issue:

Start page:

Publisher: ELSEVIER LTD.

Author/Editor: BRITISH MYCOLOGICAL SOCIETY ;
FEDERATION OF EUROPEAN
MICROBIOLOGICAL SOCIETIES

Permission Status: **Granted**

Permission type: Republish or display content

Type of use: Thesis/Dissertation

Order License Id: 4611470959980

[View details](#)

Note: This item was invoiced separately through our **RightsLink service**. [More info](#)

\$ 0.00

Figure E.6 Copyright permission information for confirmation number 11824409.

Confirmation Number: 11824411

Citation Information

Order Detail ID: 71925174

The Journal of General Microbiology by SOCIETY FOR GENERAL MICROBIOLOGY Reproduced with permission of **SOCIETY FOR GENERAL MICROBIOLOGY** in the format Republish in a thesis/dissertation via Copyright Clearance Center.

Order Details

The Journal of General Microbiology

Billing Status:
N/A

Order detail ID: 71925174

ISSN: 0022-1287

Publication Type: Journal

Volume:

Issue:

Start page:

Publisher: SOCIETY FOR GENERAL
MICROBIOLOGY

Author/Editor: SOCIETY FOR GENERAL
MICROBIOLOGY

Permission Status: **Granted**

Permission type: Republish or display content

Type of use: Republish in a thesis/dissertation

Order License Id: 4611471263850

[View details](#)

Note: This item was invoiced separately through our **RightsLink service**. [More info](#)

\$ 0.00

Figure E.7 Copyright permission information for confirmation number 11824411.

Curriculum Vitae

Name: Alexandre Galley

Post-secondary Education and Degrees: The University of Western Ontario
London, Ontario, Canada
2012-2017 B.E.Sc

The University of Western Ontario
London, Ontario, Canada
2017-2019 M.E.Sc

Honours and Awards: MME Graduate Teaching Assistant (GTA) Award
2017 (Fall Term) – 2019 (Year)

Related Work Experience Teaching Assistant
The University of Western Ontario
2017-2019

MITACS Accelerate Internship
Vineland Research and Innovation Centre, Lincoln, ON
2017-2018

Publications: